Expedition 314 Site C0002[1]

Expedition 314 Scientists[2]

Chapter contents

Background and objectives

At Integrated Ocean Drilling Program Site C0002 (proposed Site NT3-01B), we planned and carried out logging-while-drilling/measurement-while-drilling (LWD-MWD) operations to 1400 meters below seafloor (mbsf) through the Kumano forearc basin section and the underlying formations, interpreted as older rocks of the accretionary prism and/or early slope basin sediments deposited prior to the development of the megasplay fault and forearc basin (Fig. F1). Scientific objectives included investigation of the outer forearc basin depositional systems, especially documentation of the turbidite depositional record, the physical properties of these basinal sediments and the underlying preexisting rocks, likely gas hydrate deposits, and a bottom-simulating reflector (BSR) within the forearc basin sediments. We were able to drill and log the entire section from 0 to 1401 mbsf with complete success. An excellent suite of logs and vertical seismic profile (VSP) data reveal the structure, physical properties, and stress state of the forearc basin, the gas hydrate–bearing zone, and the underlying deformed rocks of the inner accretionary prism. The LWD program at this site is the deepest LWD penetration in Ocean Drilling Program (ODP)/Integrated Ocean Drilling Program history to date, as well as the deepest penetration of any type into the interior of an accretionary prism.

Site C0002 is slated for deep drilling across the entire plate boundary system to >5500 mbsf during later stage riser drilling (Tobin and Kinoshita, 2006), and the location was selected primarily to meet deep riser drilling objectives to the plate boundary and megasplay reflectors rather than based on the shallower targets drilled during Expedition 314. However, these shallower targets are important primary objectives of the Nankai Trough Seismogenic Zone Experiment (NanTroSEIZE) Stage 1 in their own right. Operations during Expedition 314, along with later coring, had the following goals:

- Document the depositional and uplift history of outer Kumano Basin sediments to shed light on the long-term slip history of the megasplay fault system and deformation in the accretionary prism,
- Sample the interior of the accretionary prism below the forearc basin,
- Determine the orientation and magnitude of horizontal stresses in the forearc basin and the prism below, and

[1] Expedition 314 Scientists, 2009. Expedition 314 Site C0002. *In* Kinoshita, M., Tobin, H., Ashi, J., Kimura, G., Lallemant, S., Screaton, E.J., Curewitz, D., Masago, H., Moe, K.T., and the Expedition 314/315/316 Scientists, *Proc. IODP,* 314/315/316: Washington, DC (Integrated Ocean Drilling Program Management International, Inc.). doi:10.2204/iodp.proc.314315316.114.2009
[2] **Expedition 314/315/316 Scientists' addresses.**

doi:10.2204/iodp.proc.314315316.114.2009

- Provide critical physical property information needed to plan for later stage riser drilling and casing program, as well as for observatory installation.

As planned, drilling was successful to total depth (TD) of 1401 mbsf and included continuous logging of the entire sedimentary section through the Kumano Basin and several hundred meters of the underlying rocks. A principal objective was to penetrate through this seismically imaged unconformity to sample the underlying formation. Characterization of seismic velocity, density, porosity, stress, rock strength parameters, and pore pressure in both tectonic domains (basin and prism) were all high priorities.

Based on the seismic reflection data, the uppermost ~950 m in the Kumano Basin domain was expected to be primarily turbiditic and hemipelagic sediments deposited in the forearc basin, with progressive tilt caused by development and displacement of the megasplay system. Several discrete packages of basin sediment bounded by unconformities are evident in this section. Within this sequence, a prominent BSR interpreted as the base gas hydrate reflection is evident at ~400 mbsf (Fig. **F2**). Log data were used to estimate the presence and distribution of gas hydrate and possible free gas in the sediment porosity at Site C0002 (see **"Log characterization and lithologic interpretation"** and **"Physical properties"**).

Between the base of the Kumano Basin at ~936 mbsf and the shallowest branch of the megasplay fault system at ~4000 mbsf lies an interval of rock interpreted as frontally accreted material of the accretionary prism. By analogy with land-based geology and ODP Leg 190 Site 1178, where the interior of the Nankai accretionary prism was drilled in the Muroto region (Ujiie et al., 2003), we anticipated a sequence of variably dipping and disrupted clastic strata cut by numerous small faults, locally forming mélange. Drilling and sampling of this domain affords the first-ever penetration of the deep, older interior of an active accretionary prism, addressing long-standing questions on the fate of offscraped material, the evolution of accretionary mélanges, and role of fluids in prism interiors. Logging to detect fracture and bedding orientations and variability, porosity and density, and state of stress in this environment was therefore a major objective as well.

Operations

Transit to Site C0002

The D/V *Chikyu* moved to a low-current area (14 nmi northwest of Hole C0001D) on 13 October 2007 in order to avoid shock and vibration from the Kuroshio Current while picking up and running in with the LWD bottom-hole assembly (BHA) and drill collars. The ship drifted to the location of Site C0002 at 1.5 kt while running the LWD BHA, and the ship arrived at the location at 2145 h.

Hole C0002A

Preparation for drilling began at 0400 h on 13 October 2007. Like the previous LWD-MWD-annular-pressure-while-drilling (APWD) holes, the LWD tools (6¾ inch [17.15 cm] collars) included the geoVISION tool with a 23.18 cm button sleeve, the sonicVISION tool (four-receiver array), the MWD (PowerPulse) tool, the seismicVISION tool, and the adnVISION tool. A breakdown of operations is given in Table **T1,** and the full BHA is described in Table **T2.**

Tools were assembled, and communication and function checks were conducted at 36.8 m drillers depth below rig floor (DRF) between 0730 and 0800 h. The radioactive source for density measurement was installed and the BHA was lowered to 700 m DRF. From 1430 to 2200 h, the *Chikyu* slowly drifted to the hole position while the bit was lowered to 1488 m DRF, where a second series of tests was successfully conducted. After tagging the seafloor at 1964.5 m DRF (1936 m mud depth below sea level [MSL]) the hole position was located and surveyed by remotely operated vehicle (ROV) from 2200 h on 13 October to 0045 h on 14 October.

Hole C0002A was jetted-in from 1964.5 to 2035 m DRF (0–70.5 m LWD depth below seafloor [LSF]) at 0045 h on 14 October with an initial pump rate of 714 gpm (2700 L/m). Drilling continued with an average rate of penetration (ROP) of ~30 m/h, normal collar rotation (80–100 rpm), and minimal weight on bit (WOB). Surface pump pressure maintained at 15 MPa while pump flow rate was decreased to ~2500 L/m. At 0445 h, a problem with the inline blowout preventer prevented real-time communication with the LWD tools. After repairs (0515 h), drilling continued to 709.5 m LSF (2674 m DRF) and the decision was made to relog the missing section (535.5–556.5 m LSF) during the next wiper trip. A wiper trip was conducted from 709.5 to 401.5 m LSF (2674 to 2366 m DRF) between 1500 and 1745 h on 15 October, and missing data were successfully collected. Drilling continued to TD of 1401.5 m LSF (3366 m DRF) at 0600 h on 17 October without any difficulties except moderate increase in equivalent circulating density (ECD) at each pipe connection, which was rapidly controlled with mud recirculation.

The hole was displaced with 100 m^3 of kill mud (density 1.3 g/cm^3). At 1400 h on 17 October, two stands of pipe were removed to create an offset in uphole check shots at every pipe disconnection. All LWD tools were recovered on the rig floor at 0800 h on 18 October, and all memory data were successfully downloaded. However, the seismicVISION battery failure before retrieval of the tool required that data be sent to the land base for processing. A time version of the surface drilling parameters and downhole ECD, annular pressure measurement (APRS), and real-time gamma ray log (GR_RAB_RT) is given in Figure **F3.**

Transit to Site C0003

As the BHA was rigged down from Hole C0002A, the ROV was deployed to pick up four beacons at 0800 h on 18 October 2007. The ship was then moved to the next site (proposed Site NT2-01D) at 1700 h for 6 nmi with average speed of 6 kt, and four beacons were deployed at 2130 h. At this site, the deployment plan was changed for greater efficiency and safety. The ship was moved against the Kuroshio Current by 12 nmi from 1400 h on 19 October for 3.5 h with average speed of 3.4 kt. The BHA was then made up and run into the sea as the ship drifted back at 1.5 kt from 2130 h. Upon arriving at the location at 0530 h on 20 October, running continued to 2480 m DRF. The bit was positioned, and a survey was made of the sea bottom.

Data and log quality

Hole C0002A

Available data

Hole C0002A was drilled with LWD-MWD-APWD tools. MWD-APWD data were transmitted in real time with a limited set of LWD data (see Table **T2** in the "Expedition 314 methods" chapter). When LWD tools were recovered on the rig floor, memory data were successfully downloaded and processed according to the data flow described in **"Onboard data flow and quality check"** and Figure **F8** in the "Expedition 314 methods" chapter. A list of available LWD data is given in Table **T3** in the "Expedition 314 methods" chapter.

Depth shift

The mudline (seafloor) was identified from the first break in the gamma ray (GR) and resistivity logs (Fig. **F4**). In Hole C0002A, the mudline was picked at 1964.5 m DRF, showing no discrepancy with drillers depth (water depth = 1964.5 m DRF; 1936 meters below sea level [mbsl]). The depth-shifted versions of the main drilling data and geophysical logs are given in Figures **F5** and **F6,** respectively. Figure **F7** presents the time-depth relationship linking the time (Fig. **F3**) and depth version (Figs. **F5, F6**) of the data from Hole C0002A.

Logging data quality

Figure **F5** shows the drilling control logs. The target ROP of 30 m/h (±5 m/h) was generally achieved until TD (1401.5 m LSF). This ROP was sufficient to record one sample per 4 cm over the majority of the hole. WOB was set to a minimal value (<5 kkgf for most of the drilled interval). Surface pump pressure (SPPA) was maintained at constant value (~15–18 MPa) for the entire drilling period, and a normal (hydrostatic) increasing trend in APRS and ECD was observed. The four azimuthal calipers (C15, C26, C37, and C48) showed poor borehole condition with washouts exceeding 2 inches (5.08 cm) in most places except between 830 and 930 m LSF, where the hole was almost in gauge (stand-off < 1 inch [2.54 cm]). Stick-slip and friction increased linearly with the length of the penetrated interval but never exceeded the critical limit of 250 rpm that could impair geoVISION resistivity tool (GVR) image quality. In the washed out lower section of the hole (950–1400 m LSF), the GVR experienced numerous shocks with peak intensity sometimes >25 g without any failure.

Time after bit (TAB) measurements were ~5–10 min for the gamma ray log, except in a short depth interval corresponding to pipe connections where they sometimes exceeded 1 h. The gamma ray log is highly correlated to borehole shape, suggesting lithology-controlled washouts of sandy layers. TAB measurements for density and neutron porosity logs are ~45 min. In spite of the major washouts, the image-derived density (four bin average maximum azimuthal density [IDRO]) and image stand-off correction (IDDR) provide valuable logs. TAB measurements for resistivity were between 5 and 10 min. Where hole conditions were good, comparison between deep button (RES_BD) and shallow button (RES_BS) resistivity values showed that drilling fluid invasion was not significant, consistent with the short TAB readings. Elsewhere, the discrepancy between deep and shallow readings reflects possible invasion in permeable (sandy) layers or poor hole conditions (washouts, also associated with sandy layers).

The sonicVISION data for Hole C0002A were processed by the Schlumberger Data Consulting Services (DCS) specialist on board the *Chikyu*. Three products were produced. The first analysis relies on a broad band-pass filter on the data acquired during drilling, referred to here as "wide." The second relies on a very narrow band-pass filter, designed to pass only

the leaky *P*-wave arrival on the data acquired during drilling, referred to as "leaky-P." The third relies on the wide filtering on the data acquired at high speed while pulling out of the hole, referred to as "wide-fast." As a result, the composite sonic velocity curve for this site includes data from all three processed logs (Table T3). In the upper half of the hole (0–634 m LSF), the results of all three processed logs were used. The leaky-P data were only used for intervals where neither of the other logs allowed reliable picks. The wide data were the most reliable in the bottom half of the hole, so these data were used to assemble the composite log from 634 to 1293 m LSF.

The quality control analysis of the sonic data is based on examination of the plots showing the sonic waveforms and the slowness coherence images for the common receiver data and the common source data (Fig. F8). The full versions of these three plots are available as picture description standard (Schlumberger) format files in the raw data for the expedition (available at sio7.jamstec.go.jp). Figure F8 illustrates a typical example of an interval in which few if any picks are possible (Quality Type 3 in Table T3). Examples of Types 0–2, are shown in "Data and log quality" in the "Expedition 314 Site C0001" chapter.

Density, gamma ray, and resistivity images are of very good quality. However, depth shifts of several tens of centimeters are observed in these images. These depth shifts are neither systematic nor constant with depth. They even occur within the images from the same tool (e.g., geoVISION deep, medium, and shallow resistivity images). All images and scalar logs were processed with the same time-depth conversion files; however, the origin of these local depth shifts is not clear and can not be realistically attributed to preprocessing of the data. At first, these depth shifts seemed localized in zones of high contrast (resistivity, density, and gamma ray values) suggesting a possible combination of (1) tool deviation in respect to layering and (2) shoulder effect. Selected examples were sent to a Schlumberger DCS specialist on shore for further investigation. He reported similar observations on past drillship expeditions, suggesting that incomplete heave compensation and rapid vertical movements between the sampling of all data (sampling rate = 5 s) are the origins of the depth shifts. Most of the analyses conducted on board were done on the shallow resistivity image. Density (density correction and photoelectric factor [PEF]) and gamma ray images have not been used for log characterization, physical properties, structural analyses, or log-seismic integration.

The resistivity image log from Hole C0002A extends from 129 to 1398 m LSF (Table T4). Overall, the quality of the image data is excellent (except isolated spurious depth shifts discussed above). The log is marked by three 1 m intervals of poor quality where the image is smeared, perhaps because of lack of rotation. A short section of variable resistivity around the hole circumference occurs from 129 to 197 m LSF, probably because of hole eccentricity. Sharp changes in resistivity along knife-edge planar horizontal surfaces, typically bounding decimeter or thicker domains, are suspected to be drilling artifacts. Centimeter-scale horizontal variations in resistivity are also suspected to be artifacts because of their thinness, regularity, and horizontal orientation. Overall, the general structural patterns and sedimentary features are apparent. Interpretation of resistivity image data is further discussed in "Structural geology and geomechanics" in the "Expedition 314 Site C0001" chapter.

Log characterization and lithologic interpretation

Log characterization and identification of logging units

Hole C0002A logging units were characterized from visual inspection of the gamma ray, resistivity, bulk density, and PEF log responses (Fig. F1). The resistivity images were used to define finer scale characteristics within the units. Four primary logging units were defined, as well as two zones of variation within logging Unit II (Table T5). Bulk density and *P*-wave velocity values increase slightly with depth, whereas neutron porosity decreases with depth, showing a clear compaction trend.

Logging Unit I (0–135.5 m LSF) exhibits a particularly homogeneous conductive character in the resistivity images. The ultrasonic caliper log indicates poor borehole quality between 43.3 and 135.5 m LSF. Gamma ray, resistivity, and density log values are relatively low throughout this uppermost section and change abruptly to higher values at 135.5 m LSF (Fig. F1). This shift is taken as the boundary between logging Units I and II.

At the upper boundary of logging Unit II (135.5–830.4 m LSF), the variability of the resistivity and gamma ray logs increases from the baseline values. Caliper values are good throughout most of logging Unit II, with the exception of 481.6–547.1 m LSF and the lowermost section (below ~700 m LSF). Bulk density values show intervals of larger and smaller variability; stronger negative spikes correlate well to higher caliper values, indicating washouts (Fig. F1). Two zones were identified within logging Unit II. Zone A (218.1–400.4 m LSF) is similar to the rest of

logging Unit II in terms of gamma ray, PEF, and neutron porosity log responses. However, resistivity logs show >50 significant resistive spikes (2–50 Ωm). Zone B (481.6–547.1 m LSF) was defined as the highest sustained frequency and magnitude of log variations seen in logging Unit II. More than 50 conductive and low gamma ray layers occur within this zone.

Logging Unit III (830.4–935.6 m LSF) is characterized by relatively consistent responses in the gamma ray (75 gAPI), resistivity (1.4 Ωm), bulk density (2.0 g/cm^3), sonic velocity (2500 m/s), and neutron porosity (0.5 PU) logs. The PEF values increase gradually over the upper few tens of meters and remain at a relatively elevated baseline (3.3 b/e$^-$) until decreasing at the base of the unit (Fig. **F1**).

In logging Unit IV (935.6–1400 m LSF) all of the log responses exhibit high variability. Caliper values are high throughout, and the density and sonic logs are correspondingly unreliable for significant portions. The neutron porosity and PEF curves reach their highest variability and lowest values within this unit. The gamma ray and resistivity logs have generally higher variability magnitudes than in any of the other logging units but do not exhibit as high or as many resistive peaks as in Zone A of logging Unit II (218.1–400.4 m LSF). Within logging Unit IV are several more homogeneous intervals that exhibit moderately high gamma ray, PEF, and resistivity log values.

Basic statistical analysis supports the broad logging units defined above. The fluctuation in the PEF curve and constraint of other parameters in logging Unit III indicate a difference in composition from the other units (Fig. **F9**). The variation in sonic log trend illustrates the unique characters of Zones A and B.

Log-based lithologic interpretation

Low resistivity associated with low gamma ray values and a higher average borehole diameter are common throughout the borehole. The difference between the shallow and deep resistivity log values for a given depth can be taken as an approximation of the degree of invasion of drilling fluid into the formation (Fig. **F10**). Intervals with significantly high resistivity difference (i.e., deep button resistivity is greater than shallow button resistivity) coincide with the gamma ray lows that are typically associated with sandier lithologies. Where borehole quality is good, high resistivity differences may indicate permeable layers which have been partially invaded. Therefore, lower (darker color) resistivity images alongside particular log responses throughout the borehole are indicative of higher sand content, with high conductivity potentially an effect of invasion.

A subtle change in bedding dip is exhibited at each of the logging unit boundaries, implying that they are angular unconformities (Fig. **F11**). Logging Unit IV is composed of steeply dipping beds with variable orientations. Bedding in logging Unit III exhibits a clear bimodal distribution between north and south dip directions. Logging Unit II consistently dips shallowly to the northwest except for the very top of the section, which begins to dip to the south. The bedding that can be seen in logging Unit I dips shallowly to the south.

Logging Unit I

Logging Unit I exhibits conductive resistivity images corresponding to sandy beds with significant washouts. Layering is also faintly visible. Accordingly, the lithology for logging Unit I is thought to be unconsolidated sandy/silty mud. Low density and high caliper measurements, as well as sonic velocity measurements coinciding with the borehole fluid arrival, indicate that Unit I is the least consolidated of the units defined in this hole.

Logging Unit II

Below the logging Unit I/II boundary, resistivity images show more variation, with clearer bedding. Fine bedding in the images corresponds to high variation in the other logs. The high variability throughout the unit is attributed to the lithologic and compositional variation within turbidite sequences, which are characterized by higher amplitudes and frequencies of variation in the gamma ray, resistivity, and density values (Fig. **F12A**). When viewed at a finer scale, many of the gamma ray cycles show an abrupt drop from values indicative of mud below to those indicative of higher sand content above, followed by a gradual, fining-upward trend returning to muddier values. The sand beds identified in the gamma ray log also exhibit low *P*-wave velocity and resistivity and a slightly larger borehole diameter, implying that the beds are uncemented, soft, and permeable. Meter-scale cycles dominate and are locally expressed in the density profiles. Several zones of smaller scale cycles are interpreted as finely interbedded sand and mud (Fig. **F12A**). Some decameter-scale cycles are also observed, as well as slightly sandier intervals in the lower half of the unit (Fig. **F12B**). Overall, logging Unit II appears to consist of sandy/silty turbidites and hemipelagic mud, with some variation in frequency of interbeds and composition.

Two zones within logging Unit II demonstrate differences potentially related to postdepositional properties and thus are classified differently. Zone A resis-

tivity logs show >50 significant resistive spikes (2–50 Ωm), ranging from 20 to 140 cm in thickness and fewer conductive spikes than the rest of logging Unit II (Fig. F12A). More than half of these resistive peaks occur between 350 and 400 m LSF and are generally >75 cm thick (Fig. F13A). Low gamma ray values, high velocity, and better borehole diameter are associated with these occurrences.

Both resistivity and sonic baseline values increase slightly throughout Zone A and decrease sharply at the base. Interpretation of the seismic data indicates a negative polarity BSR near 400 m seismic depth below seafloor (SSF). The interval above the BSR probably contains gas hydrates, which yield high resistivity and velocity values but have low density and little effect on the gamma ray log. Upon closer examination (Fig. F13A), resistivity peaks are usually found at the base of asymmetric gamma ray log lows, which have been interpreted as fining-upward sequences with gradational tops. This relation indicates a host bed grain-size control on porosity and gas hydrate formation.

More than 50 possible sand layers occur within Zone B, with thicknesses ranging from 20 cm to 1 m (Fig. F13B). The sand beds are thickest between 500 and 525 m LSF, whereas the thinnest beds are observed near the top and bottom of the zone. Above and below Zone B are mud-rich zones, which yield less variation in resistivity log responses and a lower magnitude of separation between the deep and shallow resistivity values. This implies that the strata in Zone B, particularly the central portion (500–525 m LSF), are more permeable and form a possible conduit for gas and liquid. Increased magnitude of variation in the density log through this zone, slightly depressed sonic log values, and the presence of a negative polarity bedding reflection in the seismic profiles (Fig. F14) suggest the presence of abundant gas.

Logging Unit III

Logging Unit III displays distinctly different log responses from the logging units above and below (Fig. F15). Low variation from gamma ray and resistivity baselines, which are near the high end of logging Unit II values, indicates a uniform lithology within logging Unit III, similar in some respects to the mud-rich end-member of the Unit II variation. Values of PEF near 3.5 b/e$^-$ are particularly high, in contrast to 3 b/e$^-$ in the section above. This difference suggests a compositional change to a very low sand content, as 3.5 b/e$^-$ is close to pure shale or mudstone values (Rider, 1996). Resistivity images show very fine layering and a decrease in breakout occurrences. The most likely lithology is hemipelagic mud.

Several conductive peaks in the resistivity logs, corresponding to low gamma ray, PEF, and density log values, are found in the middle portion of logging Unit III and are interpreted as thin sand or silt beds. These beds are at depths (~890 m LSF) consistent with an unconformity seen in the seismic profile (top of lower sediments I in Fig. F14). Distribution of dips within this unit shows that above this unconformity the dips are dominantly southward, whereas below the dips are dominantly to the north (Fig. F11). This differs somewhat from the seismic interpretation, which shows the upper part of logging Unit III (seismic Unit Kumano 11) dipping to the north. However, the surface of this unconformity may be uneven, and the southward dip may be a local phenomenon. Above the unconformity, the PEF curve decreases upward to the top of the unit; however, other logging parameters show no difference from the lower portion of the logging unit. Classification of a lithologic boundary at this unconformity is therefore not warranted.

Logging Unit IV

Logging Unit IV corresponds to the accretionary prism inferred in the seismic interpretation (Fig. F14). The boundary between logging Units III and IV is sharp and marked by a negative spike in each log except for the neutron porosity. All of the logs except for resistivity and PEF return to values similar to logging Unit II and III baselines within 40 m of the logging Unit III/IV boundary. Observed bedding dips are steeper and more variable in logging Unit IV than in the logging units above. Intervals which exhibit more variation, particularly in the resistivity, and intervals which appear more homogeneous are both observed within Unit IV. Some of the intervals of high variability are similar to Unit II, with some fining-upward cycles and meter to decameter scales of variation. High caliper values (9.5–14 inches) are believed to indicate higher concentration of uncemented sand both within these cycles and overall. These zones are interpreted as strongly deformed sandy/silty turbidite sequences.

The more homogeneous intervals of logging Unit IV are distinctive on the image logs, where they appear mottled (Fig. F16). These more homogeneous intervals are characterized by relatively constant, high gamma ray and density values and significantly less variability in resistivity logs. Associated high resistivity could be attributed to compaction, which would make the formation more stable and is consistent with good borehole quality. The homogeneous appearance indicates higher clay-size content, although the mottled appearance on the resistivity images lends itself to several interpretations. Given the

deformed nature of the rest of Unit IV, it is possible that the mottled sections are the dismembered remnants of clay-rich horizons. Incorporation of volcanic ash or volcaniclastic inputs are also possible with this interpretation. An alternative hypothesis is that logging Unit IV may be composed predominantly of deformed interbeds of sand and mudstone with local mass flow deposits. The mottled sections would correspond to more homogeneous intervals.

Physical properties

Physical properties analyzed at Site C0002 include thermal neutron porosity (TNPH), IDRO, five different resistivity logs (bit; ring; and shallow, medium, and deep button), and sonic *P*-wave velocity. Porosities were also derived by several different methods. A series of cross-plots between different physical properties were produced to compare and reveal relationships between properties.

Density

The density log in Hole C0002A is based on IDRO, which is derived by extracting the highest value from the 16 azimuthal measurements of density at a given depth.

Log density in Hole C0002A generally increases with depth (Fig. **F17**). In logging Unit I, the density log increases rapidly from 1.15 g/cm³ at the seafloor to 1.68 g/cm³ at 64.0 m LSF. From 64.0 m LSF to the bottom of Unit I (135.5 m LSF) density data are affected by hole conditions. The density log remains nearly constant at ~1.8 g/cm³ from ~136 to ~300 m LSF with some negative spikes. The density log shifts to higher values (~1.9 g/cm³) between 299.3 and 343.8 m LSF with minor fluctuations and then remains constant (~1.93 g/cm³) to 481.6 m LSF. No large fluctuations in density are observed in Zone A (hydrate zone) (see **"Log characterization and lithologic interpretation"**), whereas resistivity data show high variability (see **"Resistivity and estimated porosity"**). The density log shows a gradual increase to ~2.0 g/cm³ at the base of logging Unit II. In Zone B (potential gas zone, 481.6–547.1 m LSF) density exhibits large variations associated with fluctuations in the caliper, which can also be seen on the resistivity log (see **"Resistivity and estimated porosity"**). This variability may correspond to a turbidite-rich layer. At the boundary of Units II and III (830.4 m LSF) density shows a negative peak at 1.83 g/cm³. In logging Unit III, density decreases from 2.10 g/cm³ at 832.6 m LSF to 2.00 g/cm³ at the bottom of Unit III (935.6 m LSF). The data are much more scattered in logging Unit IV as a result of hole conditions. Density shows an increasing trend with depth, reaching a value of ~2.3 g/cm³ at 1366.4 m LSF.

Density-derived porosity

A porosity profile was calculated from the bulk density log (IDRO) (Fig. **F18**), using a constant grain density (ρ_g) of 2.65 g/cm³ and a water density (ρ_w) of 1.024 g/cm³ (see the **"Expedition 314 methods"** chapter). The density-derived porosity shows higher values than the neutron porosity in logging Unit I. The density-derived porosity and neutron porosity show almost the same value from 131 to 319 m LSF, and the density-derived porosity is ~10% lower than the neutron porosity to the bottom of the hole. The difference in values is especially marked in Unit II below Zone A (Zone B excepted) and in Unit III, which is clay-rich.

The density-derived porosity log is generally slightly less scattered than the neutron porosity log, except for intervals with large caliper measurements (i.e., 135.5–344.5, 481.6–547.1, and 935.6 m LSF to the bottom of the log). The discrepancy between the two porosities is also demonstrated in the cross-plot of density-derived porosity versus neutron porosity, which shows an overall positive correlation between the density-derived porosity and neutron porosity (Fig. **F19**). High porosity data mainly lie above the diagonal line and relatively low porosity data (≤55%) mainly lie below the diagonal line.

Neutron porosity

The TNPH log in Hole C0002A shows large scatter throughout the entire depth range (Fig. **F20**); therefore, the porosity data were smoothed using a 4.5 m running average to reduce the scatter. In logging Unit I, the porosity data show relatively high porosity (60%–75%) with high-frequency fluctuation. In logging Unit II, the porosity log shows a stepwise decrease from 63.3% to 49.2%. At the first step, the porosity log drops from 63.3% at 135.5 m LSF to 56.0% at 146.0 m LSF; thereafter, the log stays constant at ~56%. At the second step, the porosity log drops to 54% at ~262 m LSF and remains nearly constant until 547.1 m LSF (54.3%). The porosity log decreases from 54.3% to 50.0% across the 46.8 m interval from 547.1 to 593.9 m LSF then remains nearly constant at ~50% to the bottom of Unit II, with only small fluctuations around this value. Porosity slightly increases from 49.2% to 55.0% in Unit III (830.4–935.6 m LSF). In logging Unit IV, TNPH data show significant scatter and are affected by the hole conditions. The porosity log shows a decreasing trend with depth and reaches ~37.2% at the bottom of the log.

Resistivity and estimated porosity

Resistivity logs

Figure F10 shows a comparison of the caliper (CCAV) log, smoothed logs of the five different resistivity measurements (ring; bit; and shallow, medium, and deep button resistivity), and the smoothed result of the difference between shallow and deep button resistivity. A moving average using a 21-point (~3 m interval) window was used to smooth the resistivity values. Superposition of the deep, medium, and shallow button resistivity measurements shows generally good agreement among them. The logs show increasing resistivity values from the seafloor to the bottom of Zone A followed by a slight decreasing trend of resistivity to the top of logging Unit IV and an increasing trend to the bottom of the hole.

More systematic comparisons between resistivity logs were made through cross-correlations. Figure F21 shows bit and ring resistivity and shallow and deep button resistivity cross-plots. Contrary to Hole C0001D, the ring resistivity is generally lower than the bit resistivity. The difference between bit and ring measurements is ~0.3–0.5 Ωm for all the resistivity values.

The cross-plot between shallow and deep button measurements indicates that deep resistivity measurements are generally higher than shallow resistivity measurements. Figure F10 shows that the zones where deep resistivity values are significantly higher than shallow resistivity values correspond in most cases to intervals with large caliper values identified as possibly sand-rich layers (see **"Log characterization and lithologic interpretation"**). At the bottom of Zone A, some notable peaks showing relatively high deep resistivity values imply the presence of gas hydrate.

In logging Unit I, resistivity values gently increase from 0.8 to 1.1 Ωm. A stepwise increase from 1.1 to 1.4 Ωm is observed at the logging Unit I/II boundary. The top section of logging Unit II, above Zone A, shows relatively constant resistivity values of ~1.5 Ωm, reduced at depths between 200 and 218 m LSF. The resistivity values increase in Zone A from 1.5 to 2.6 Ωm, with a lower resistivity value excursion from 280 to 320 m LSF. It is noted that this lower resistivity zone is between (below and above) spikes of high resistivity values. Similar high resistivity spikes (up to 50 Ωm) are found at the bottom of Zone A and are interpreted as the signature of gas hydrate–rich intervals (see **"Log characterization and lithologic interpretation"**). The bottom of Zone A is marked by a net decreasing trend of resistivity values from 2.6 to 1.7 Ωm. The resistivity values are nearly constant in Zone B and the deepest part of logging Unit II, below Zone B (1.5 and 1.6 Ωm, respectively). The ring and the shallow, medium, and deep button resistivity signals become very noisy in Zone B and are scattered in patches below Zone B to the logging Unit II/III boundary. This scattering is likely to be linked to the presence of sand-rich layers. It is noted that most spikes in Zone B are negative (conductive), which is typical for sandy layers, whereas spikes in Zone A are mostly positive (resistive), representing a gas hydrate–dominated character. From 530 to 700 m LSF a decreasing trend of resistivity from 1.7 to 1.3 Ωm is observed followed by an increasing trend of resistivity from 1.3 to 1.5 Ωm. Logging Unit III is characterized by a slightly decreasing trend of resistivity from 1.5 to 1.4 Ωm and by a stable ring resistivity signal. The logging Unit III/IV boundary is marked by a decrease in resistivity from 1.4 to 1.1 Ωm. The upper section of logging Unit IV (from 936 to 1080 m LSF) is characterized by the general increase of resistivity from 1.4 to 2.1 Ωm. Below that section, the resistivity measurement is relatively constant at ~1.9 Ωm except for one zone of lower resistivity values (1.7 Ωm) between 1080 and 1140 m LSF and two zones of higher resistivity values (2.2 and 2.3 Ωm, respectively) at ~1220 and ~1300 m LSF.

Estimation of temperature profile

The temperature gradient was integrated from porosity-dependent rock thermal conductivity and estimation of temperature at the base of the gas hydrate zone.

The depth-dependent thermal conductivity (K) at this site was inferred using a geometric mean model, as follows:

$$K = K_g^{1-\phi} K_w^{\phi},$$

where K_g is the grain thermal conductivity (2.85 W/[m·K], from Leg 190 Site 1173) (Moore, Taira, Klaus, et al., 2001), K_w is the water thermal conductivity (0.60 W/[m·K]), and ϕ is the porosity. TNPH was used to estimate ϕ. Calculated K is ~1.25 W/(m·K) from seafloor to ~950 m LSF and ~1.5 W/(m·K) from ~950 m LSF to the bottom of the hole.

The temperature at the base of the gas hydrate zone (400.4 m LSF) was estimated at 22°C from the stability fields of gas hydrate (Kvenvolden, 1988).The resulting regional surface heat flow (Q) is 60 mW/m², as obtained from the integration of the thermal resistance between the surface and the base of the hydrate zone:

$$T = T_0 + Q\int_0^z \frac{dz}{K}.$$

Surface temperature (T_0 = 2°C) was assumed. The estimated heat flow is consistent with surface heat flow data. The in situ temperature profile was calculated using the same equation assuming the heat flow estimated above. The resulting temperature profile reaches 67°C at 1370.7 mbsf.

Estimation of porosity from resistivity

Seawater electrical resistivity was calculated using the temperature profile estimated above (see the **"Expedition 314 methods"** chapter) and was used to evaluate formation factor from both ring and resistivity logs. They are normally related to porosity by Archie's law. The Archie's law parameters that best fit the lower bound of the density-derived porosity are a = 1 and m = 2.4 (Figs. **F22, F23, F24**). It should be noted that lithologic variations not taken into account in this estimation could affect the resulting porosity, as well as the choice of Archie's law constants.

Resistivity-derived porosity generally decreases with depth (Fig. **F21**). In logging Unit I, resistivity-derived porosity decreases from 70% at the surface to 54% at its base. Within a 10 m interval at the top of logging Unit II, the resistivity-derived porosity jumps from 54% to 50% then decreases gradually to 47% to the top of Zone A. Resistivity-derived porosity further decreases within this zone to 33% at its base. The high ring resistivity peaks in this zone apparently generate negative resistivity-derived porosity peaks interpreted as intervals of gas hydrate occupying the pore spaces of the formation. At the base of Zone A the resistivity-derived porosity jumps from 33% to 40% within <7 m, corresponding to the BSR visible on the seismic sections. This apparent increase is almost certainly an artifact of the resistivity difference between hydrate-filled pore space and pore space filled with free gas rather than an actual change in porosity. From 406 m LSF to the base of logging Unit III (936 m LSF), resistivity-derived porosity decreases very slowly from 40% to 37%, corresponding to a gradient of ~0.6% per 100 m. Possible explanations for this very slow decrease could be the cementation of a somewhat sandy formation, the presence of fluid overpressure in an undrained material, increasing hydrous clay content downsection, or the result of lithologic variations. The resistivity-derived porosity gradient with depth increases to ~2.0% per 100 m in logging Unit IV, corresponding to the shallow part of the older accretionary prism. Resistivity-derived porosity reaches ~28% at the base of the hole.

P-wave velocity

The formations at this site can be divided into two main sections at 934 m LSF based on quality of the *P*-wave velocity log (Fig. **F25**): (1) upper formation of relatively good quality (quality level of 1–2) and (2) lower formation of relatively poor quality (quality level of 2–3) (see **"Data and log quality"**). There appears to be a significant discontinuity in physical properties at the boundary between the forearc basin (logging Units I–III) and the accretionary prism (logging Unit IV). The lower quality of the sonic logs in logging Unit IV can be attributed primarily to hole conditions.

No reliable formation velocity was measured in logging Unit I because of either mud arrival interaction (0–100 m LSF) or borehole washouts (~135 m LSF). Sonic *P*-wave velocity increases monotonically from 1600 m/s at the logging Unit I/II boundary to ~2000 m/s at ~380 m LSF. Velocity begins to decrease sharply at 380 m LSF through an interval below the BSR between 400 and 550 m LSF. Below this depth, velocity tends to gradually increase with depth with a few minor fluctuations. The low-velocity zones at 660 and 710 m LSF should be noted because sonic data at these depths are of high quality. Also noted is a nearly constant velocity (~2260 m/s) between 810 and 890 m LSF in logging Unit III, where muddy sediments are dominant. It is noteworthy that other physical properties such as resistivity, TNPH, and gamma ray values also remain almost constant in this depth interval. Directly above the logging Unit III/IV boundary, a notable low-velocity zone exists.

The quality of the sonic logs is poor in logging Unit IV. Thus, it is hard to define detailed characteristics of the sonic behavior in this unit. However, a strong increasing trend (1.33 m/s per meter) in V_P compared to that in the upper formations from 550 to 920 m LSF (0.73 m/s per meter) is noted. Values up to 3000 m/s or more were recorded in intervals of good data quality near the bottom of the hole.

Comparison of *P*-wave velocity with other properties

In this section, we compare V_P with resistivity (Fig. **F26**) and estimated porosity (Fig. **F27**). Figure **F26A** shows a cross-plot between V_P and bit resistivity. The entire data set in this cross-plot (except the mud arrival at 1500 m/s) produces three main subsets depending on the velocity-resistivity relation: (a) formations above the BSR (~400 m LSF, indicated by purple and light blue), (b) formations below the BSR (red and orange), and (c) accretionary prism (green). Note the remarkable difference in slopes between (a) and (c). The formations above the BSR (a) are characterized by a significant increase in resistivity but a minimal increase in velocity with depth, resulting in a gentle slope in the velocity-resistivity relation. In

the prism (c), both velocity and resistivity increase with depth, resulting in a moderate slope in the velocity-resistivity relation. The data cluster for the formations below the BSR (b) has a negative slope resulting from the decrease in resistivity while velocity increases with depth, connecting the two subsets (a) and (c). Such a trend is more clearly visualized in Figure **F26B.** Both velocity and resistivity decrease with depth immediately below the BSR over a 100 m interval. Velocity then increases with depth, but resistivity continues to decrease and stays constant to the logging Unit III/IV boundary.

P-wave velocity and porosity relationships are presented in Figure **F27.** Four different porosity logs (TNPH, density-derived porosity, and bit and ring resistivity–derived porosities) are cross-plotted with *P*-wave velocity. Clearly, there are some differences in values between differently derived porosities. See relevant descriptions for individual porosities in **"Physical properties"** in the "Expedition 314 methods" chapter.

Whereas all four plots show a general agreement in trends of decreasing porosity with increasing velocity, there are slight differences in fitting data for individual formations. For example, the gas hydrate–bearing formations (indicated with light blue) tend to have different patterns of resistivity-derived porosities from those of other porosity data, such that the slope of the relationship is relatively low. It is mainly because resistivity-derived porosity is biased toward higher resistivity values in the gas hydrate–bearing formations. The velocity-porosity relationship for the accretionary prism is markedly scattered for density-derived porosity. The relationship for the prism is quite well constrained for both resistivity-derived porosities, simply because the resistivity-derived porosities themselves vary less than the noisy density-based values.

Structural geology and geomechanics

Our interpretations of structure and in situ stress are derived from resistivity images in Hole C0002A (see the **"Expedition 314 methods"** chapter). We used a variety of images for the interpretation, including shallow, medium, and deep depths of investigation and several static and dynamically normalized images. Final interpretation was based on the shallow image. Data quality is good for the majority of the hole. See the **"Expedition 314 methods"** and **"Expedition 314 Site C0001"** chapters for comments on uncertainties and methods in picking features and in differentiating bedding and fracture planes. Where possible, the level of uncertainty of interpretation is provided in the text and figures of this chapter. Caliper data were not directly integrated with the resistivity images but were considered during interpretation.

Site C0002 penetrated both the forearc basin and the underlying older accretionary prism; therefore, the structural character of these two major units can be compared (Fig. **F28**). We also compare structural aspects of this site with Site C0001.

Bedding

Bedding dips contrast clearly between the forearc basin, with mostly shallow dips (≤15°), and the underlying prism, with markedly steeper dips (~30°–60°) (Figs. **F28, F29**). The shallow dips of the forearc basin make identifying and accurately determining dip and strike difficult, and this should be considered in the following interpretation. Our interpretation results, however, show that the poles to the bedding planes in the basin are highly concentrated and their trends generally agree with the regional bedding parameters defined by the three-dimensional (3-D) seismic data volume (Fig. **F29**), suggesting sufficient reliability. See **"Discussion and synthesis"** for comparisons of borehole image and seismic data.

The forearc basin is divided into three logging units (Figs. **F28, F29**). The majority of beds in logging Unit I trend northeast to east and dip to the south (<4°). Logging Unit II beds appear to trend approximately northeast–southwest but with some scatter in azimuth and dipping (<8°), both toward the north and south. Logging Unit III beds also trend northeast–southwest but are more variable in azimuth and dip magnitude, with dips to both north and south. Bedding dips increase in the lower half of logging Unit III (Fig. **F30**). For the structure of logging Unit III, see the next section.

The stratigraphy of the underlying prism (logging Unit IV) is more deformed with steeper dips (~18°–60°) and a dominant northeast–southwest trend (Fig. **F29**). The poles to the bedding of this unit have two clusters on the stereonet (Fig. **F29B**). One highly scattered cluster dipping to the south approximately corresponds to the shallow beds (~1120 m LSF), and the other less scattered one dipping to the north corresponds to the deeper beds.

Structure of logging Unit III (forearc basin–prism transition)

Logging Unit III is distinguished from other units by its lithologic homogeneity and distinct gamma ray and PEF signature and is interpreted as a homogeneous mud deposit (see **"Log characterization and**

lithologic interpretation"). Structurally it also contrasts with logging Units II above and IV below (Fig. F30). Borehole breakouts, which occur throughout most of the hole, are very weakly developed within this unit, possibly as a result of sediment properties. The base of this unit (lower ~30 m) is characterized by a number of steeply dipping resistive fractures (Fig. F30).

Bedding is difficult to discern, but beds in the middle zone (870–910 m LSF) dip to the south at up to 25°, whereas beds in the lowermost 10 m of the unit dip to the north (<16°).

Natural fractures

Fractures were less common at this site compared with Site C0001 within the active accretionary prism. Fractures have been analyzed according to azimuth and conductivity and are classified into four types: (1) conductive, (2) resistive, (3) undefined conductivity, and (4) uncertain fractures. Most fractures only show a partial sinusoid in the borehole images, often preventing accurate determination of strike and dip. In some cases, these fractures have been classified as "uncertain" fractures (e.g., Fig. F28), as there is a small possibility that they are not real features. Uncertain fractures are not differentiated according to conductivity but are mostly conductive. In some cases, fracture conductivity cannot be defined because of small fracture aperture or little/variable resistivity contrast with surrounding sediments, hence the fracture class "undefined conductivity." Fracture frequency (Fig. F31) indicates increased deformation in the prism (below 936 m LSF) relative to the forearc basin.

Fractures in the forearc basin are both resistive and conductive, but mostly conductive if all uncertain fractures are included (Figs. F28, F32C). In the fractured base of the forearc basin (logging Unit III), fractures are resistive (Fig. F30). The majority of better defined fractures within the prism (logging Unit IV) are also resistive but more mixed in conductivity if "uncertain" fractures are included.

Analyzing the entire hole, the fractures exhibit scatter in trend but with dominant trends of northeast–southwest and northwest–southeast (Fig. F32C). Fractures of the forearc basin (logging Units I–III) are highly scattered (Fig. F32A). However, trends of northeast–southwest to east–west may be present. Uncertain fractures show a clear northwest–southeast trend. A few of the forearc basin fractures, with orientations northeast–southwest and east-northeast–west-southwest, offset bedding planes with normal offset (Fig. F33). Higher fracture densities occur in the upper 200 m of the forearc basin and within logging Unit III (Fig. F31).

Prism fractures (logging Unit IV) are more difficult to differentiate from bedding but show much less scatter than the forearc basin and a dominant northeast–southwest trend with a minor northwest–southeast trend (Fig. F32B). Examples of conductive prism fractures are shown in Figure F34. Fracture dips are not significantly steeper than those in the basin (~30°–85°). Many of the fractures are bedding parallel within this unit. Several large-aperture (10–30 cm) highly resistive fractures were observed within the prism, and we interpret these as cemented or mineralized. These features were interpreted as fractures, not bedding, because of their extreme resistivity.

Borehole breakouts

Breakouts were common throughout Hole C0002A (e.g., Fig. F33) and present in both the forearc basin and underlying older accretionary prism. Interestingly, the breakout orientation is approximately the same in these two distinct units (Figs. F28, F35A). No tensile fractures were observed. The average azimuth of breakouts is ~135° (northwest–southeast) with a range of 080°–170°, indicating that S_{Hmax} is oriented northeast–southwest (045° or 225°). This orientation is at ~90° to that at Site C0001 in the megasplay fault zone or outer arc high. Breakout widths range from 10°–170° but with a modal range of ~20°–40° (i.e., at the lower end of the total range) and an average of ~60° (Fig. F35B).

In detail, breakout parameters (azimuth and width) vary slightly with depth (Fig. F36). Figure F36A illustrates azimuth varying nonlinearly downhole, generally from a mean of 120° in the upper forearc basin to a mean of 145° in the lower part of the prism penetrated by the borehole. The most dramatic change in orientation occurs at ~1200 m LSF from 125° to 140°. The general change in azimuth downhole is likely a result of changes in the stress field, but local variability on the 50–200 m depth scale may be related to sediment properties around the borehole. Breakout width (Fig. F36B) shows a distinct increase at ~1000 m LSF near the top of the old accretionary prism material, which might be related to physical properties of the borehole sediments and/or related drilling parameters (e.g., borehole pressure).

Stress magnitude analysis from breakout widths

A preliminary attempt to constrain stress magnitude based on breakout widths was carried out at two depths (900 and 1300 m LSF). These two depths were chosen because rock types were relatively well identified from multiple logs and the states of stress may be different at depths above and below the major

forearc basin/prism boundary. Average widths of borehole breakouts are 34° and 85° at the respective depths.

Formation pressure at each depth was assumed to be hydrostatic. Figure F37 shows stress polygons for the two depths, in which the drilling-induced tensile fracture criterion (indicated by a red line) and rock uniaxial compressive strength (UCS) lines (indicated by blue lines) are plotted. Each blue line represents a trace of S_{Hmax} and S_{hmin} that is required to create the observed widths of borehole breakouts for a given UCS value. Because no drilling-induced tensile fractures were observed at Site C0002, S_{Hmax} and S_{hmin} must lie within the stress polygon to the right of (below) the red line and along a blue line representing rock strength.

Reliable information on rock strength is essential for this analysis. Since no known rock strength data are available in this area, an indirect estimation of rock strength was attempted using a series of empirical relationships that relate velocity or porosity to UCS (Chang et al., 2006). These relations are calibrated for high-porosity shale and sandstones from the Gulf of Mexico and North Sea, which might have undergone a different compaction and diagenetic history from the rocks of the Nankai forearc. Thus, the estimated UCS values here are subject to uncertainty and await corrections using data from subsequent expeditions.

The values of UCS were estimated to be 5.1 ± 3.9 MPa (shale at 900 m LSF) and 11.9 ± 1.7 MPa (sandstone at 1300 m LSF). Based on these estimated UCS values, the state of stress at 900 m LSF is a normal fault stress regime ($S_{hmin} < S_{Hmax} < S_v$) and that at 1300 m LSF is categorized to be either a strike-slip fault or a thrust fault stress regime.

Discussion and conclusions

Comparisons between borehole analysis of structure and seismic reflection data

Bedding in the 3-D seismic data set shows gentle dips in the Kumano forearc basin sediments, and this agrees with the structural style in the resistivity images (Fig. F29). Forearc basin bedding orientations from borehole data are generally compatible with those imaged by seismic reflection data (Table T6) with a northeast–southwest strike. Prominent seismic scale horizons in logging Unit I strike northeast–southwest and dip south, which agrees generally with small-scale bedding from the borehole. Logging Unit II beds strike northeast–southwest and dip mostly to the north in seismic data. The strike is consistent in borehole data, but dip directions are more scattered. This may be due to difficulties in resolving low-angle features or to some difference between bedding at two different scales.

Logging Unit III represents the lowermost forearc basin sediments and appears to be divided into two subunits in seismic reflection data (Fig. F14). The lower of these two subunits lacks continuous seismic reflectors and coincides with more intensive fracturing from resistivity images (Fig. F30). The two seismic units of this logging unit have contrasting dip directions: the upper dipping north and the lower dipping south. Borehole bedding interpretations (Fig. F30) show northeast–southwest trends and more scattered dip directions (north and south) but with a more consistent southeasterly dip direction and increased dip magnitude in the lower half of the unit (below ~870 m LSF), except for the basal 10 m where dips decrease again. This also generally agrees with the seismic data.

Within the prism, both seismic and borehole interpreted beds dip more steeply than the basin above and strike approximately northeast–southwest. The scattered azimuth and dip of the borehole beds suggest a strongly deformed structural style of the prism, which cannot be clearly imaged in the seismic profiles.

Seismic reflection data show clear normal faulting within the forearc basin (Figs. F14, F38) with trends from east–west to northeast–southwest and predominantly dipping to the north. There is another set of faults identified in time slices, with some displacing the seafloor, with a northwest–southeast trend. These seismic scale faults can be correlated with the forearc basin fractures identified in resistivity images, (i.e., those with northeast–southwest to east–west trends and northwest–southeast trends [uncertain fractures]) (Fig. F32A).

The orientation of possible faults within the upper prism has not been determined from seismic reflection data, although some of the northeast/east-trending normal faults in the basin may extend into and offset parts of the upper prism. If we presume that the tectonic setting has remained similar for the last few million years, then we might expect old compressional structures within the older prism unit with similar trends to the active prism (i.e., northeast–southwest), as observed in the borehole fracture data set at this site (Fig. F32B). It is possible that some of these structures may have been reactivated as other fault/fracture types in the present stress regime or, alternatively, these structures may be inactive prism fractures.

Stress magnitude implications for deformation style

Stress magnitude estimations from borehole breakout widths, compressive strengths, borehole pressures, and friction coefficients suggest different stress regimes within the forearc basin and prism (Fig. F37). At ~900 m LSF, the base of the forearc basin, normal faulting would be expected. In this case, the maximum principal stress would be vertical and the minimum principal stress would be to the northwest. This is generally consistent with the observed seismic scale faulting and with evidence of normal offset by borehole scale fractures trending ~northeast–southwest. At ~1300 m LSF, within the prism, the estimated state of stress conditions favor either strike-slip or thrust faulting. However, if the empirical equations have overestimated UCS, normal faulting is also possible. So the faulting stress regime is not well constrained in the older prism. Conceivably, the following deformation styles are geologically possible and plausible from the predicted state of stress in the prism:

- Normal faulting and extension similar to the overlying forearc basin, with faults extending into the upper prism, possibly reactivating old thrust faults with favorable orientation;
- Strike-slip faulting accommodating some component of margin-parallel deformation; and
- Thrust faulting but with northwest–southeast fault trends (perpendicular to the margin) resulting from the orientation of S_{Hmax}.

The latter style of deformation, however, is not compatible with northeast–southwest borehole fracture orientations in the prism. If the strike-slip or thrust faulting stress regime dominates, then S_{Hmax} is also the maximum principal stress and trends parallel to the strike of the margin and prism. Ground-truthing by coring will reduce the uncertainty in the parameters for determining stress state and magnitude, which may allow these hypotheses to be tested.

Comparison of in situ stress and deformation between Sites C0001 and C0002

In situ stress indicators (borehole breakouts) suggest S_{Hmax} is rotated by ~90° at Site C0001 relative to Site C0002 located to the southeast, which is compatible with the northwest–southeast to north–south extension observed in the forearc basin. This abrupt change in stress regime over a short distance (~10 km) may represent the transition from the actively shortening prism to the relatively static landward part of the forearc. This corresponds well to the models of Fuller et al. (2006) and to some extent Wang and Hu (2006) that predict high strain rates within the active critical wedge ("outer wedge") and relatively little deformation in the stable "inner wedge" (beneath and within a sediment-filled forearc basin). At the latter location, the convergence-related deformation is thought to be focused on the plate boundary at depth. The transition between the inner and outer wedges, which should be between Sites C0001 and C0002 based on deformation and morphology, is proposed to mark the approximate updip limit of the seismogenic zone (Wang and Hu, 2006). During the interseismic period, Wang and Hu (2006) predict compression in the inner wedge, which we do not observe. This may be due to the proximity of Site C0002 to the inner-outer wedge transition zone, shallowness of the borehole (so not sampling the true stress state of the inner wedge), variations in coefficient of friction along the plate boundary, or other problems with the model.

Extension within the forearc basin and potentially the underlying prism can be explained by gravitational collapse and downslope extension as movement on the outer arc megasplay fault zone causes uplift and backtilt of the seaward part of the basin (inner wedge). Another example of a forearc basin extending perpendicular to the margin is northern Cascadia, USA, where underlying overpressured prism melange drives downslope migration and extension of basin sediments (McNeill et al., 1997).

The gradual rotation of breakout orientations and therefore S_{Hmax} with depth at Site C0002 (Fig. F36) suggests that such a change could continue with depth to the megasplay fault or décollement where in situ stress might be expected to reflect plate convergence.

Log-seismic correlation

Kumano Basin seismic stratigraphy

A series of seismic units lie within the southwestern Kumano Basin in the area imaged by the Kumano 3-D seismic volume (Gulick et al., 2007; Moore et al., 2007). These seismic units (Fig. F14; Table T6) show the evolving uplift within the southwestern basin and in places can be correlated to specific features within the logs. To aid correlation of bedding strike and dip observed in the image logs, we report the dip and dip directions for each of the sequence boundaries that separate our defined seismic units (Table T6).

Seismic Unit Kumano 2/3/4 (undifferentiated) appears to dip to the southeast based on the dip of the underlying horizon, Top of Kumano 5. In contrast, the underlying seismic Units Kumano 5–11 all dip to the northwest, based on their sequence boundaries. As the Kumano Basin sequences were deposited,

there appears to have been a gradual shift from more northward dip direction in the oldest sediments to more northwestward dips in the younger sequences, ending with the deposition of Kumano 5. Kumano 5 shows lower dip than the underlying sequences. Lastly, at the base of the sequence is an angular unconformity between the Kumano Basin units and a seismic unit called Lower Sediments 1. The unconformity dips to the southeast, whereas the underlying horizon, Top of the Accretionary Prism, dips to the north (Table T6); therefore, the dips of individual strata within seismic Unit Lower Sediments 1 may vary (Fig. F14).

Overall log unit correlation

Logging Unit I (Fig. F14) corresponds to seismic Unit Kumano 2/3/4 (undifferentiated) (Gulick et al., 2007). Depths to the boundaries of the seismic units and their structural orientations are shown in Table T6. The structural orientations of the faults near the borehole are shown in Table T6. Logging Unit I appears to consist of hemipelagic sediments that dip <1° to the southeast (Fig. F14). The base of logging Unit I correlates with the positive peak below an unconformity in the seismic data. We mapped this unconformity using the positive peak at the top of the unconformity and named it horizon Top of Kumano 5. The interval between the base of logging Unit I and horizon Top of Kumano 5 is ~30 m; however, the difference may arise from which peak or trough is selected to trace the top of seismic Unit Kumano 5. This boundary is subjective enough to allow for a 30 m difference.

Logging Unit II (Fig. F14) corresponds to the majority of seismic Unit Kumano 5, all of Units Kumano 6–10, and a portion of Unit Kumano 11. These are older forearc basin sediments, now dipping gently to the northwest, as will be discussed below in greater detail (Table T6). Included within logging Unit II are a prominent BSR, a north-northwest–dipping normal fault, an interval of interpreted gas hydrate, an interval of negative polarity reflection suggestive of trace amounts of free gas at the base of the BSR, and a dipping negative polarity reflection deeper than the BSR that also suggests the presence of free gas.

Although there is an obvious unconformity in the seismic data between seismic Units Kumano 11 and Lower Sediments 1 that suggests a hiatus across the boundary, there appears to be little lithologic or physical property contrast. Therefore, logging Unit III (Fig. F14) corresponds to the middle part of the northwest-dipping seismic Unit Kumano 11, the onlap of Kumano 11 onto the top of southeast-dipping seismic Unit Lower Sediments 1, and the Lower Sediments 1 strata. Logging Unit IV (Fig. F14) corresponds to the drilled portion of the old accretionary prism. The seismic data show that the top of the prism is a rough surface that is difficult to pick definitively everywhere but locally produces a bright low-frequency reflection. The abrupt changes in most of the logs at ~947 m LSF seem likely to accurately locate the top of the accretionary prism.

To facilitate discussions involving the correlation of log and seismic reflection data at this site, we present a series of figures (Figs. F39, F40, F41, F42, F43, F44, F45) in which we have superimposed logs over a portion of the check shot–corrected prestack depth migrated (PSDM) seismic reflection profile. The seismic reflection profile was produced by converting the PSDM profile from depth to time using the PSDM velocity model, and converting the PSDM time section from time to depth using the velocity depth function obtained from the check shot survey at this site. This process should yield the best seismic profile to compare to logs and to estimate the depths to significant stratigraphic and structural features (Table T6).

Log-seismic correlation in zones of interest

Logging Unit I/II boundary

The strata of logging Unit I, which in general correlates with seismic Units Kumano 2/3/4 (undifferentiated) (Fig. F14), show local evidence of erosion and normal faulting. The boundary between logging Units I and II likely correlates with the top of seismic Unit Kumano 5 despite the depth difference, as discussed above (Fig. F46A). *P*-wave velocity increases at the boundary (Fig. F46B), suggesting a transition from higher to lower porosity hemipelagic sediments (possibly the result of compaction and consolidation). The gamma ray value abruptly increases to a higher value in logging Unit II than that in Unit I (Fig. F46C), suggesting that the top of seismic Unit Kumano 5 is an abrupt boundary.

Zones A and B in logging Unit II

The base of Zone A matches exactly with the BSR in the seismic section (Fig. F47A). This boundary is clearly indicated by high resistivity above the BSR in Zone A and lower resistivity below (Fig. F47B), suggesting the existence of gas hydrate in Zone A. *P*-wave velocity beneath the BSR is lower than that in Zone A (Fig. F47C), which is consistent with the presence of trace amounts of free gas.

The upper boundary of Zone B corresponds to a bright reflection with negative polarity that dips to the northwest (Fig. F47A). Regionally it is a high-amplitude, negative polarity reflection only below the depth of the BSR, and the seismic image is poorly focused in the same region (see Fig. F4 in the "Expedi-

tion 314 summary" chapter). Zone B correlates with a low *P*-wave velocity zone beneath a zone of higher velocity (Fig. F47C), suggesting that Zone B may be a zone of permeable coarser sediments where small amounts of free gas may be migrating updip.

Logging Unit III/IV boundary

The boundary between logging Units III and IV corresponds to the seismic reflection Top of Accretionary Prism (Figs. F14, F48A). This major boundary lies between the basin sediments and the apparent older accreted sequence. The PEF log curve shows a significant change at the boundary, with a larger value above and lower value below (Fig. F48B). The gamma ray curve exhibits a zone of low values at the top of logging Unit IV (Fig. F48C), suggesting that a sandy interval may lie near the top of accretionary prism, aiding in the generation of a strong seismic reflection.

Structural orientations from seismic observations

In order to allow accurate correlation between the regional seismic observations of faults and stratigraphy and the observations in the logs, we computed orientations for features of interest. For these calculations, we used the prestack time-migrated seismic volume combined with the velocities provided by the check shot data. We used the horizontal plane (time slice) at 2888 ms, the depth where Hole C0002A intersects a normal fault, to determine the strikes of nearby faults, and we generated seismic sections from the 3-D volume oriented in the direction of maximum fault dip to determine their respective dips. The accuracy of the reported strikes and dips for the faults near Site C0002 is estimated at ±5° based on the velocity-based errors inherent in using the prestack time-migrated volume and the human error of determining the exact strike along a curved fault plane. Dip directions for horizons were determined by digitizing a 100–400 m long transect centered on the borehole orthogonal to the two-way traveltime contours of each horizon. The dips were then calculated from the end points of these digitized transects with time to depth conversion computed using the check shot velocities. The estimated error for the reported dips for the seismic horizons close to the borehole is ±1°, whereas the estimated error in the dip direction is ±5°. The dips within the prism are less reliable because of the reflections being laterally discontinuous and affected by migration algorithms; therefore, the error is estimated at ±5°.

The southern boundary of the Kumano Basin is cut by numerous normal faults (Fig. F38), and Site C0002 penetrated one of these faults at 253 m SSF (Table T6). The trend of these faults changes along strike. However, near Site C0002 three of four faults show remarkably consistent strikes and dips (Table T6). These faults all strike east-northeast, whereas a potentially older fault strikes more northeast (Table T7; Fig. F38). Regionally there are distinct fault populations, including a dominant population of normal faults striking east-northeast, a smaller population striking northeast, a few faults related to the seafloor depression to the south (Fig. F38) that strike east, and a few faults striking northwest. This last population may be responsible for accommodating some of the 3-D complexities of the basin. The east–west striking faults close to the seafloor depression are either near vertical or dipping south (Martin et al., 2007).

Check shot survey and vertical seismic profile data

A very complete check shot survey was acquired at Site C0002. One-way traveltime seismic records were obtained at 72 depths from the seafloor to 1355 m LSF in Hole C0002A (Fig. F49). Of these observations, 63 were of adequate signal strength to be used in the check shot analysis (Table T8). Data were acquired during each pipe connection as the pipe was lowered and as it was pulled out of the hole. Each depth observation involved acquiring and stacking multiple shots, typically 15 per observation on the way down and 8 per observation on the way up. Noisy traces and traces with poor first arrival waveforms were deleted or edited. The remaining traces were filtered (trapezoidal, zero phase, and 30-40-150-200 Hz band-pass) and stacked to produce the traces shown in Figure F48. The first arrival wavelet is unambiguous on all traces, although noise makes identifying the true first break difficult on a few of the traces.

The first arrival times were picked manually. These are the "raw first arrival" times in Table T8. We applied a damped least-squares inversion to the observed depth/time data (Lizarralde and Swift, 1999). This inversion determines a smooth velocity depth curve by varying the arrival times by amounts that are within the data uncertainty. We estimated the uncertainty of the arrivals to be ~1 ms. We used an inversion damping coefficient of 0.05 because it produced a χ^2 value consistent with the optimal balance between over- and underfitting the data. The smoothed interval velocities and adjusted arrival times are shown in Table T8. We used the smoothed first arrival times and the observation depths as the check shot function, which we then used for the time-depth correction of seismic reflection profiles and synthetic seismogram preparation.

The smoothed interval velocity curve and sonic log interval velocity data are generally similar (Fig. F50). The most significant difference between the two is between ~550 and 675 m LSF, where the check shot velocity is 100–200 m/s lower than the sonic log velocities. The discrepancy in this interval may be a result of the smoothing method applied to the check shot arrival times. Both curves show a general pattern of steep increases of velocity separated by intervals of approximately constant velocity. There appear to be ~4 such cycles in the hole. The check shot velocities show a low-velocity zone that has a lowest point at ~540 m LSF.

We also obtained a near-zero offset VSP using the check shot data (Fig. F51). In the VSP, we observe clear upgoing reflection arrivals originating from the seafloor to the top of the accretionary prism. The signal-to-noise ratio is not high for these arrivals, but they seem to correlate reasonably well with packages of reflections in the seismic profile at the site.

Synthetic seismogram

In order to construct a synthetic seismogram for Site C0002, we used the IDRO log and the sonic (DTCO) log. The density log was edited to remove densities associated with density-derived caliper values (DCAV) of 9.5 inches or larger and DTCO. It should be noted that we later learned that the ultrasonic caliper (HORD) might have been superior to the density-derived caliper as a log to filter density values, but the change in the result of the synthetic seismogram would likely be inconsequential and not worth the effort of repeating the calculations. Because both the density and sonic logs have gaps in them, we used a 51-point running average over the gaps in the logs to fill them in. Where the gaps were greater than ~50 points, we linearly interpolated between the final running averaged values within each gap. Because of the high caliper values for the seafloor and uppermost sediments, where we were jetting-in, we created a seafloor curve shaped similar to that observed in Hole C0001C with values derived from the highest recorded IDRO densities in Hole C0002A.

The resulting synthetic seismogram correlates with the observed reflections in the seismic data in some intervals such as at the BSR (404 m SSF) (Fig. F52). However, both on the edges of the longer gaps in the logs and at locations where high caliper values correlate with low gamma ray values, the gap-filling process introduced artifacts. In some cases, the artifacts were false reflections produced in the synthetic seismogram. In other cases, expected reflections are not produced. A variety of smoothing, editing, and filtering techniques were tested, but a highly correlated synthetic seismogram was not achieved.

Discussion and synthesis

The goal of drilling at this site was to log the ~1000 m thick Kumano forearc basin section and several hundred meters of the underlying formations, interpreted as older rocks of the accretionary prism and/or early slope basin sediments deposited prior to the development of the megasplay fault. We were able to drill and log the entire section from 0 to 1401 mbsf with 100% success. An excellent suite of logs and seismic VSP data reveal the structure of the forearc basin, gas hydrate–bearing zone, and the underlying deformed rocks of the inner accretionary prism.

Site C0002 is slated for riser drilling across the entire plate boundary system to >5500 mbsf during later stages of the NanTroSEIZE project. Similar to Site C0001, which is planned for riser drilling to 3500 mbsf, it is important for the installation of the blowout preventer on the seafloor and a few hundred meters of 20 inch casing pipe to obtain geotechnical properties in the upper sections. In addition, *P*-wave velocity structure in the prism, which is essential for a precise estimate of the depth to the seismogenic fault zone, has been determined using the 3-D seismic survey (Moore et al., 2007) but still needs to be calibrated using in situ data. Using continuous drilling and logging to 1401 mbsf, we obtained data that can serve to prepare for future riser drilling.

The hole was tagged at 1936 mbsl and was jetted-in to 70.5 m LSF. Approximately 3 days of drilling time (excluding ~0.5 days of wiper trip and other down time) was required to reach TD (1401 m LSF) without any significant difficulties. The average rate of penetration was ~30 m/h. All LWD tool memory data were successfully downloaded. In spite of several major washouts (stand-off > 2 inches) in sand-rich intervals, log data quality is generally good, and image logs in particular are of high quality. These logs provide a rich data set for interpretation of the geology and stress conditions at this site.

Four logging units bounded by dip discontinuities interpreted as angular unconformities were identified. Logging Unit I (0–135.5 m LSF) is the youngest of the slope basin deposits at this site. Logging Unit II (135.5–830.4 m LSF) is interpreted as thick basin fill marked by numerous turbidite deposits, as seen clearly on the log responses, particularly the gamma ray log. Logging Unit III (830.4–935.6 m LSF) is a homogeneous clay-rich interval of mudstone immediately overlying the top of the older accretionary prism section that forms basement to the forearc basin at 936 m LSF. Logging Unit IV (936–1401 m LSF) corresponds to the accretionary prism imaged on the seismic profiles, with a distinct change to much more variable responses in virtually all of the logs.

Kumano forearc basin features

The Kumano forearc basin is composed of logging Units I–III, or 13 seismic units (Kumano 2–13 and Lower Sediments). Bedding dips are shallow (<15°) in the forearc basin and increase downhole toward the base of the section. All fractures dip between 30° and 85° with no significant difference between basin and prism. Basin fractures have three dominant trends: (1) northeast–southwest, (2) east–west, and (3) northwest–southeast. All three orientations can be identified in faults imaged in seismic data. A few basin fractures offset bedding in a normal sense, consistent with the seismic-scale normal faulting.

Within logging Unit II are two zones of particular interest defined by changes in the log responses. Zone A (218.1–400.4 m LSF) is interpreted as a gas hydrate–bearing zone based on the resistivity profiles, with the hydrates concentrated in the sandy bases of the turbidite deposits. Velocity and density decrease at the BSR, suggesting that the reflection may be generated by the presence of small amounts of free gas below.

Zone B (481.6–547.1 m LSF) is interpreted as an interval in which the sandy horizons of the turbidite deposits are potentially gas-bearing. At the top of Zone B, a strong, dipping, negative polarity reflection in the seismic data correlates with a low-velocity region in the sonic log. The regional observation that some reflectors brighten in amplitude as they approach the BSR from below, coupled with interpreted sandy turbidite layers based on gamma ray logs of Zone B, supports the suggestion that this reflection may represent sands bearing at least small amounts of free gas.

The lower part of the forearc basin below 400 m LSF at the BSR is characterized by physical properties that suggest changing lithology, relative undercompaction, or other effects: slightly decreasing or nearly constant resistivity with depth, whereas velocity increase is insignificant and changes in density and porosity are relatively limited.

Logging Unit III, at the basin–prism transition, is a homogeneous clay-rich interval of mudstone and is characterized by increasing bedding dips and a fractured base.

Old accretionary prism features

Logging Unit IV from 936 to 1401 m LSF corresponds with the chaotic reflectivity imaged on the seismic profiles and interpreted as the inner older accretionary prism, with a high-amplitude reflection and a distinct change to much more variable responses in virtually all of the logs. A sequence of low gamma ray values just below the top of the prism suggest that a sandier interval may contribute to this bright reflection.

Physical properties not sensitive to hole condition (e.g., bit and deep resistivity) suggest that the accretionary prism is denser and more compacted than the forearc basin.

Bedding dips increase within logging Unit IV (~30°–60°). Clearly imaged natural fractures are rarer than at Site C0001 and have scattered orientations within the basin but a more consistent northeast–southwest trend within the prism. All fractures dip between 30° and 85° with no significant difference between basin and prism. Resistivity of the fractures is varied, but includes several wide aperture (10–30 cm) and highly resistive (mineralized or cemented) fractures in the prism.

Stress field and tectonics in the Kumano Basin

Whereas the structural styles of the forearc basin and underlying accretionary prism at Site C0002 are different, the orientations of bedding planes and borehole breakouts are consistent, northeast–southwest and northwest–southeast, respectively, throughout the entire borehole.

Borehole breakouts indicate a northeast–southwest oriented S_{Hmax}, nearly perpendicular to that at Site C0001. Breakout azimuth gradually rotates clockwise with depth and breakout width increases in the prism relative to the basin. Stress magnitude determined from breakout width is consistent with observed dominance of normal faulting in the basin but is more ambiguous in the prism. Fracture and fault orientations, breakouts, and state of stress collectively support margin-normal extension of this part of the forearc. We suggest this is driven by uplift of the megasplay/outer arc high causing gravitationally driven extension of the inner prism. This contrasts with Site C0001 in the active outer prism where convergence-related compression dominates.

References

Chang, C., Zoback, M.D., and Khaksar, A., 2006. Empirical relations between rock strength and physical properties in sedimentary rocks. *J. Pet. Sci. Eng.,* 51(3–4):223–237. **doi:10.1016/j.petrol.2006.01.003**

Fuller, C.W., Willett, S.D., and Brandon, M.T., 2006. Formation of forearc basins and their influence on subduction zone earthquakes. *Geology,* 34(2):65–68. **doi:10.1130/G21828.1**

Gulick, S.P., Bangs, N.L., Moore, G.F., Martin, K., Nakamura, Y., Kuramoto, S., Tobin, H.J., and Taira, A., 2007. Uplift and deformation of the Kumano forearc basin: preliminary results from Nankai Trough 3D seismic

imaging offshore Kii Peninsula, Japan. *Eos, Trans. Am. Geophys. Union,* 88(52):T53A-1118. (Abstract)

Kvenvolden, K.A., 1988. Methane hydrate—a major reservoir of carbon in the shallow geosphere? *Chem. Geol.,* 71(1–3):41–51. **doi:10.1016/0009-2541(88)90104-0**

Lizarralde, D., and Swift, S., 1999. Smooth inversion of VSP traveltime data. *Geophysics,* 64(3):659–661. **doi:10.1190/1.1444574**

Martin, K.M., Gulick, S.P., Bangs, N.L., Moore, G.F., Kuramoto, S., Tobin, H., and Taira, A., 2007. Preliminary analysis of an anomalous bathymetric "notch" between the Kumano forearc basin and the slope of the Nankai Trough accretionary prism. *Eos, Trans. Am. Geophys. Union,* 88(52):T53A-1115.

McNeill, L.C., Piper, K.A., Goldfinger, C., Kulm, L.D., and Yeats, R.S., 1997. Listric normal faulting on the Cascadia continental margin. *J. Geophys. Res.,* 102(B6):12123–12138. **doi:10.1029/97JB00728**

Moore, G.F., Bangs, N.L., Taira, A., Kuramoto, S., Pangborn, E., and Tobin, H.J., 2007. Three-dimensional splay fault geometry and implications for tsunami generation. *Science,* 318(5853):1128–1131. **doi:10.1126/science.1147195**

Moore, G.F., Taira, A., Klaus, A., et al., 2001. *Proc. ODP, Init. Repts.,* 190: College Station, TX (Ocean Drilling Program). **doi:10.2973/odp.proc.ir.190.2001**

Rider, M.H., 1996. *The Geological Interpretation of Well Logs* (2nd ed.): Caithness (Whittles Publishing).

Tobin, H.J., and Kinoshita, M., 2006. NanTroSEIZE: the IODP Nankai Trough Seismogenic Zone Experiment. *Sci. Drill.,* 2:23–27. **doi:10.2204/iodp.sd.2.06.2006**

Ujiie, K., Hisamitsu, T., Maltman, A.J., Morgan, J.K., Sánchez-Gómez, M., and Tobin, H.J., 2003. Deformation structures and magnetic fabrics at Site 1178: implication for deformation history recorded in accreted sediments at an evolved portion of the Nankai accretionary prism. *In* Mikada, H., Moore, G.F., Taira, A., Becker, K., Moore, J.C., and Klaus, A. (Eds.), *Proc. ODP, Sci. Results,* 190/196: College Station, TX (Ocean Drilling Program), 1–15. **doi:10.2973/odp.proc.sr.190196.202.2003**

Wang, K., and Hu, Y., 2006. Accretionary prisms in subduction earthquake cycles: the theory of dynamic Coulomb wedge. *J. Geophys. Res.,* 111(B6):B06410. **doi:10.1029/2005JB004094**

Publication: 11 March 2009
MS 314315316-114

Figure F1. Summary log diagram, Site C0002. Bedding and fracture dips from resistivity at bit image. LSF = LWD depth below seafloor, VE = vertical exaggeration, PEF = photoelectric factor. Black tadpoles = bedding, red tadpoles = fracture, tadpole line = dip direction of plane.

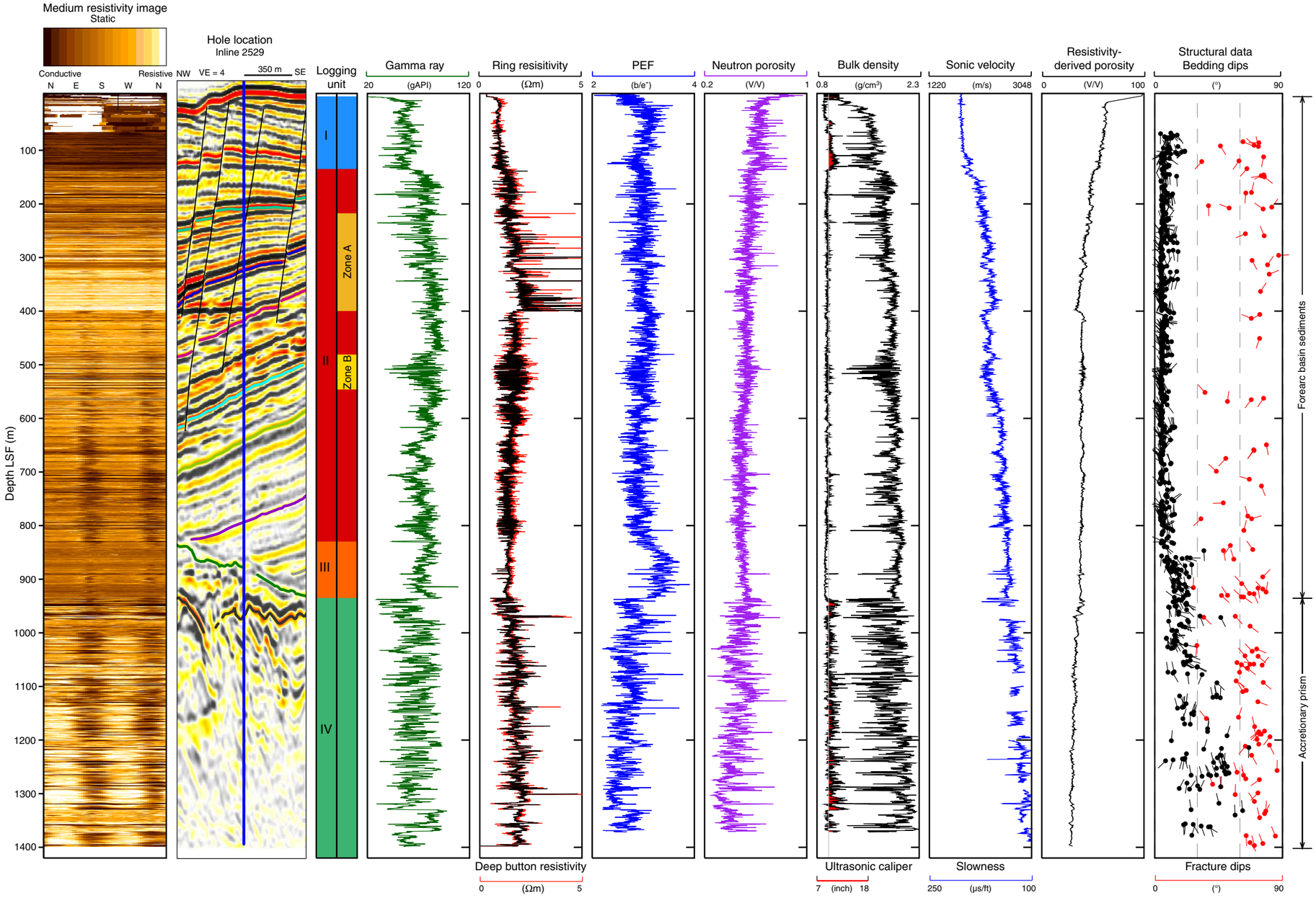

Figure F2. Three-dimensional seismic profile crossing Site C0002 (Moore et al., 2007). **A.** Inline 2529. BSR = bottom-simulating reflector. **B.** Cross-line 6225. VE = vertical exaggeration.

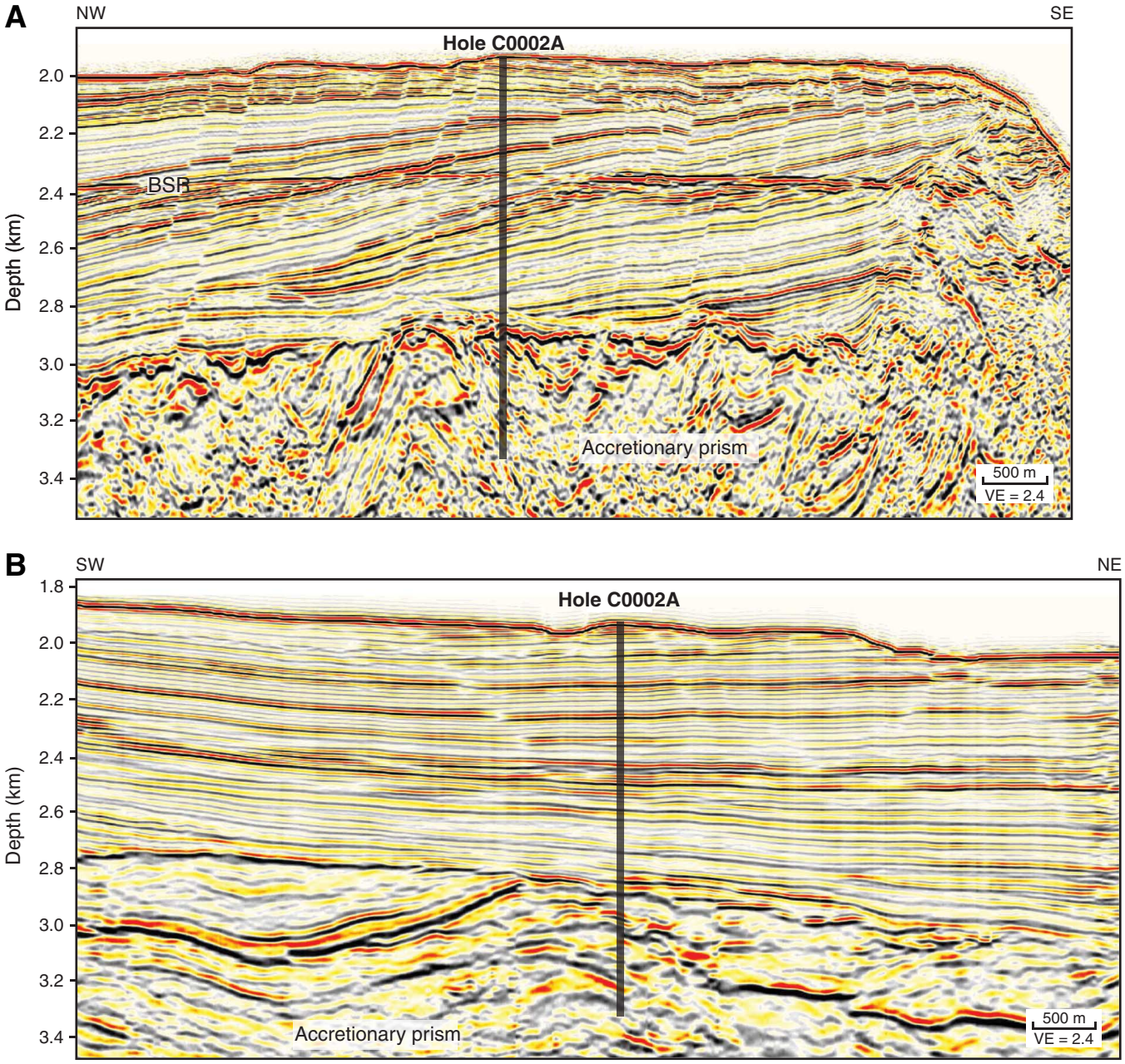

Figure F3. Drilling parameters and gamma ray log plotted vs. time for LWD-MWD-APWD operations in Hole C0002A. GR_RAB_RT = gamma ray resistivity-at-the-bit (real time), ECD = equivalent circulating density, APRS = average annular pressure, TRPM = MWD turbine rotation speed (off = <1500 or >4500 rpm, on = 1500–4500 rpm), TRPM_RT = TRPM (real time), CRPM = collar rotation, SWOB = surface weight on bit, HKLD = hook load, SPPA = standpipe pressure, ROP = rate of penetration, ROP_5ft = 5 ft averaged ROP, LSF = LWD depth below seafloor, DRF = drillers depth below rig floor.

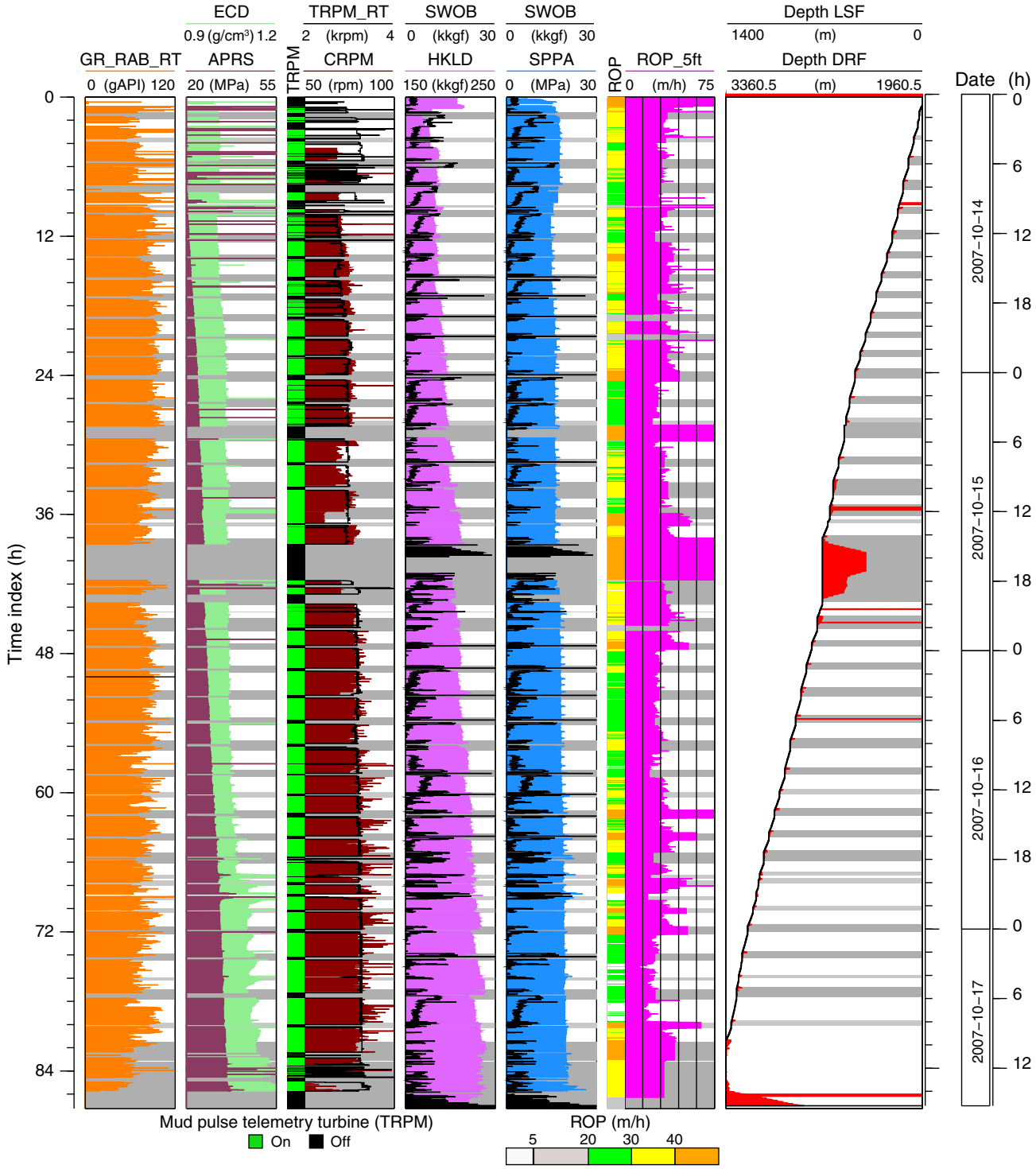

Figure F4. Mudline (seafloor) identification in Hole C0002A using natural gamma ray and resistivity logs of the geoVISION resistivity tool (memory data). The seafloor is defined by a break in the natural gamma ray and resistivity logs at 1964.5 m drillers depth below rig floor (DRF). Resistivity data are plotted on a linear scale.

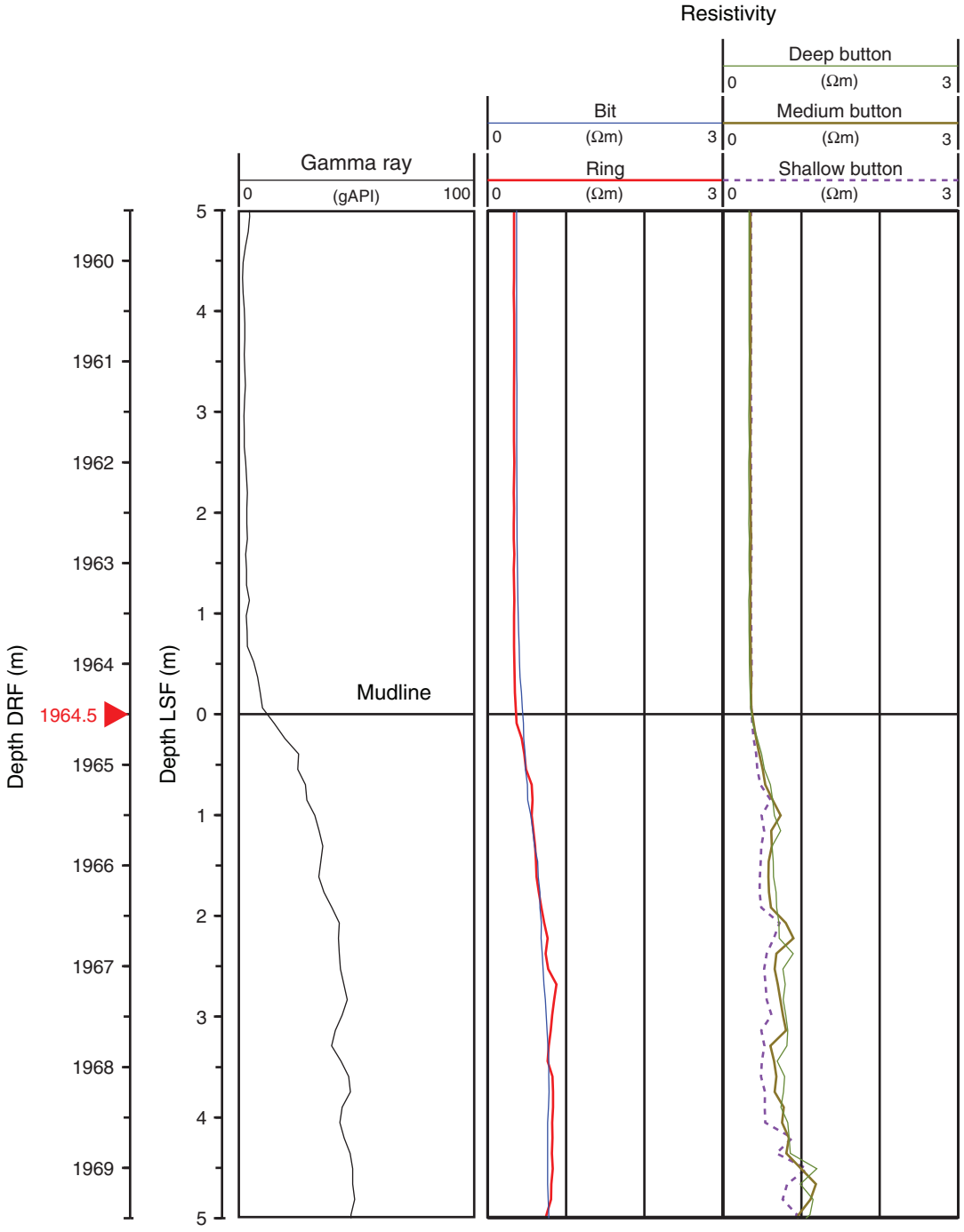

Figure F5. Control logs of Hole C0002A. LSF = LWD depth below seafloor; ROP = rate of penetration; SWOB = surface weight on bit; CRPM = drilling collar (bit) rotation; HKLD = hookload; SPPA = standpipe pressure; ECD = equivalent circulating density; CC15, CC26, CC37 and CC48 = ADN tool ultrasonic calipers; SKR_T and SHK_R = transverse and radial shocks experienced by the geoVISION resistivity tool; SHKPK = shock peak; STICK = stick-slip indicator.

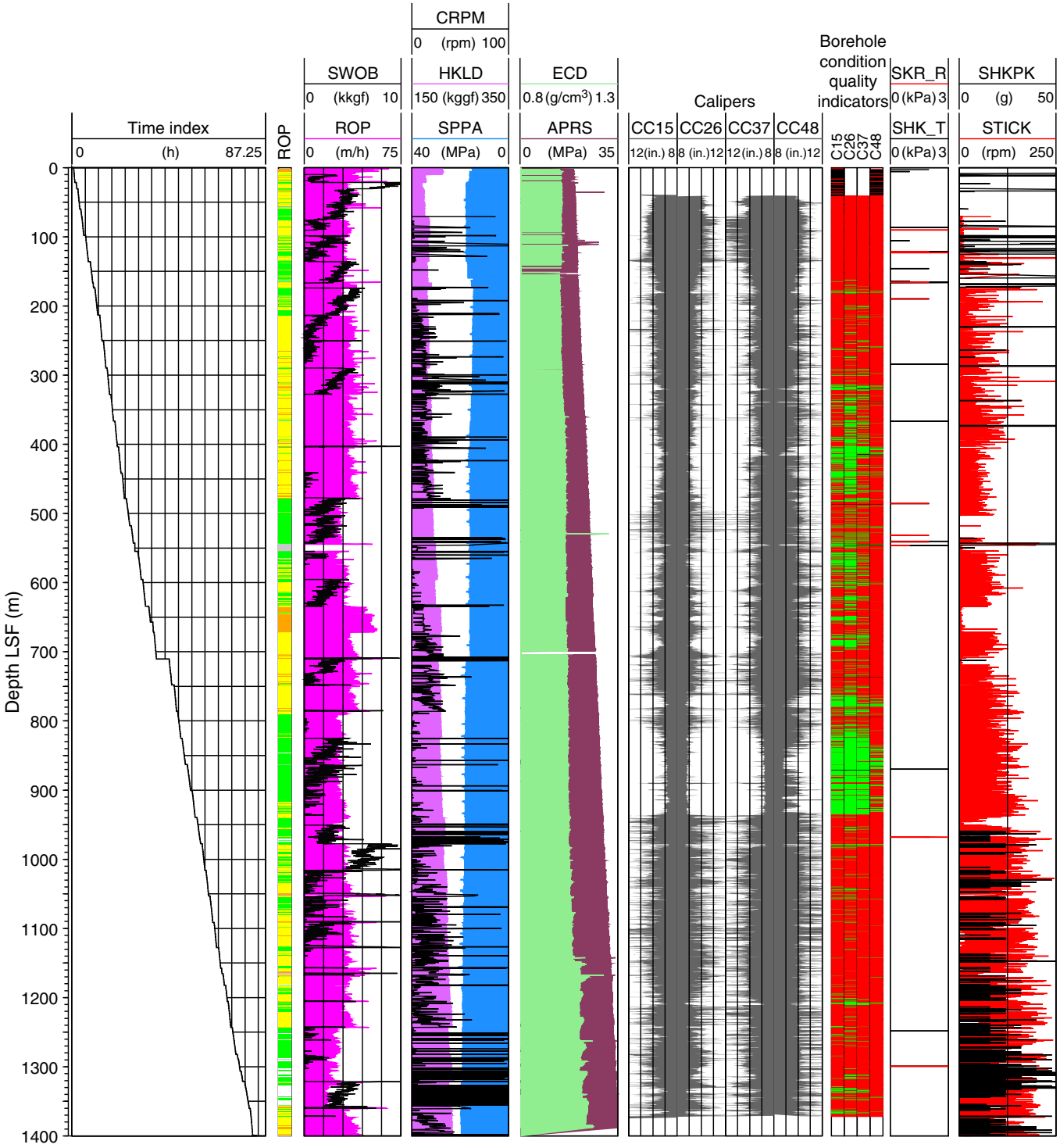

Figure F6. Geophysical logs in Hole C0002A. LSF = LWD depth below seafloor, ROP = rate of penetration; TAB_RAB_GR = time after bit (TAB) of gamma ray measurement by the geoVISION resistivity (GVR) tool, GR_RAB = gamma ray log (GVR memory data), Cxy = ADN ultrasonic calipers (C15, C26, C37, and C48), TAB_DEN = TAB of ADN density measurement, IDRO = image-derived density, IDDR image-derived density correction (for stand-off), TAB_RAB_BD = TAB of GVR deep button resistivity, TAB_RAB_BIT = TAB of GVR bit resistivity, RES_BD = deep button resistivity, RES_BM = medium button resistivity, RES_BS = shallow button resistivity, V_P = sonic compressional velocity, DTCO = Δt compressional transit time measurement, sonic processing and quality color-coded indicators and geoVISION resistivity image quality. (**Figure shown on next page.**)

Figure F6 (continued). (Caption shown on previous page.)

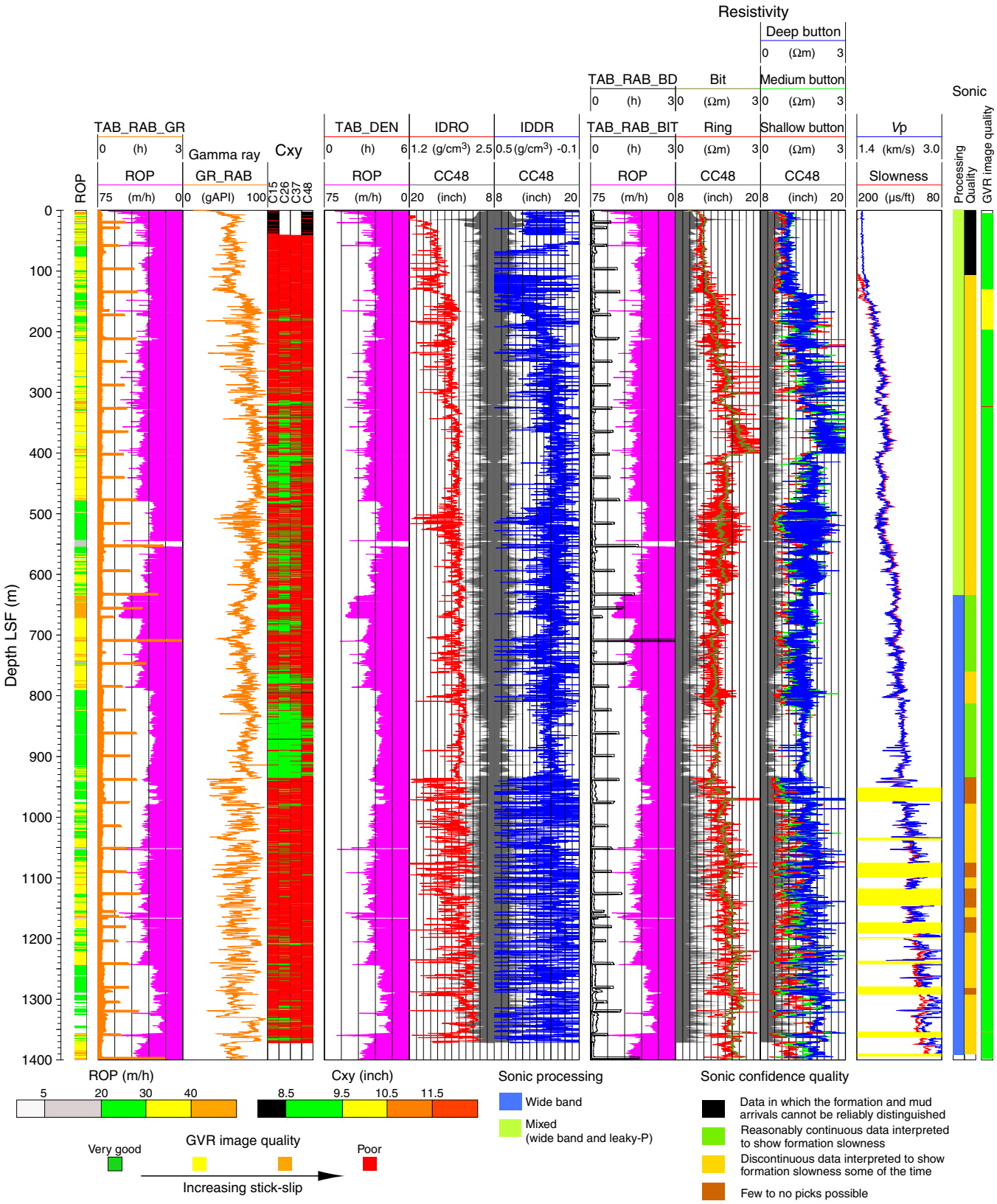

Figure F7. Plot of time-depth relationship in Hole C0002A. LSF = LWD depth below seafloor.

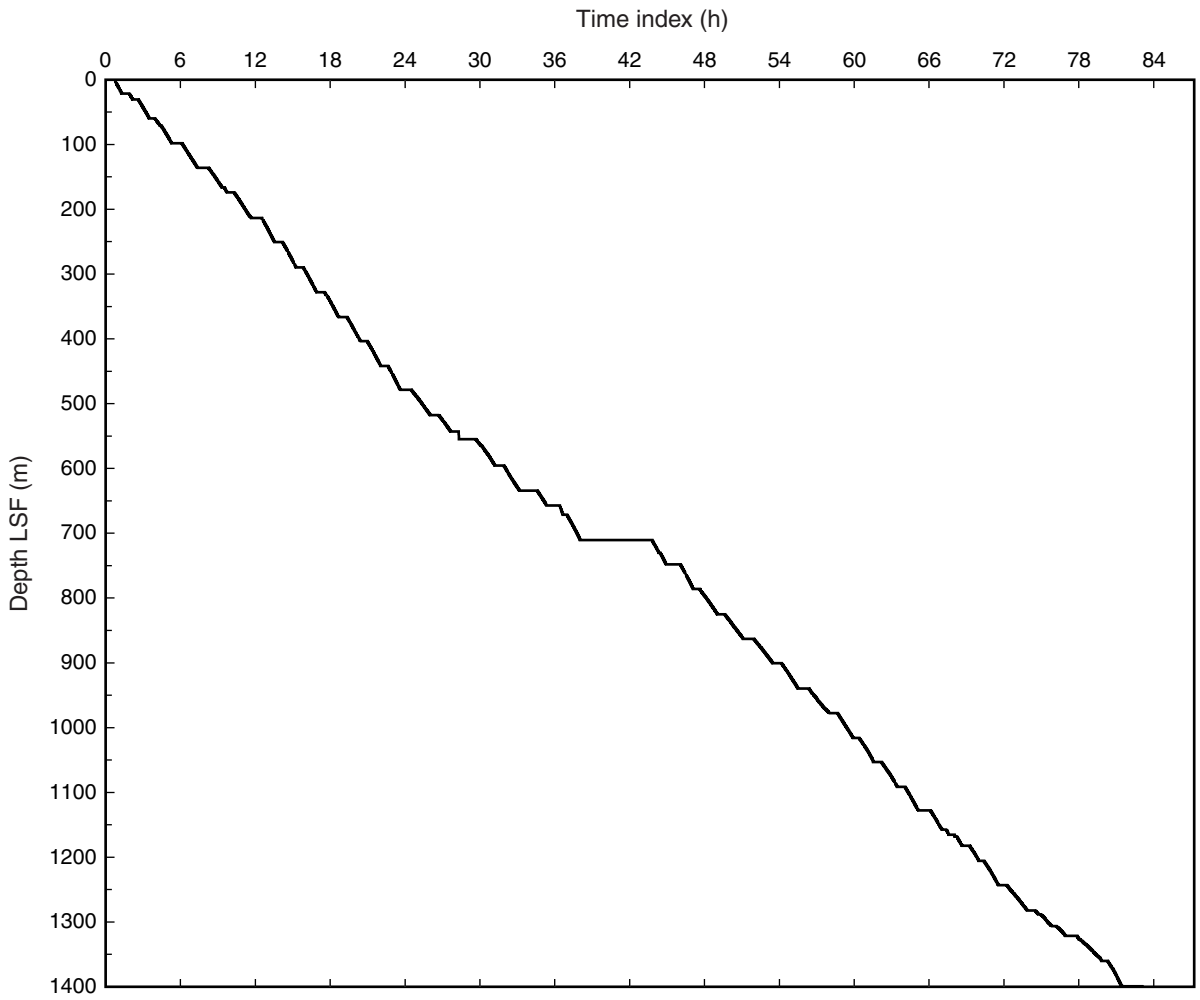

Figure F8. Example of wide quality control log prepared for the sonic log from the sonicVISION tool. Color panels are slowness coherence plots for the common source (left) and common receiver (middle) configurations of the tool. Horizontal axis is slowness, with higher slowness (lower velocity) to the right. Warm colors = high signal strength at a particular slowness. Black vertical lines = manual picks. Gray-scale plot shows seismograms with time increasing to the right. Blue line = arrival pick associated with slowness identified in the picks. Final slowness value at depth is given by the mean of the slownesses picked in the common source and common receiver configurations. This serves to compensate for tool position in the hole. This plot illustrates an interval in which few if any reliable velocity picks are possible. LSF = LWD depth below seafloor.

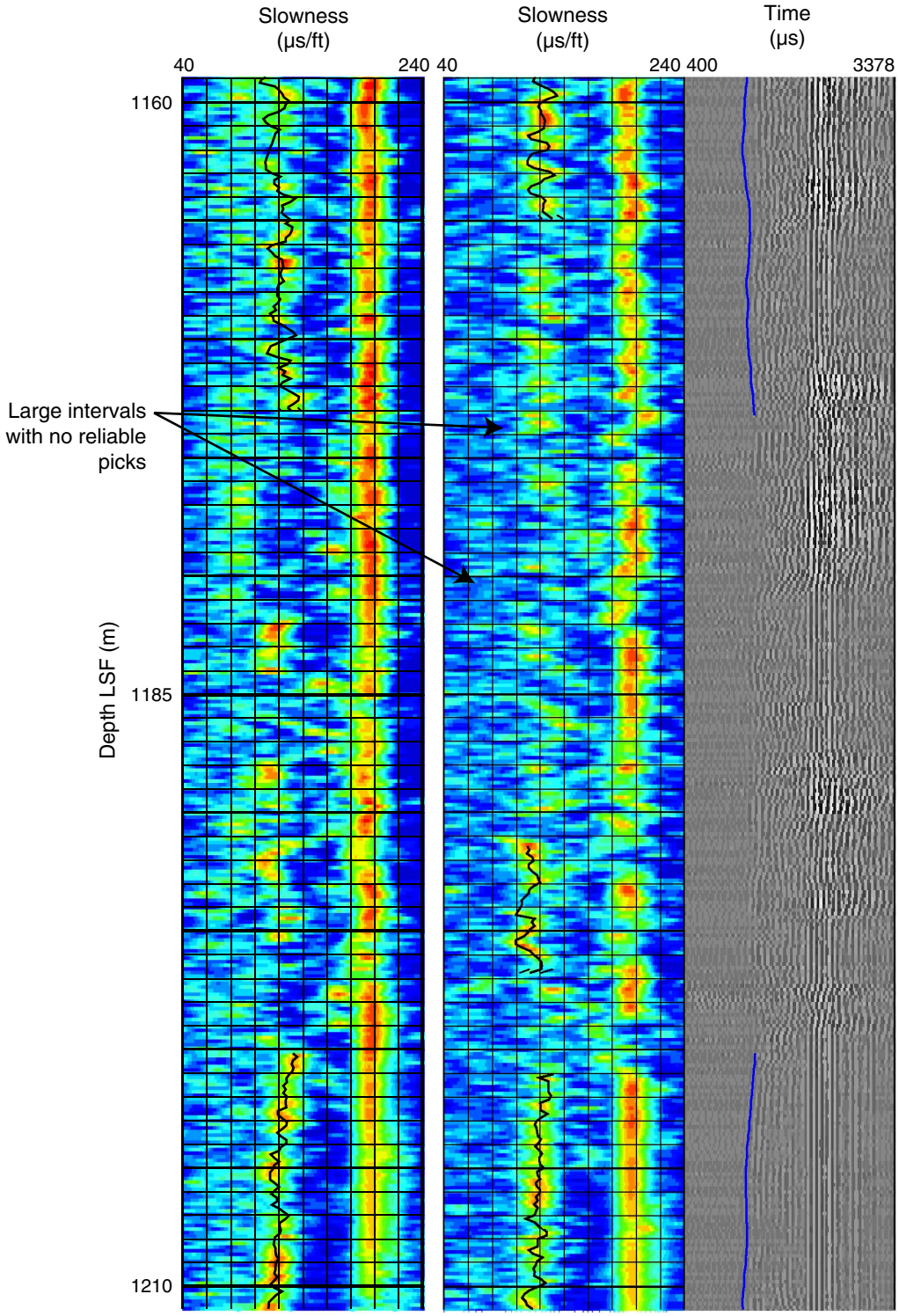

Figure F9. Statistical variation exhibited by the main logging units and zones. PEF = photoelectric factor.

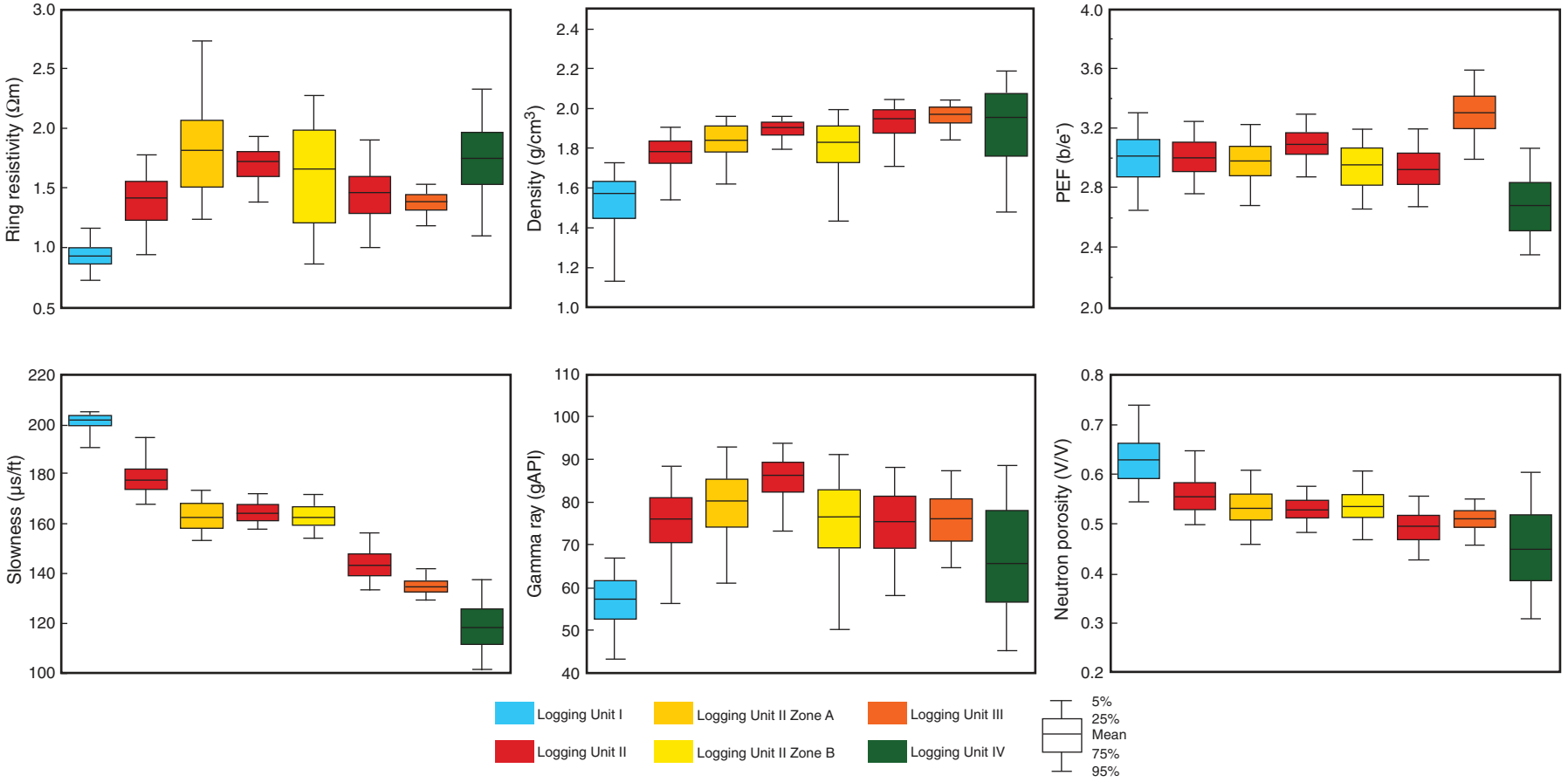

Figure F10. Caliper log (CCAV) (red = caliper values >9.5 inches); smoothed ring and bit resistivity logs; smoothed shallow, medium, and deep button resistivity log; and smoothed resulting curve of the difference between deep and shallow resistivity button data. Smoothing results from a moving average of the resistivity values using a 21-point (~3 m) window. LSF = LWD depth below seafloor.

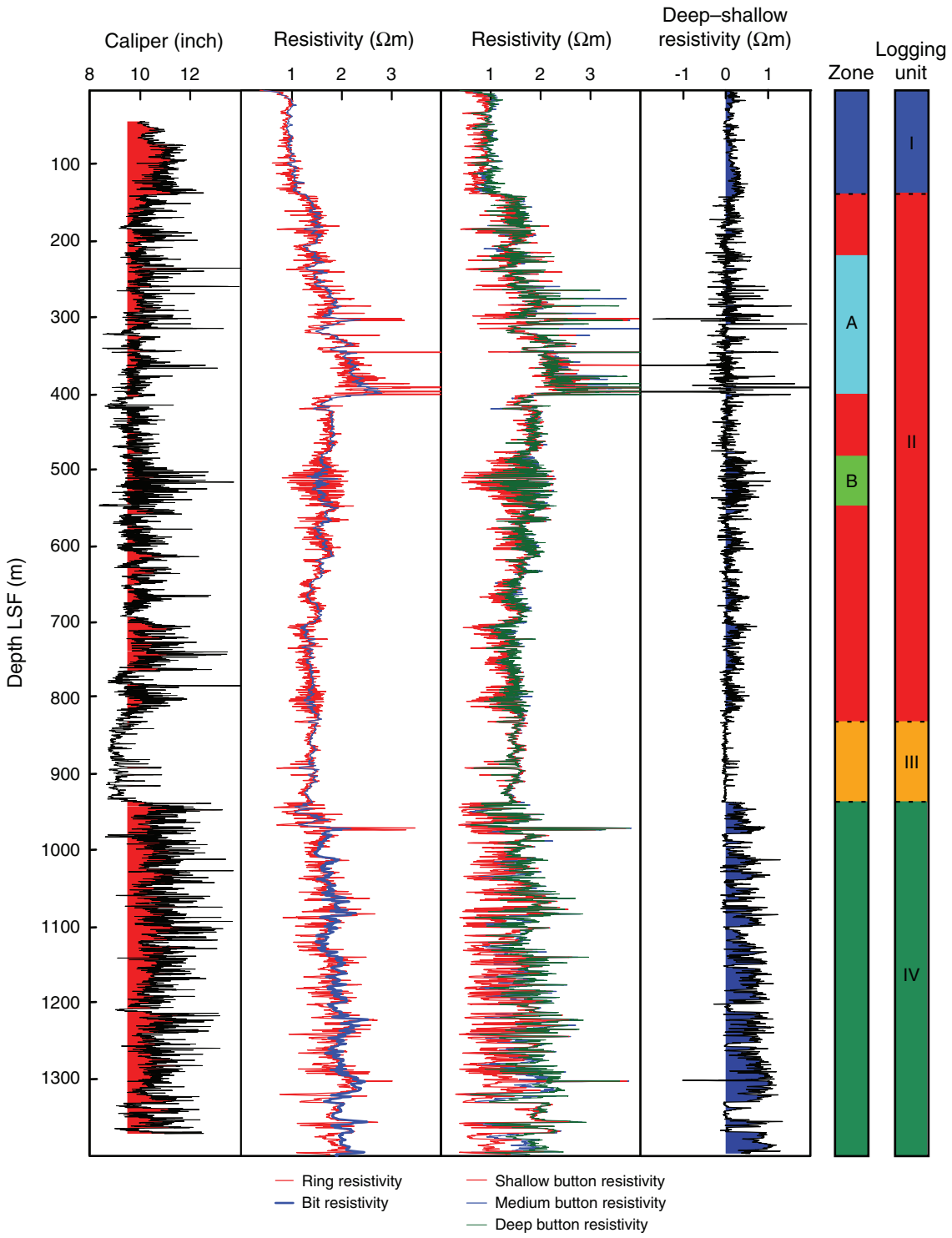

Figure F11. Summary of variation in bedding dips between the logging units and zones. Green boxes = intervals shown in Figure F12. PEF = photoelectric factor, GR = gamma ray, LSF = LWD depth below seafloor.

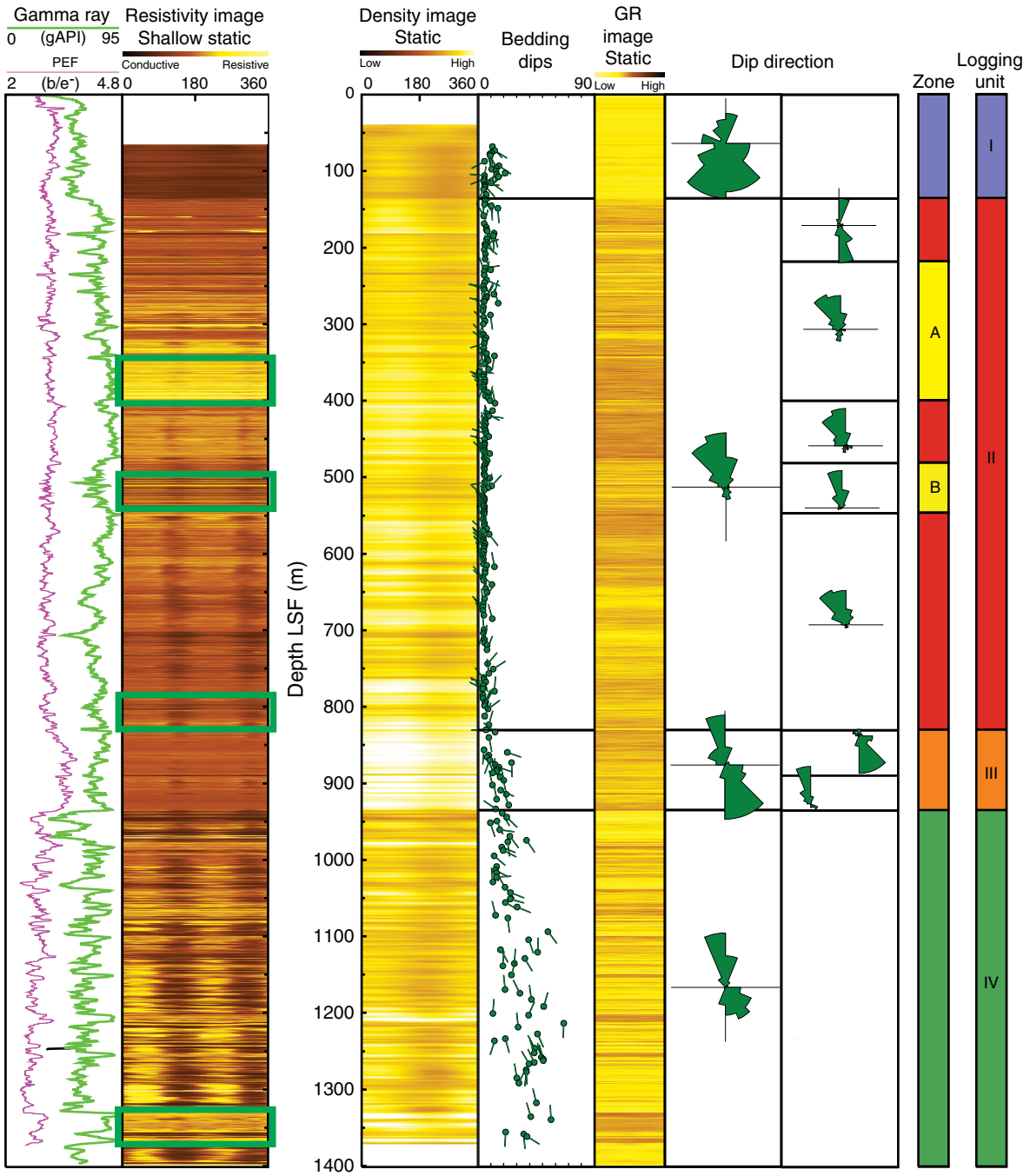

Figure F12. A. Representative images of facies variability corresponding to boxed intervals in Figure F11. Typical resistivity image of logging Unit II Zone B. Layered sediments are identified as alternating resistive and conductive layers in the image. A thickening upward trend is displayed within this section. Light bands are also observed on the density image and the natural gamma ray (GR) image. Higher frequency excursions are indicative of thinner layers toward the bottom. Dip measurements indicate generally north-northwest to northwest bedding dips. LSF = LWD depth below seafloor, PEF = photoelectric factor. (Continued on next page.)

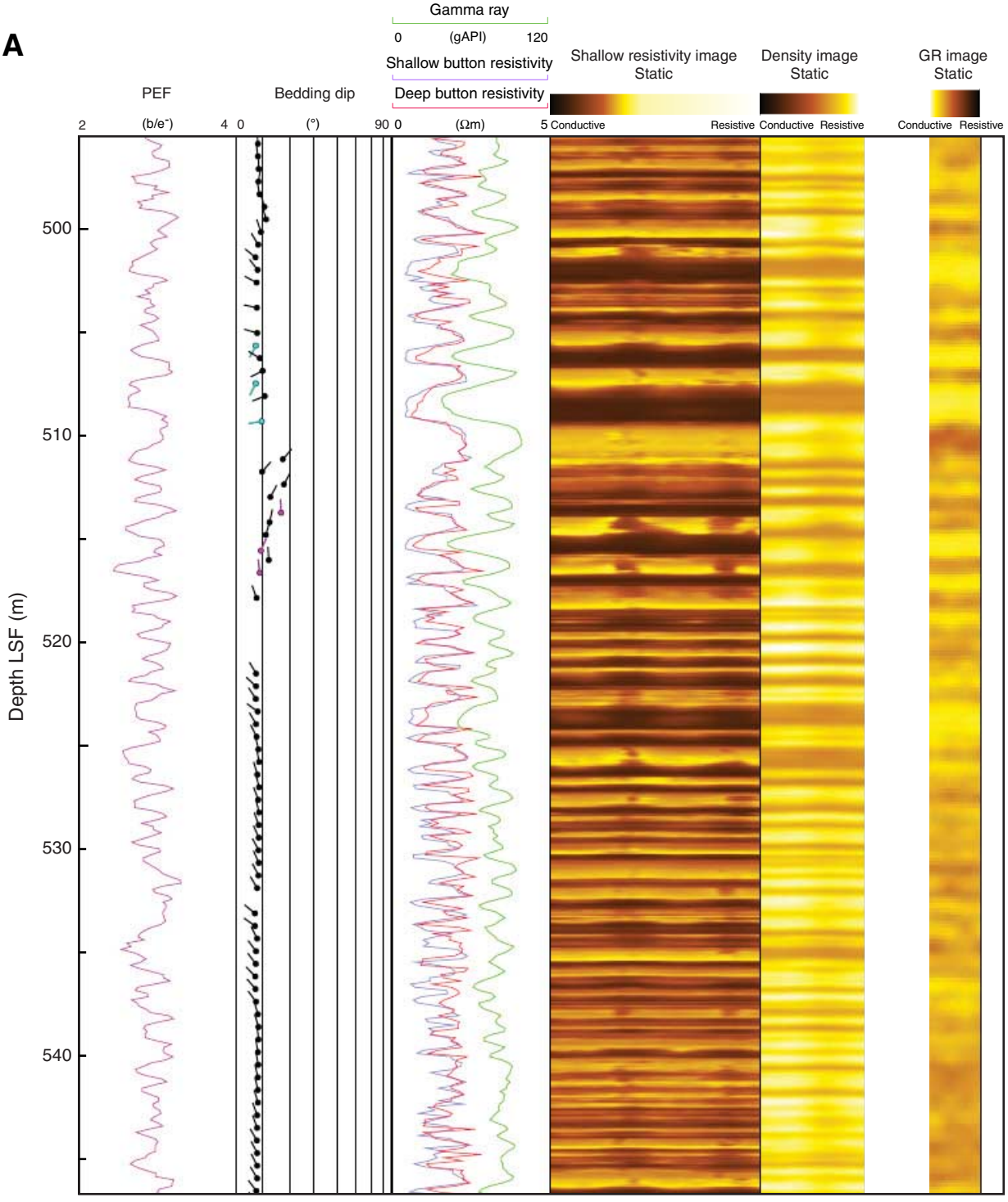

Figure F12 (continued). B. Resistivity images from the basal part of logging Unit II showing high-frequency alternating cycles composed of resistive and conductive layers. Notice a predominance of darker colors indicating lower resistivity than in Zone B. Dip measurements indicate north-northwest to northwest bedding dips. LSF = LWD depth below seafloor, PEF = photoelectric factor GR = natural gamma ray.

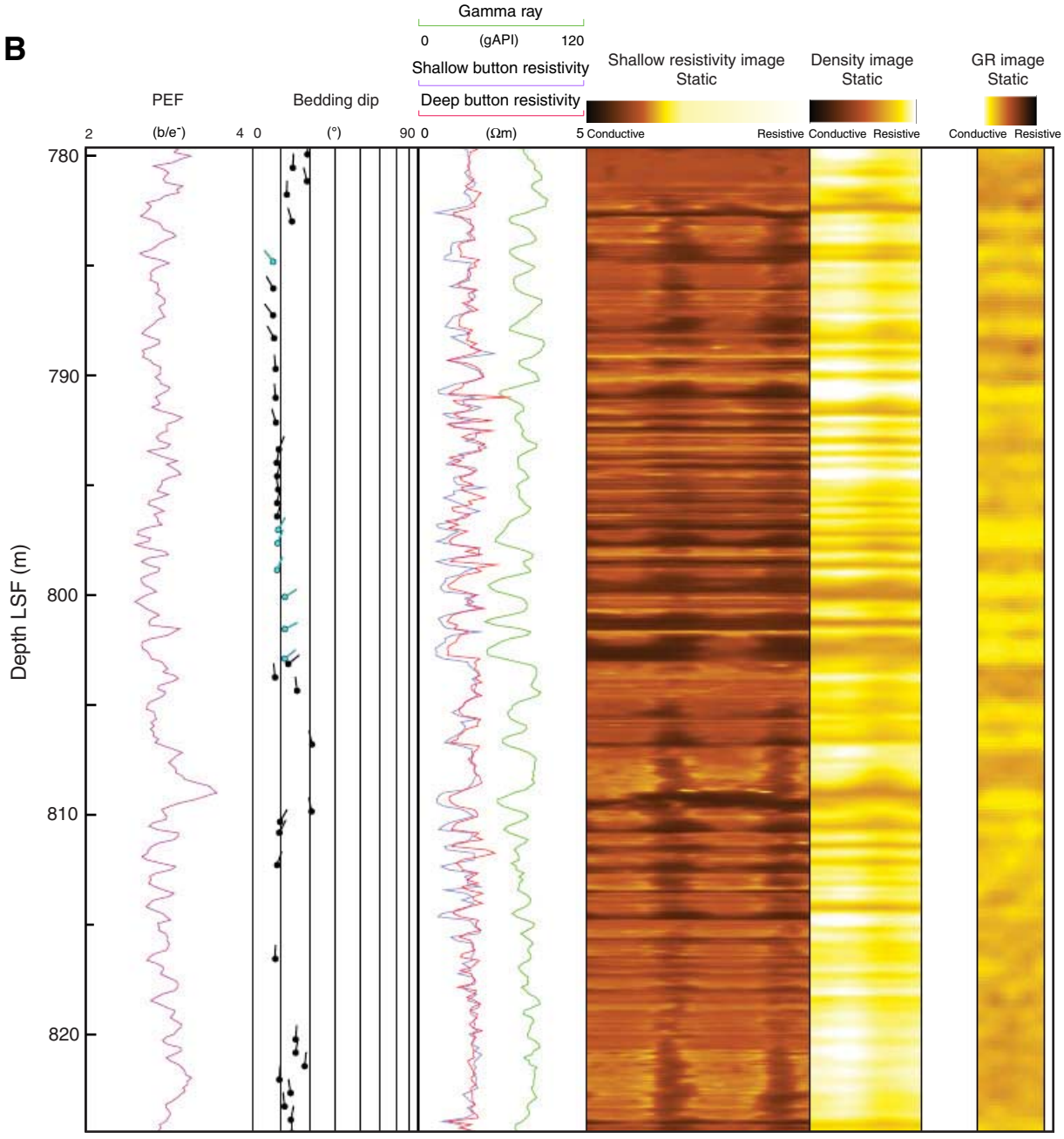

Figure F13. A. Ring resistivity, gamma ray, sonic velocity, and ultrasonic caliper logs and a resistivity-at-the-bit (RAB) deep image in the interval 371–401 m LSF, the lowermost part of Zone A. Arrows indicate that all resistive peaks (colored zones) are correlated to lower gamma ray and higher velocity peaks and intervals of larger borehole diameter. Dip measurements indicate north-northwest to northwest bedding dips. (**Continued on next page.**)

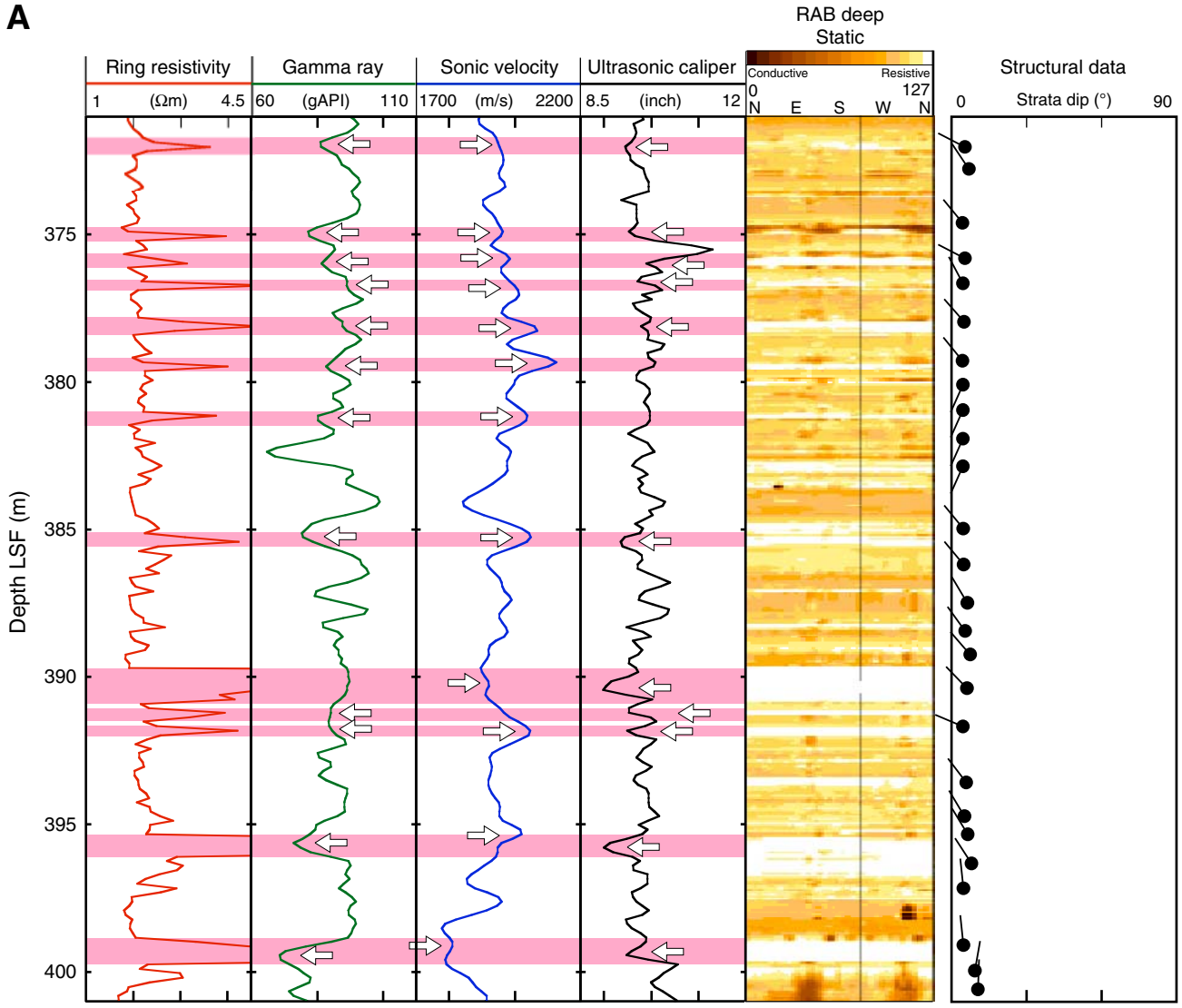

Figure F13 (continued). B. Ring resistivity, gamma ray, sonic velocity, and ultrasonic caliper logs and resistivity-at-the-bit (RAB) deep image in the central part of Zone B (495–525 m LSF). Arrows indicate that conductive layers (colored zones) are correlated to lower gamma ray and lower velocity peaks and intervals of smaller borehole diameter. Sharp lower boundaries and gradational tops are observed in each conductive layer from the ring resistivity log and RAB image.

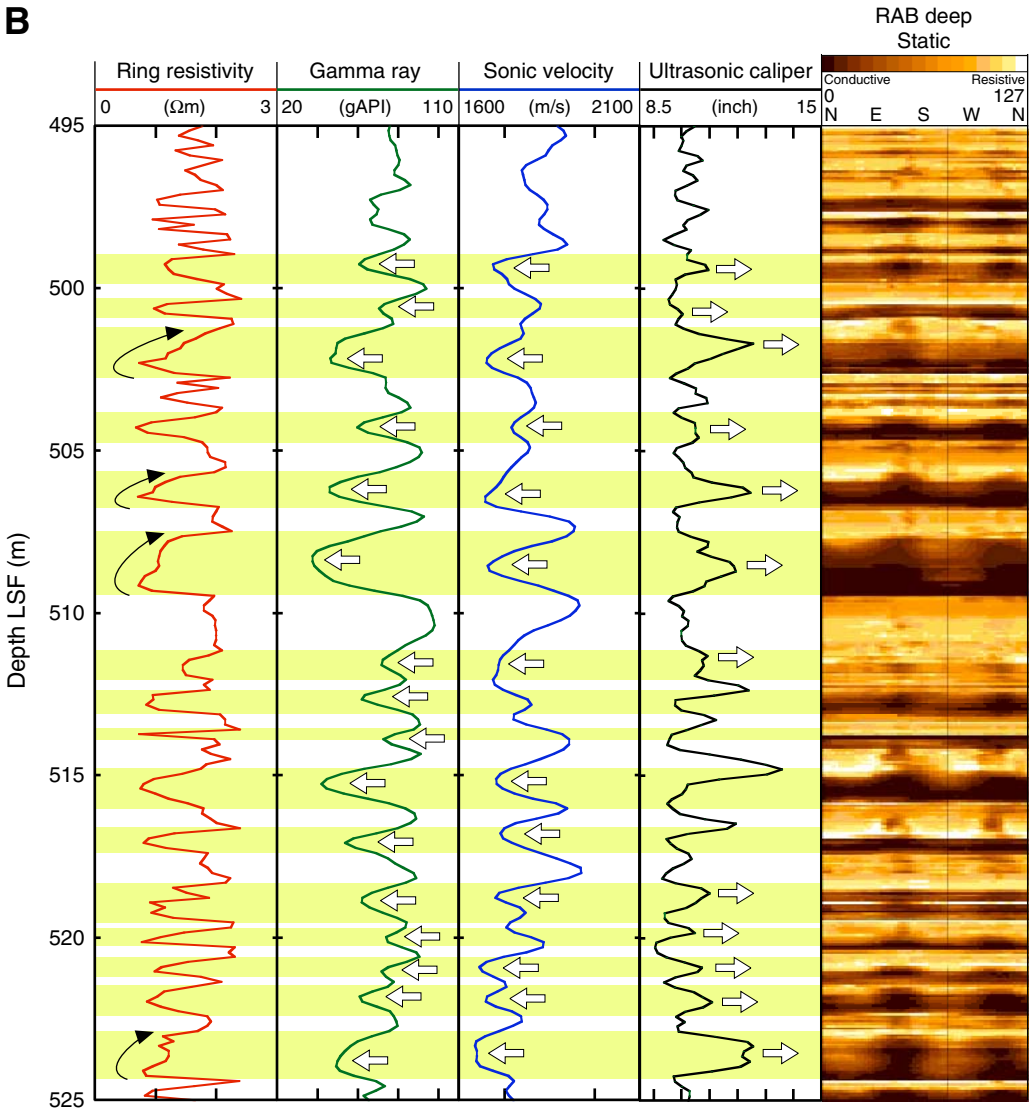

Figure F14. Logging Units I–IV and Zones A and B superimposed on check shot–corrected prestack depth-migrated seismic profile through Hole C0002A. Seismic Units Kumano 2–12, Lower Sediments, and Accretionary Prism from Gulick et al. (2007). LSF = LWD depth below seafloor, VE = vertical exaggeration.

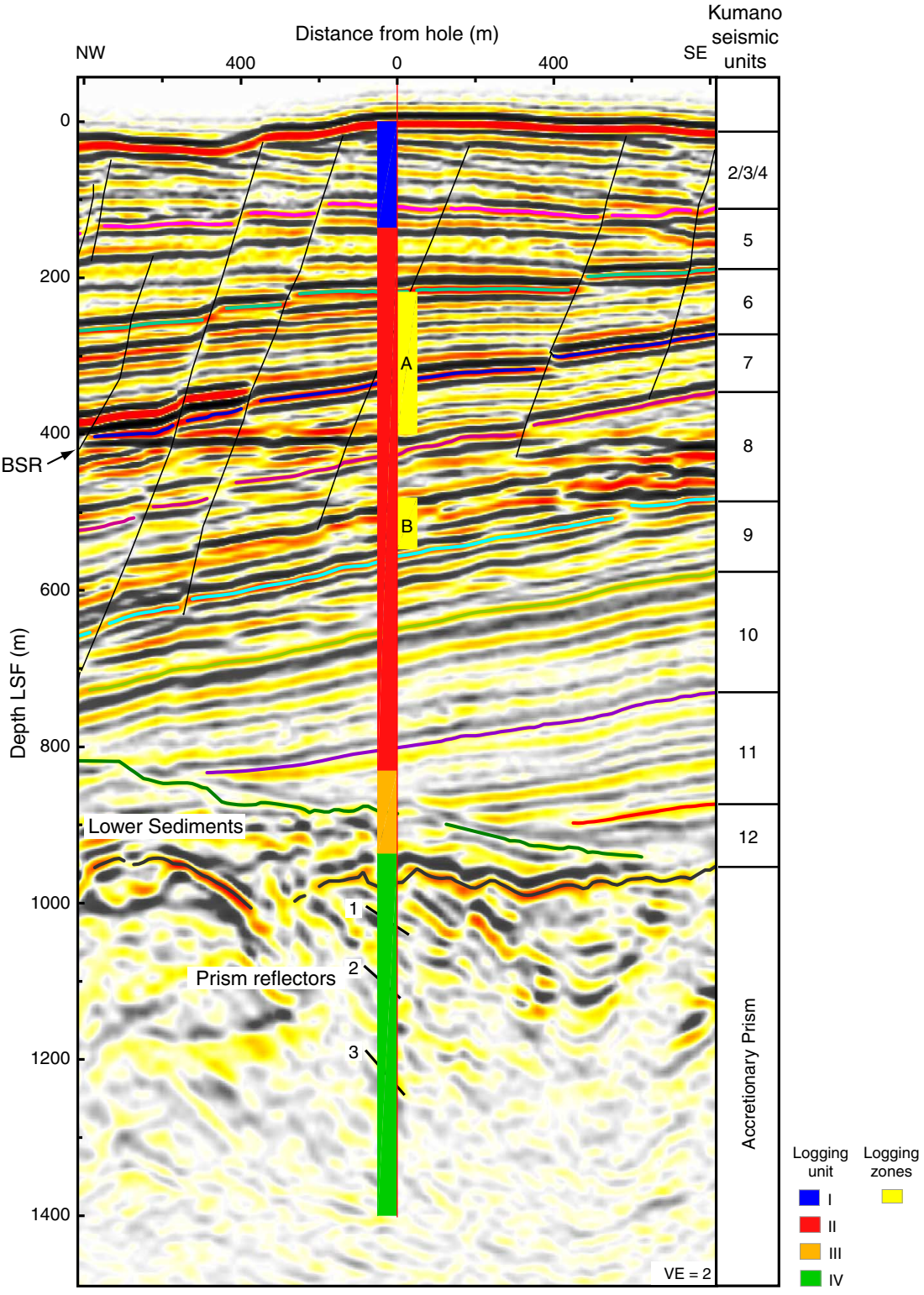

Figure F15. Display of log responses through logging Unit III. Dashed line = unconformity characterized by a variation in bedding dips (Fig. F11) above and below a prominent negative peak seen in all the logs. LSF = LWD depth below seafloor, PEF = photoelectric factor.

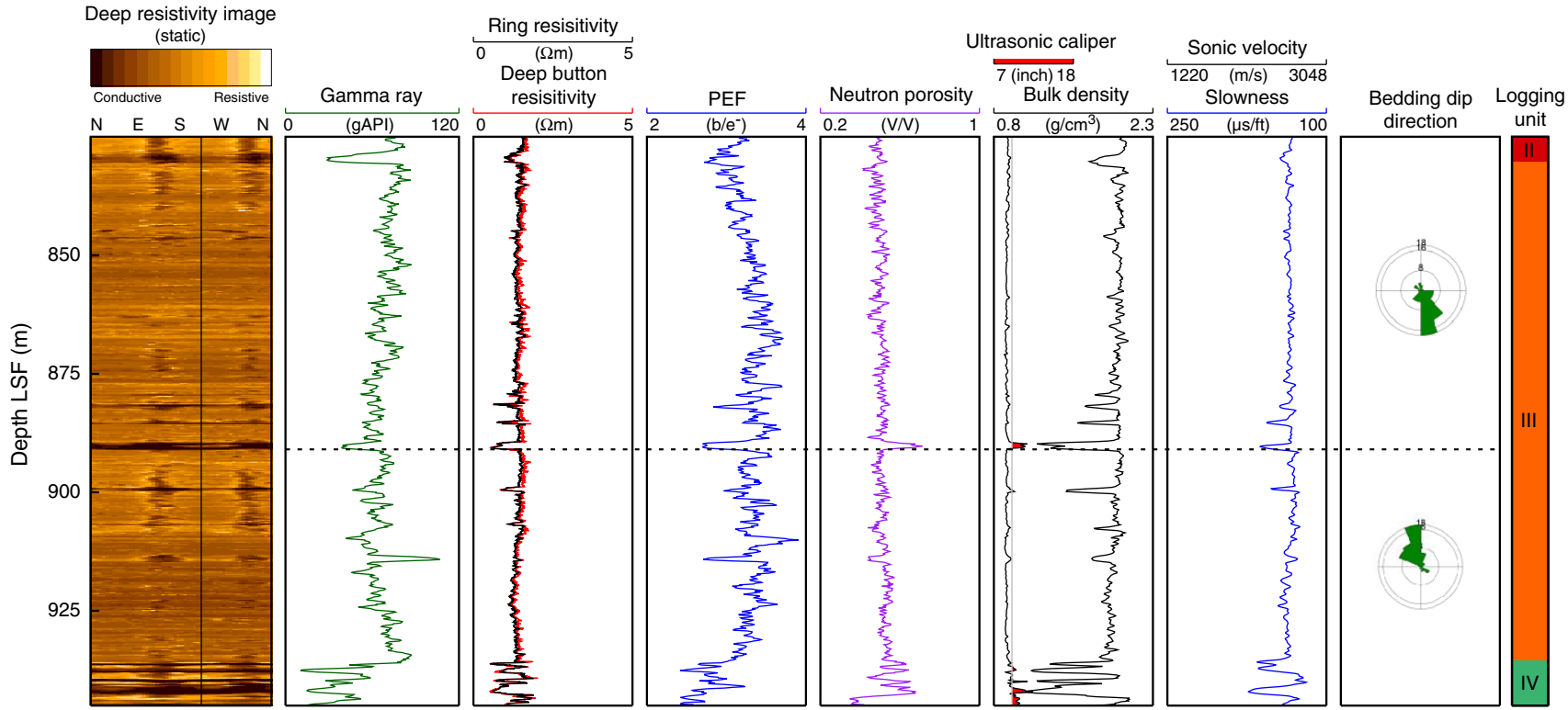

Figure F16. Thickest example of the "mottled" intervals present within logging Unit IV. LSF = LWD depth below seafloor, PEF = photoelectric factor.

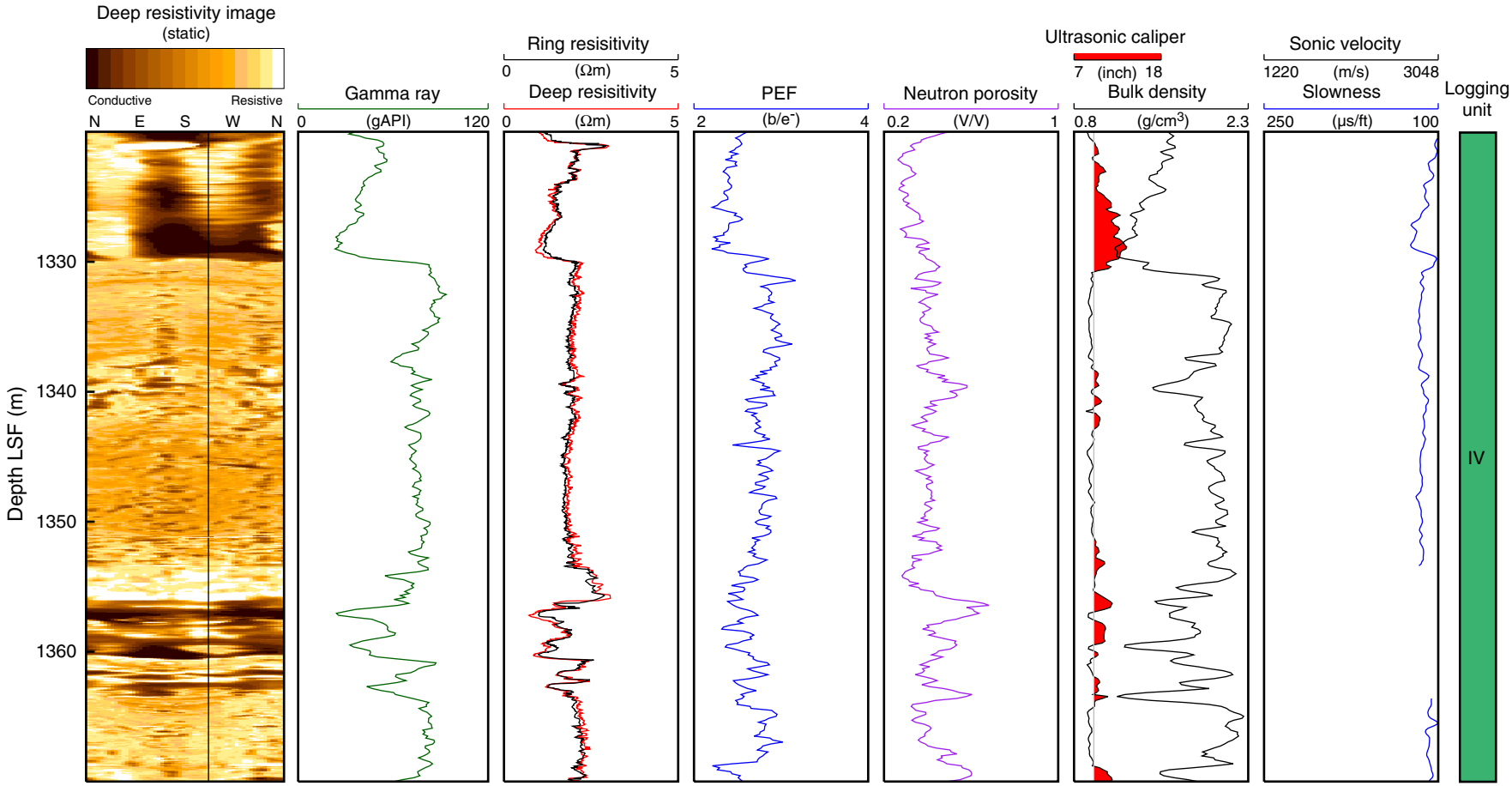

Figure F17. Image-derived density data (IDRO) profile from Hole C0002A. LSF = LWD depth below seafloor.

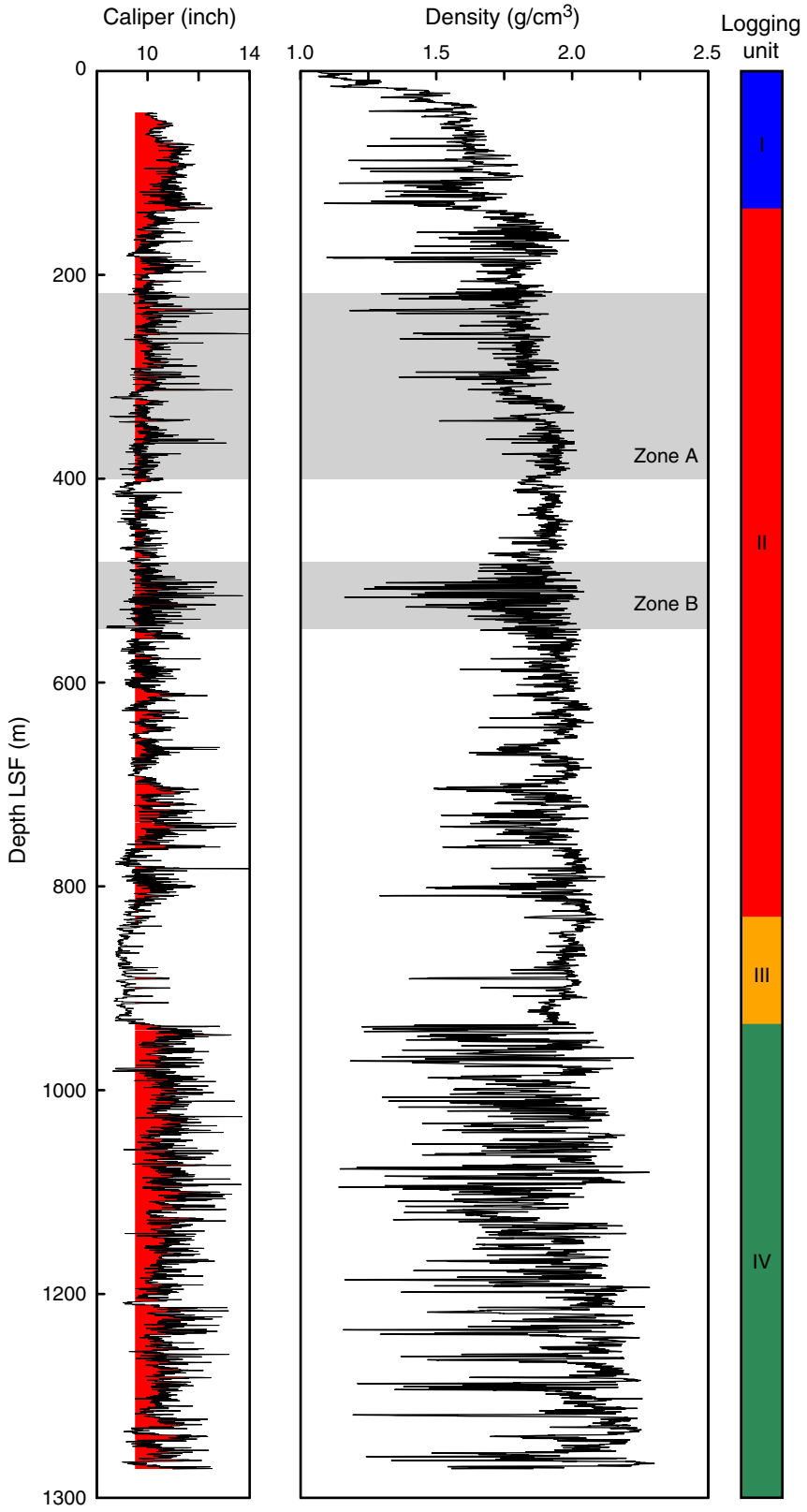

Figure F18. Neutron (TNPH) and density (IDRO)-derived porosity profiles from Hole C0002A. LSF = LWD depth below seafloor.

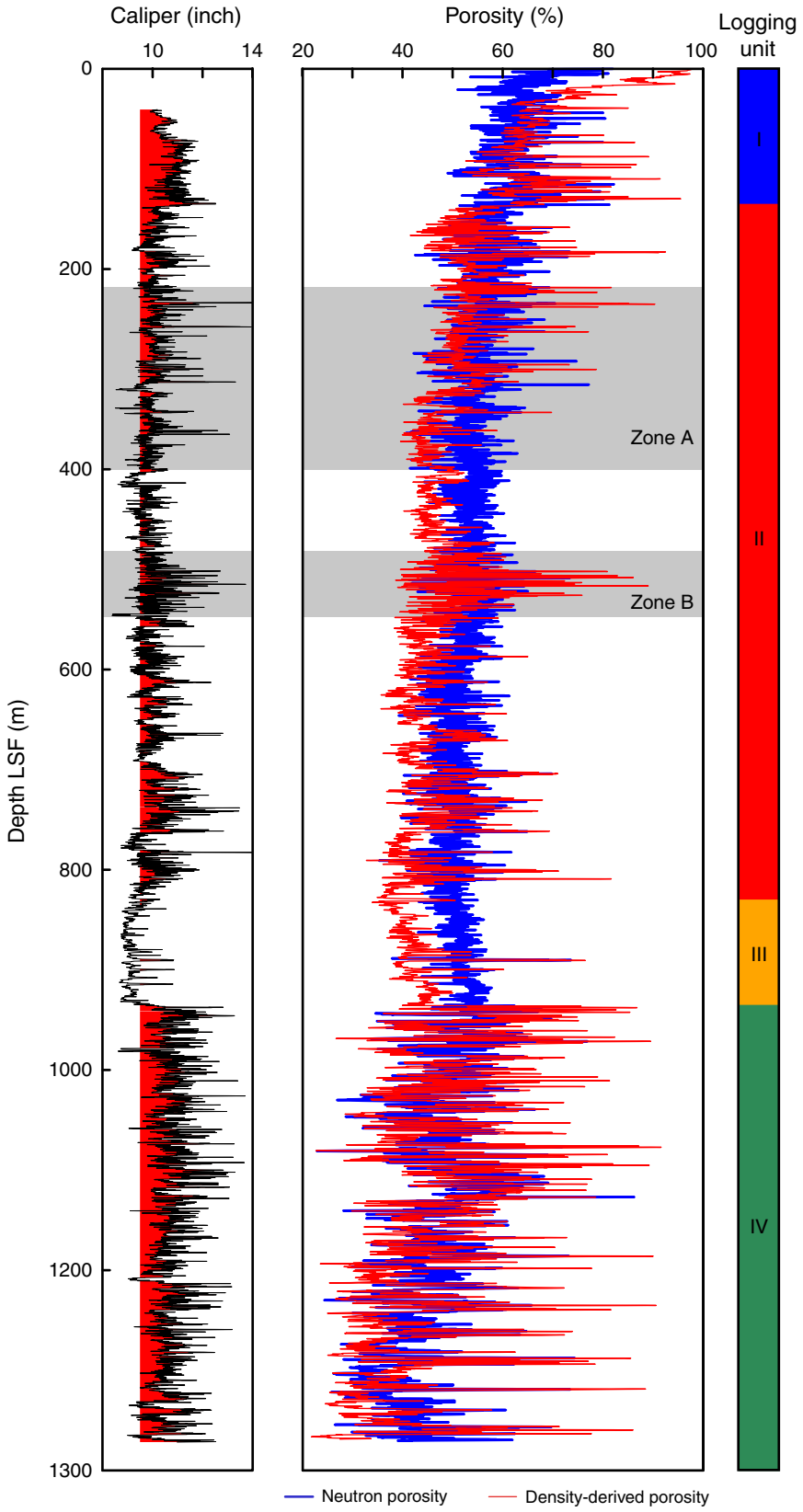

Figure F19. Plot of neutron porosity vs. density (IDRO)-derived porosity. Solid line = unit slope passing through the origin.

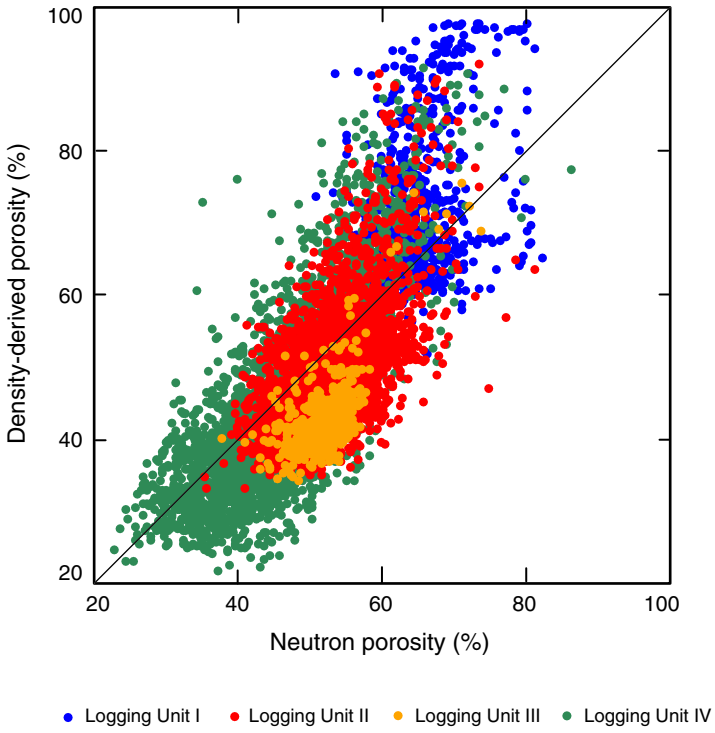

Figure F20. Neutron porosity (TNPH) data profile from Hole C0002A and smoothed porosity data using a 4.5 m running average. LSF = LWD depth below seafloor.

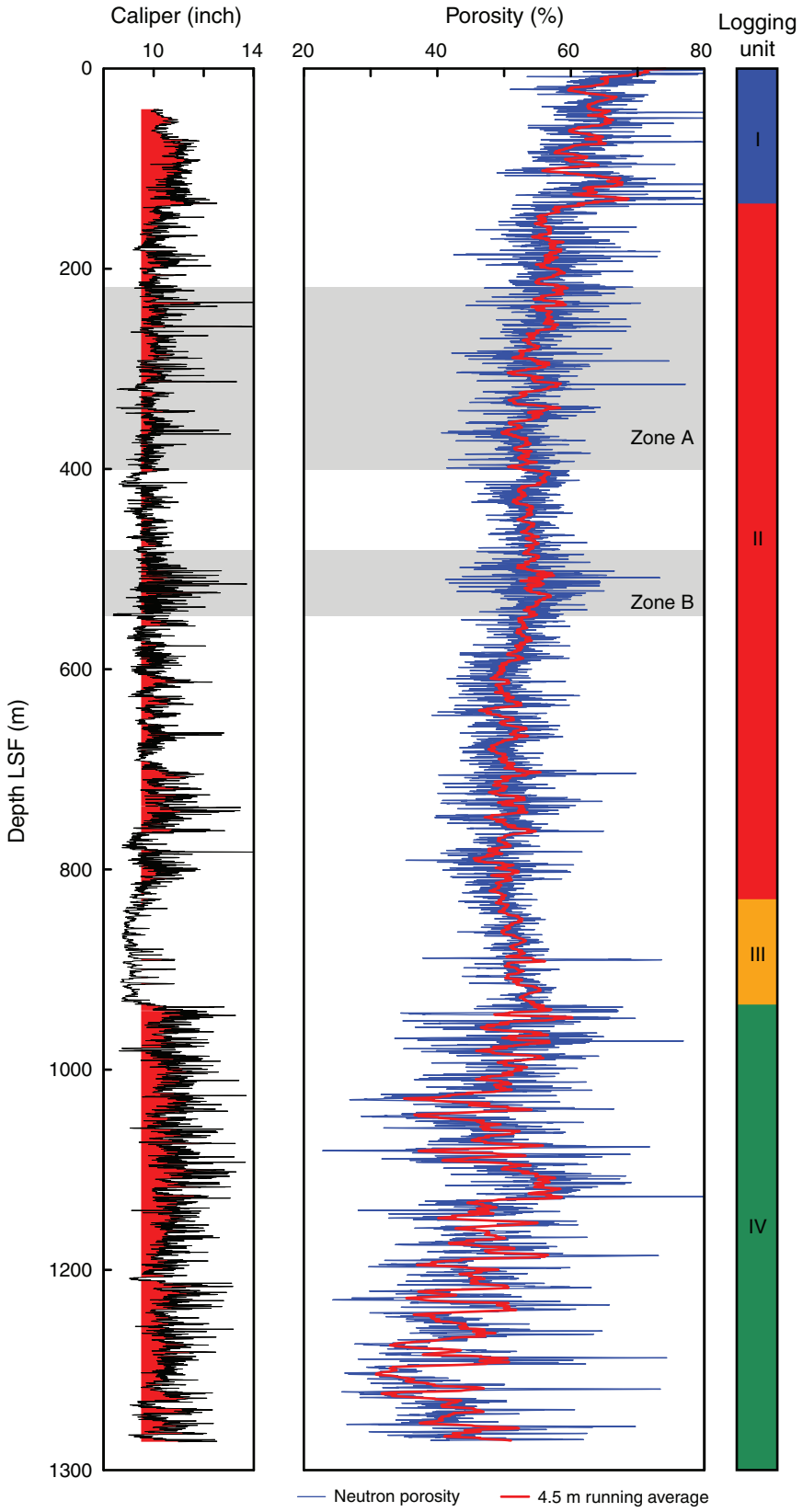

Figure F21. Plots of (**A**) bit vs. ring resistivity and (**B**) deep vs. shallow resistivity.

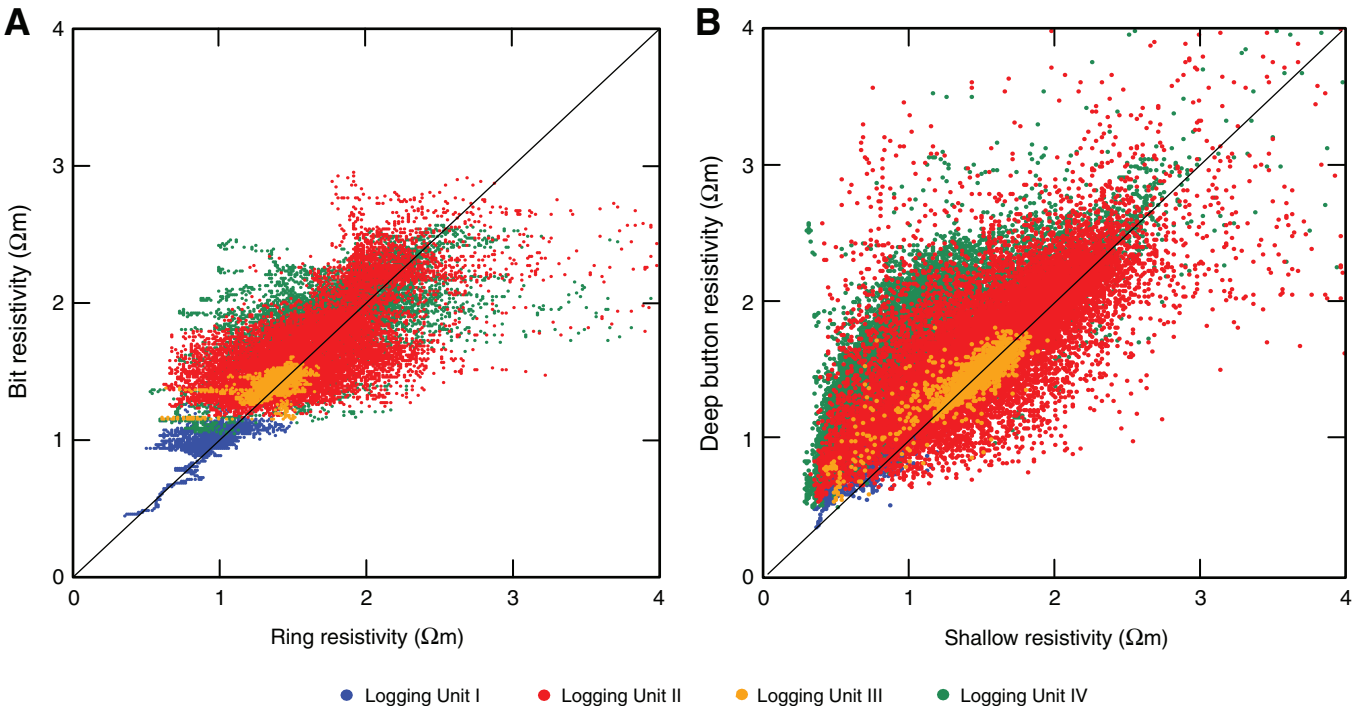

Figure F22. Plots of ring and bit formation factor (FF) vs. bulk density (IDRO)–derived porosity. Curved lines correspond to the plot of the Archie's law, FF = $1/\phi^{-2.4}$.

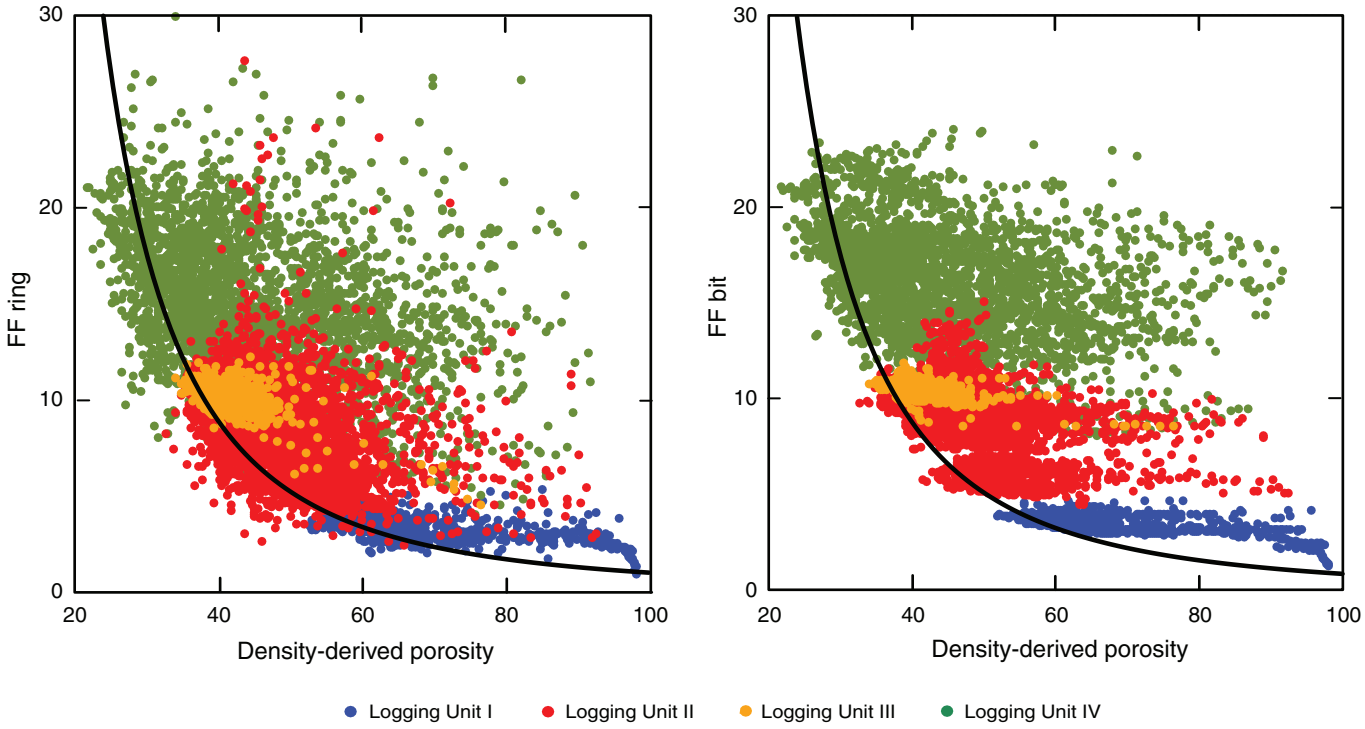

Figure F23. Bit resistivity porosity derived from Archie's law with parameters a = 1 and m = 2.4 compared with neutron porosity (TNPH) and bulk density (IDRO)–derived porosity. LSF = LWD depth below seafloor.

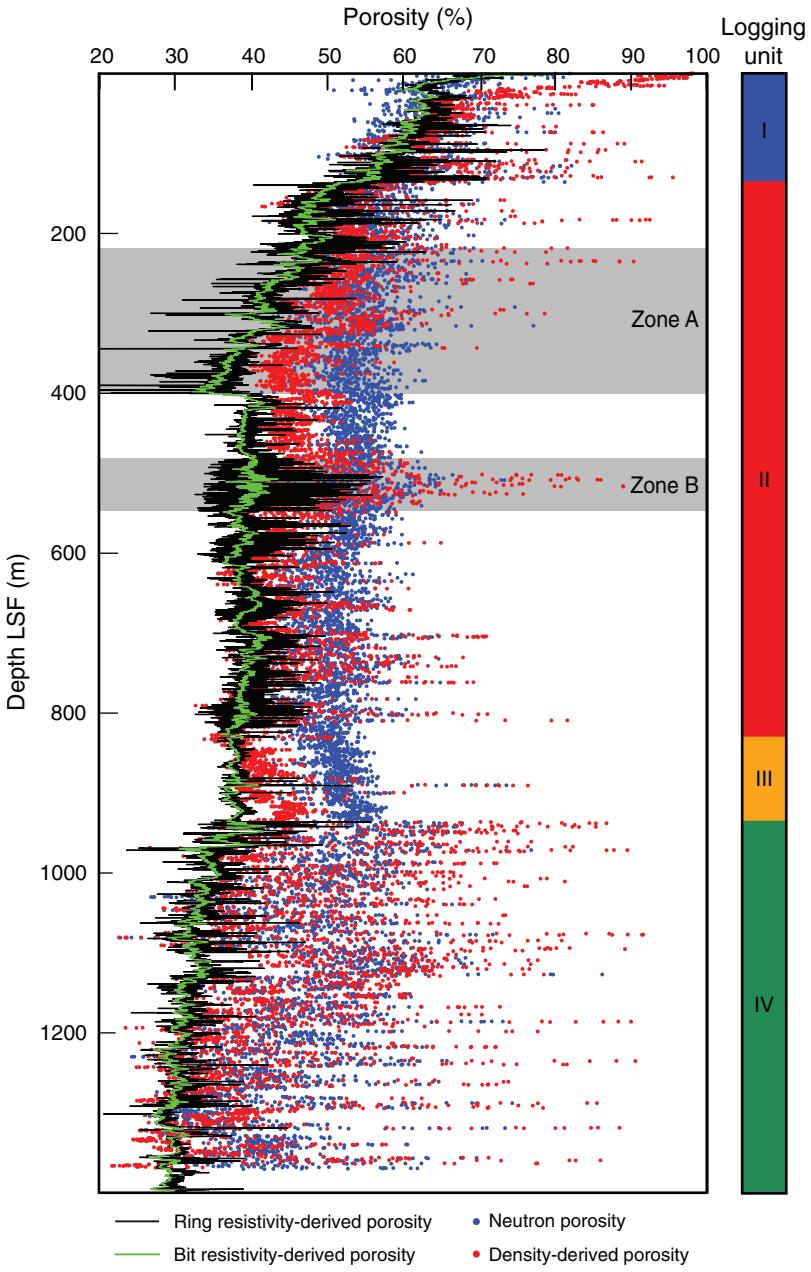

Figure F24. Plots of ring and bit resistivity porosity vs. bulk density (IDRO)–derived porosity. Solid line = unit slope passing through the origin.

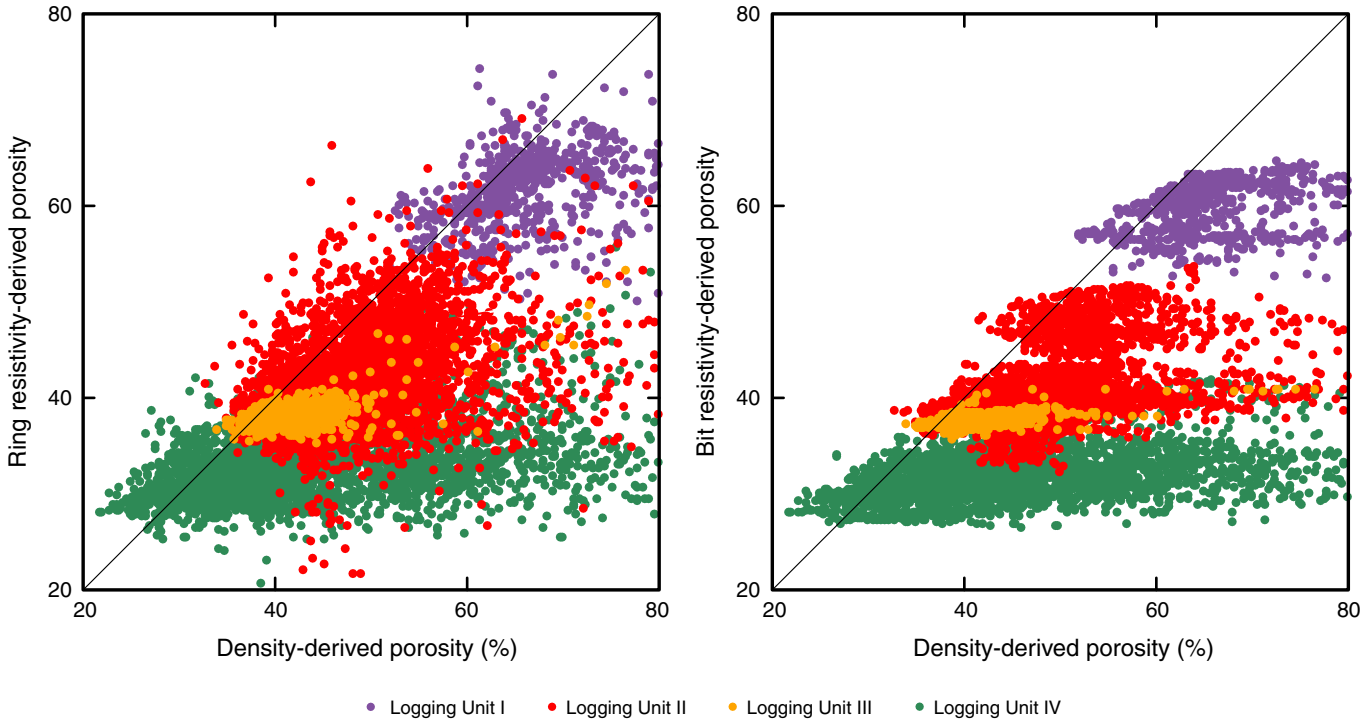

Figure F25. *P*-wave velocity log in Hole C0002A. LSF = LWD depth below seafloor.

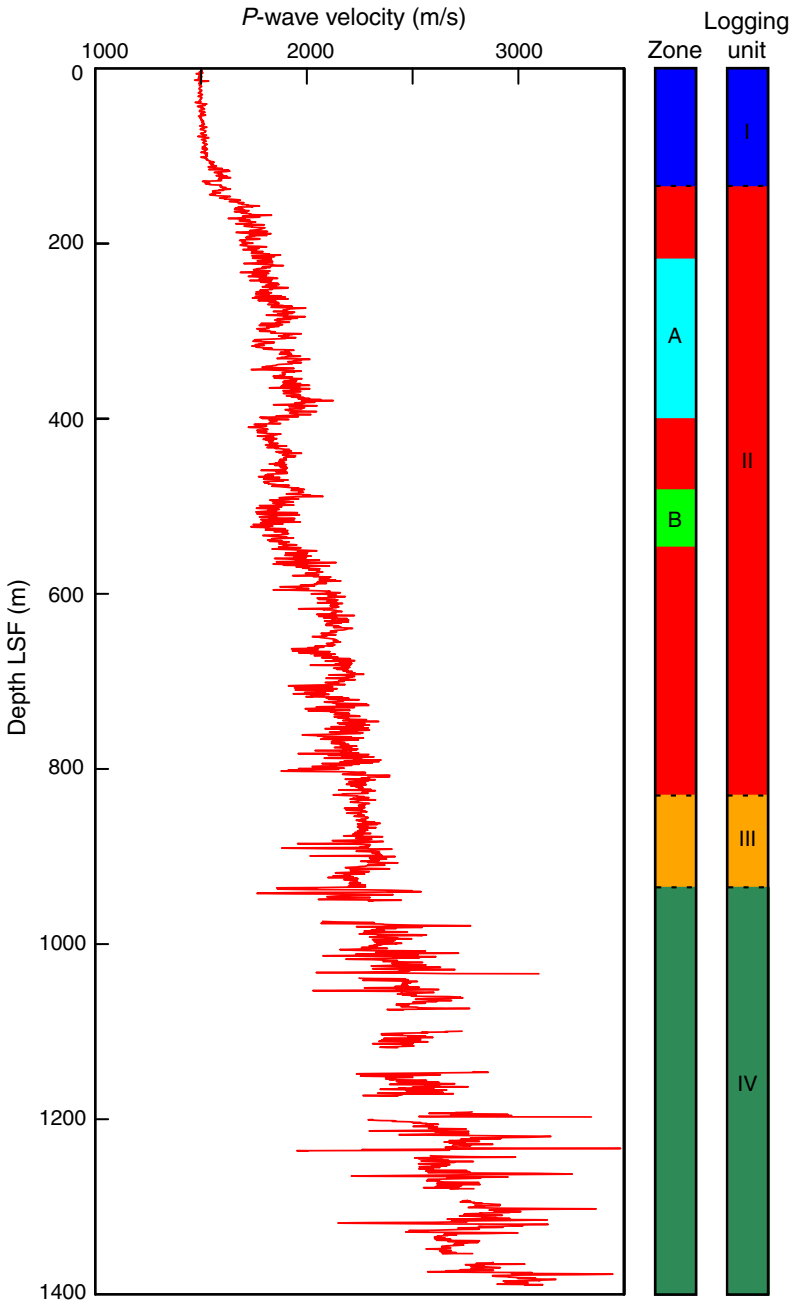

Figure F26. Comparison between sonic *P*-wave velocity and bit resistivity in Hole C0002A. **A.** Plot of *P*-wave velocity vs. bit resistivity. a = basin formations above the bottom-simulating reflector (BSR) (purple and blue), b = basin formations below the BSR (red and orange), c = older accretionary prism (green). Note the resistivity axis is in a logarithmic scale. **B.** Velocity and resistivity logs.

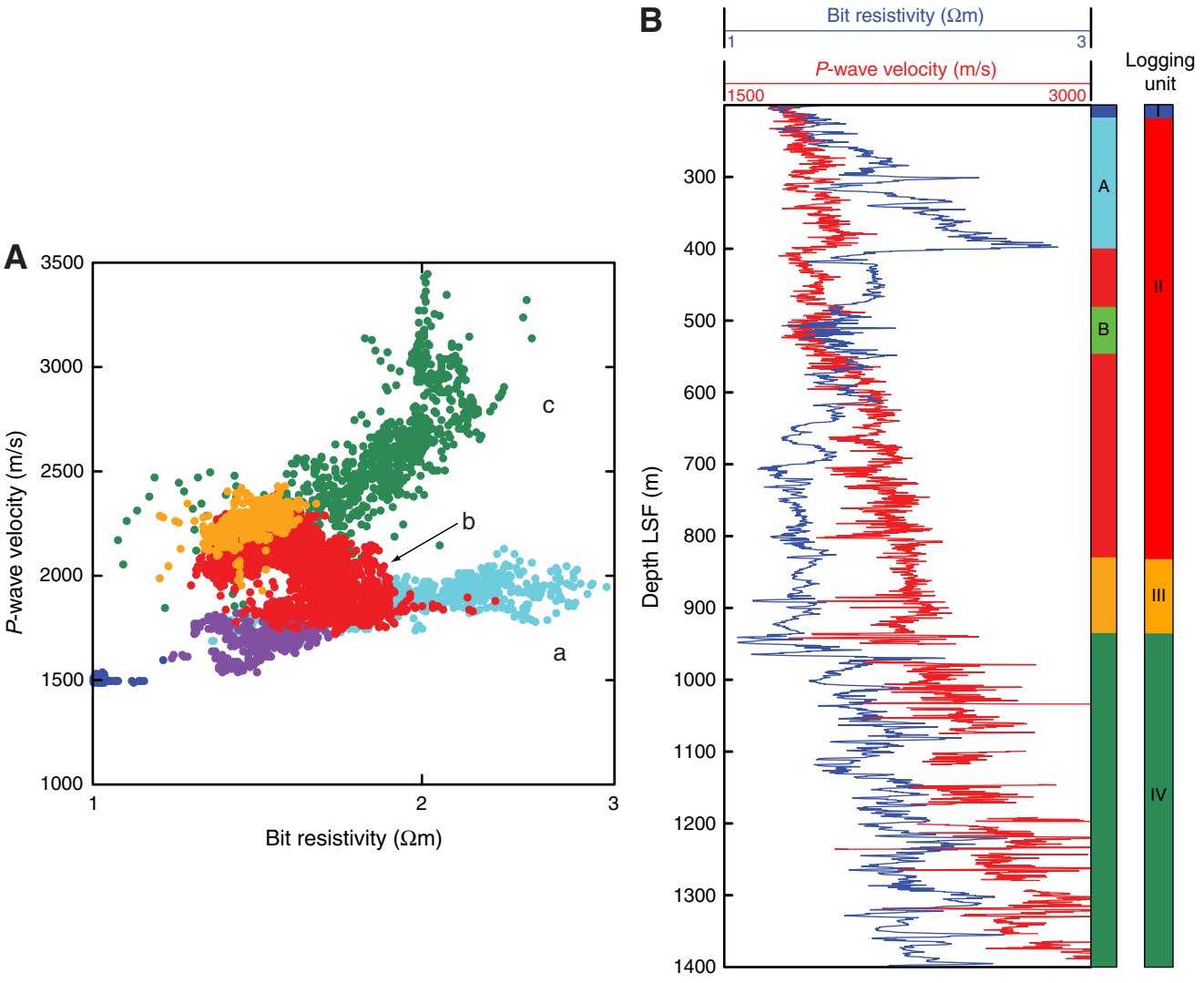

Figure F27. Plots of *P*-wave velocity vs. (**A**) neutron porosity, (**B**) density porosity, (**C**) bit resistivity–derived porosity, and (**D**) ring resistivity–derived porosity. Purple and blue = basin formations above the bottom-simulating reflector (BSR), red and orange = basin formations below the BSR, green = older accretionary prism.

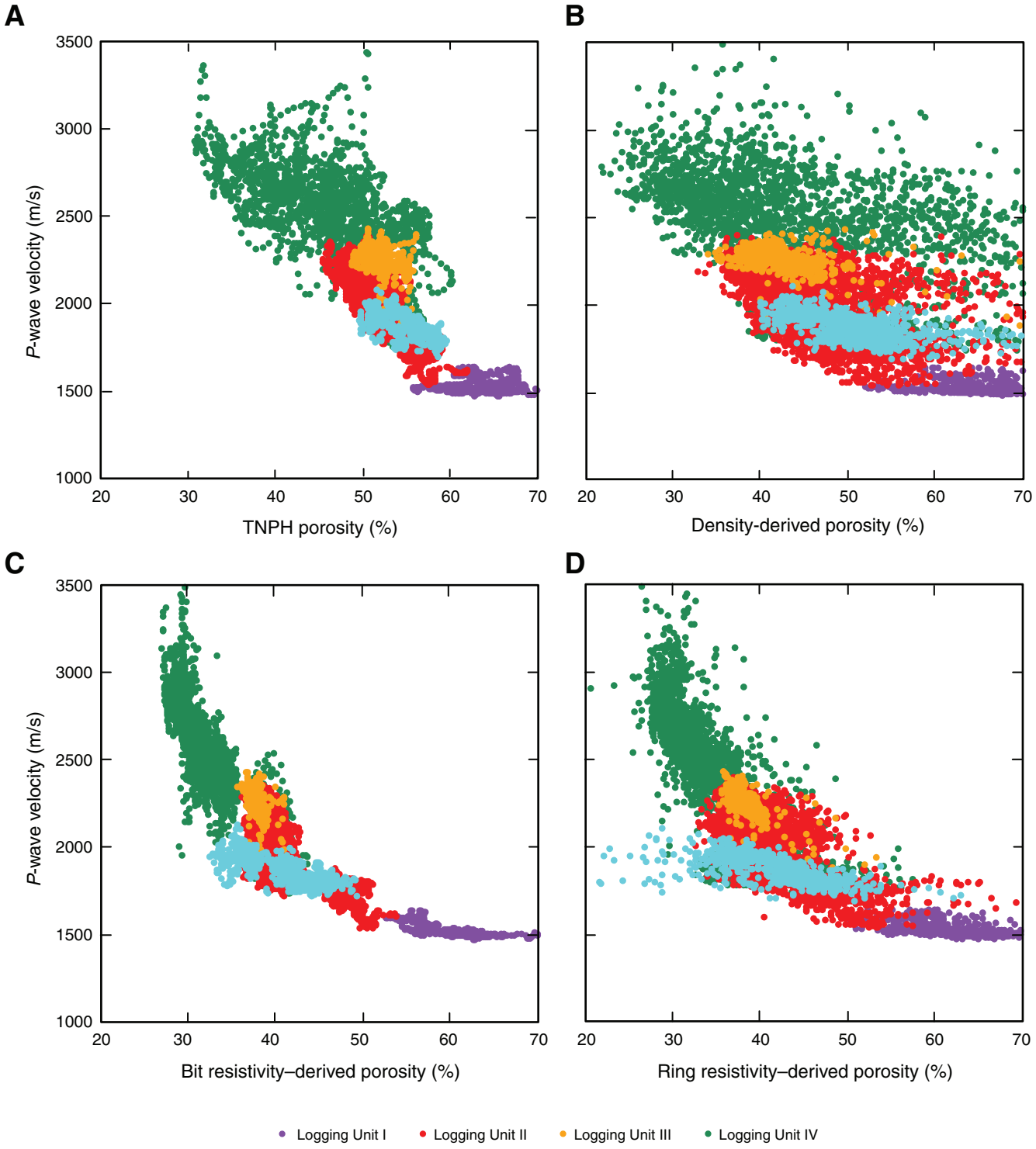

Figure F28. Shallow resistivity image (dynamic normalization) in Hole C0002A showing bedding and fracture orientations, dip, and fracture conductivity. Tadpole lines = dip direction of the plane. LSF = LWD depth below seafloor.

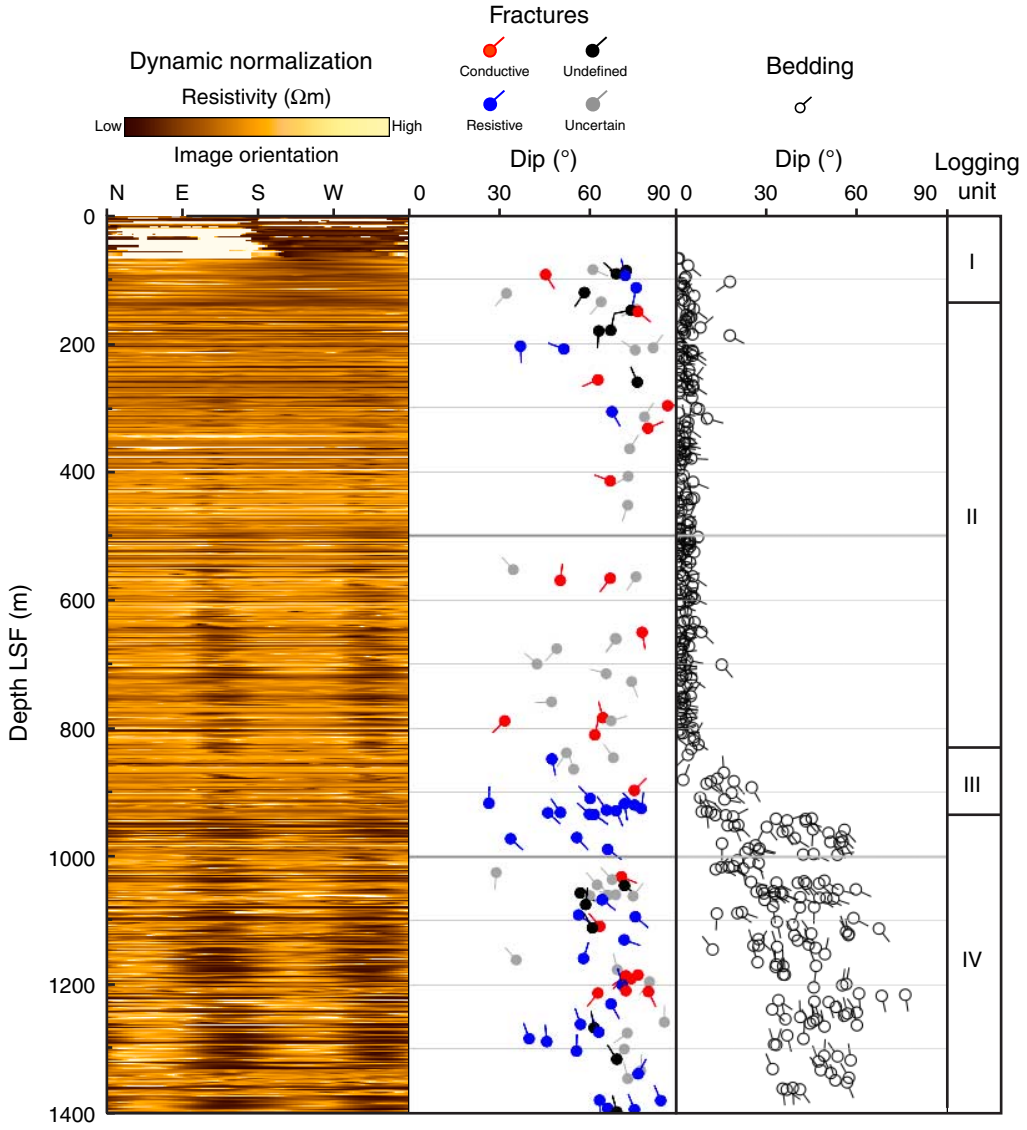

Figure F29. Equal area lower hemisphere stereographic projection of poles to bedding planes in (**A**) the forearc basin, logging Units I (0–136 m LWD depth below seafloor [LSF]), II (136–830 m LSF), and III (830–936 m LSF) and (**B**) the prism, logging Unit IV (936–1400 m LSF). Left panel data identified in borehole images; right panel data determined from 3-D seismic data (Table T6).

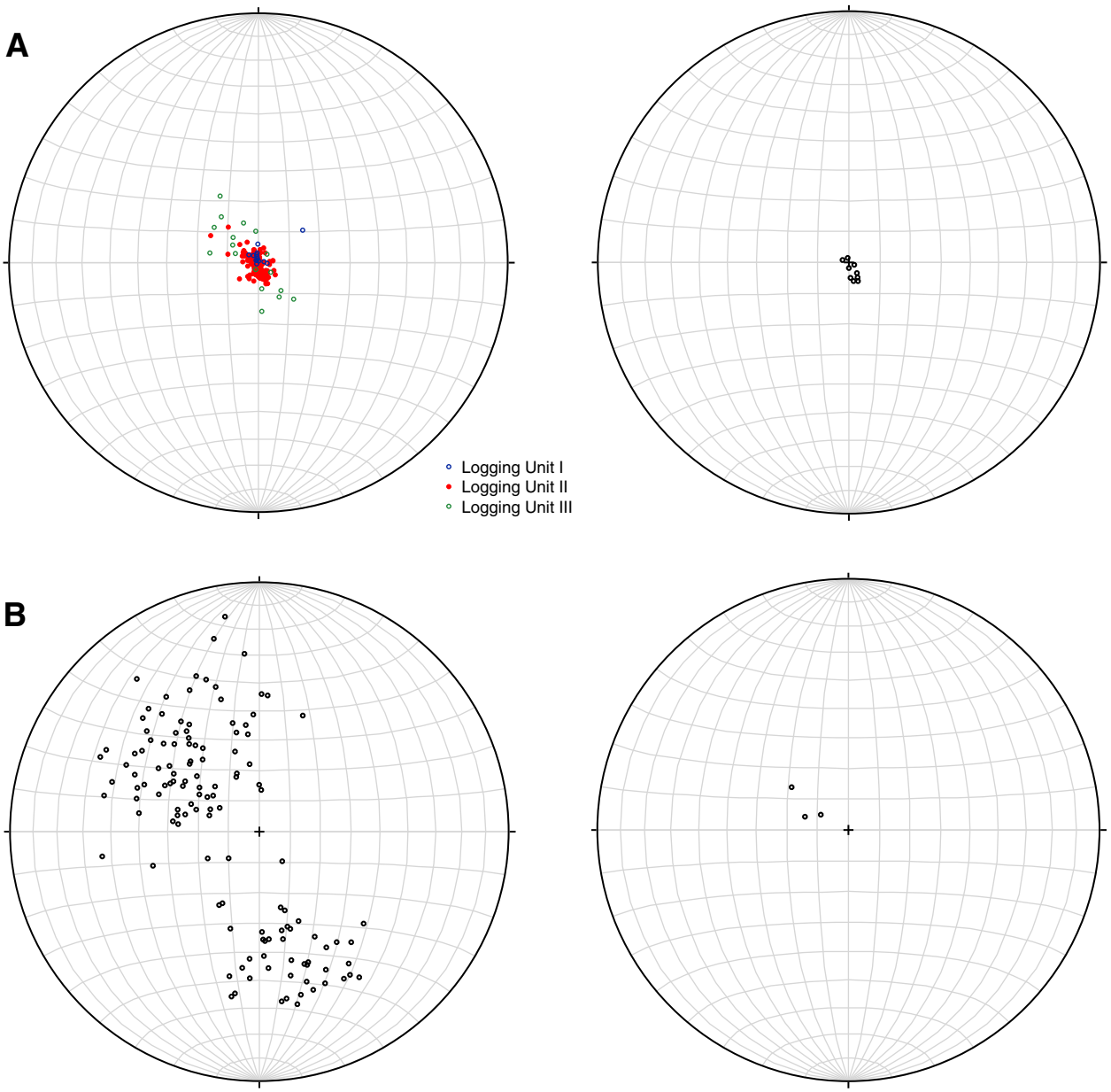

Figure F30. Resistivity image (static normalization shallow) of logging Unit III (830–936 m LWD depth below seafloor [LSF]) with fracture and bedding interpretation and ring resistivity and gamma ray logs. Inset shows fractured base of this unit (~915–935 m LSF). Tadpole lines = dip direction of the plane.

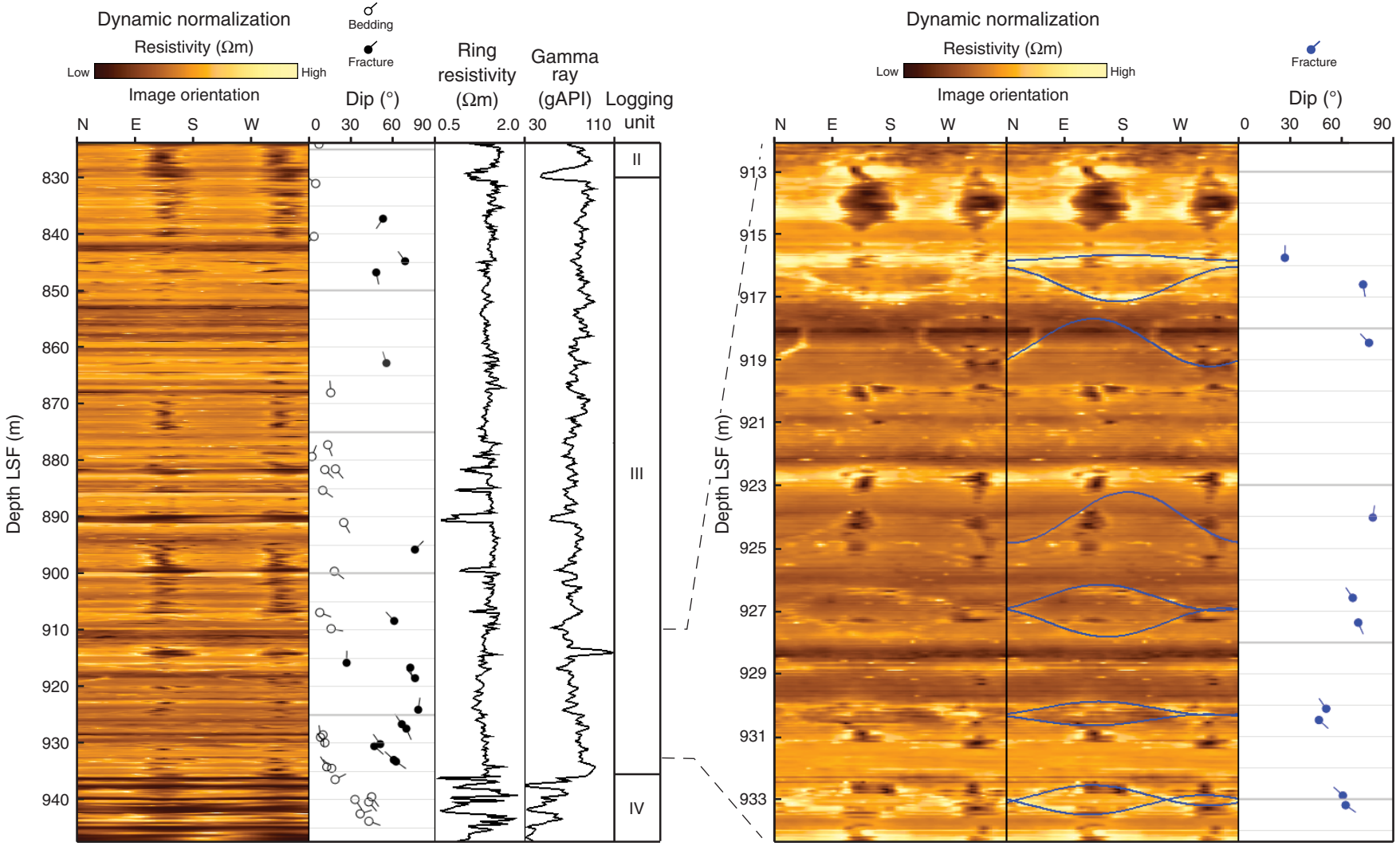

Figure F31. Fracture frequency with depth for Sites C0001 and C0002. Site C0001 in the active prism has a significantly higher fracture density than Site C0002 in the forearc basin and older prism. Within Site C0002, the prism is more fractured than the forearc basin; the latter has regions of more intense fracturing at 100–200 and ~800–1000 m LWD depth below seafloor (LSF) (including logging Unit III). Bin size = 20 m.

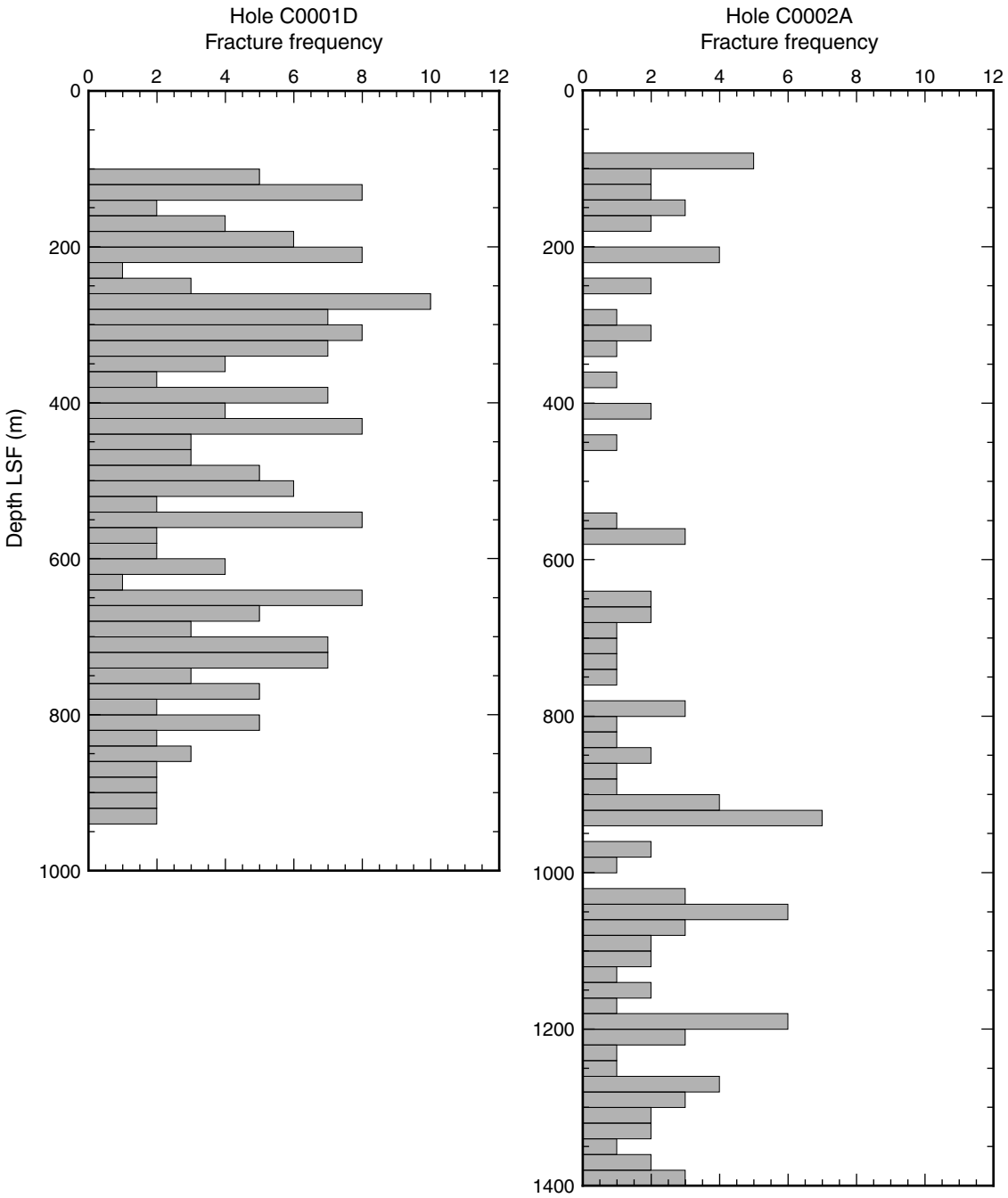

Figure F32. Equal area lower hemisphere stereographic projection of poles to fracture planes for (**A**) forearc basin, (**B**) prism, and (**C**) all fractures differentiated according to conductivity. Rose diagrams represent fracture azimuths (shown as dip direction –90°), preserving dip direction information.

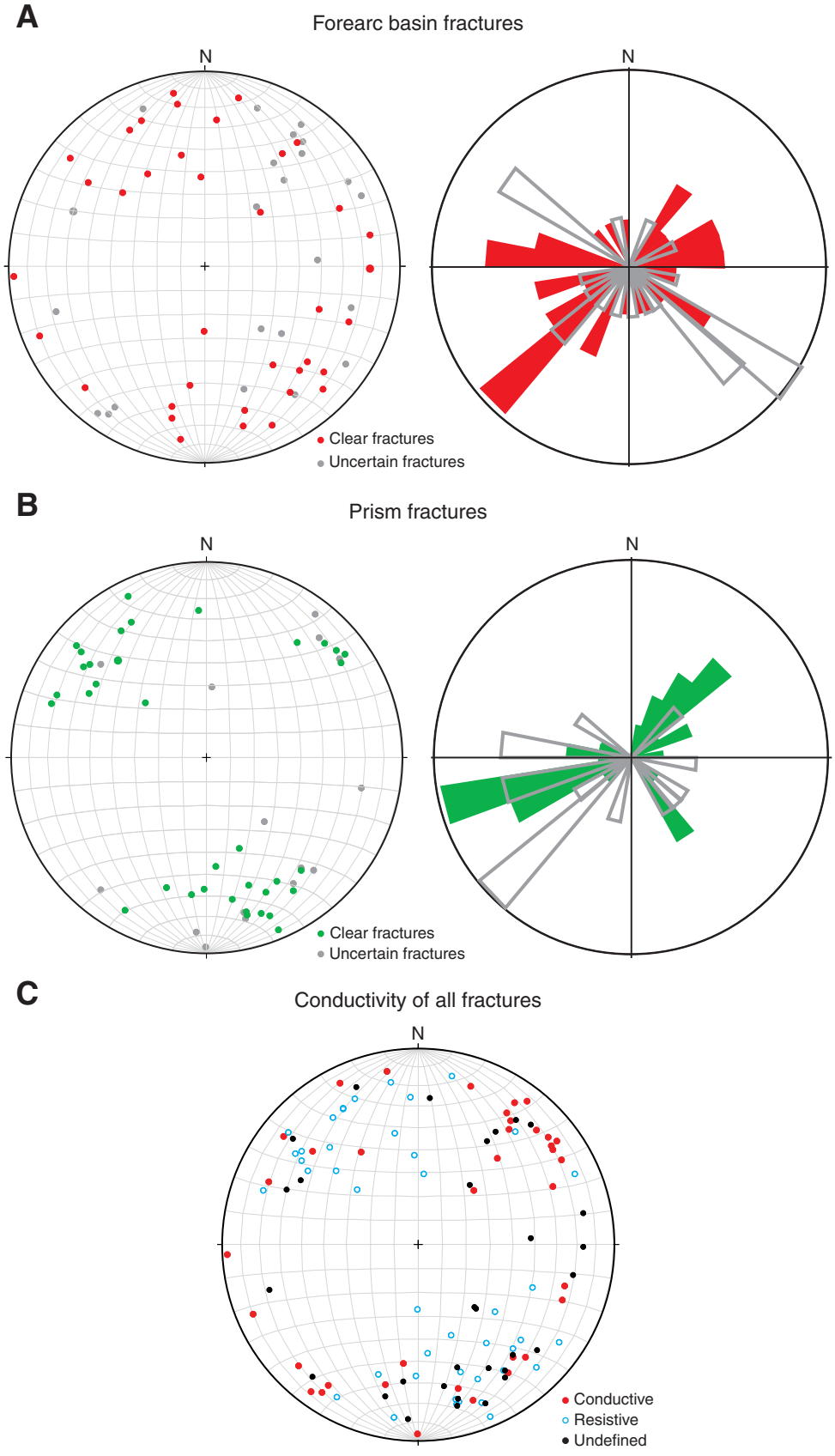

Figure F33. Normal fault displacement of a bed within the forearc basin (649 m LWD depth below seafloor [LSF]). The fracture cannot clearly be seen, but its azimuth and dip can be estimated from the displacement. Breakouts oriented northwest–southeast are clearly seen as conductive vertical lines 180° apart. Static normalization shallow resistivity image. 3-D = three-dimensional, tadpole lines = dip direction of the plane.

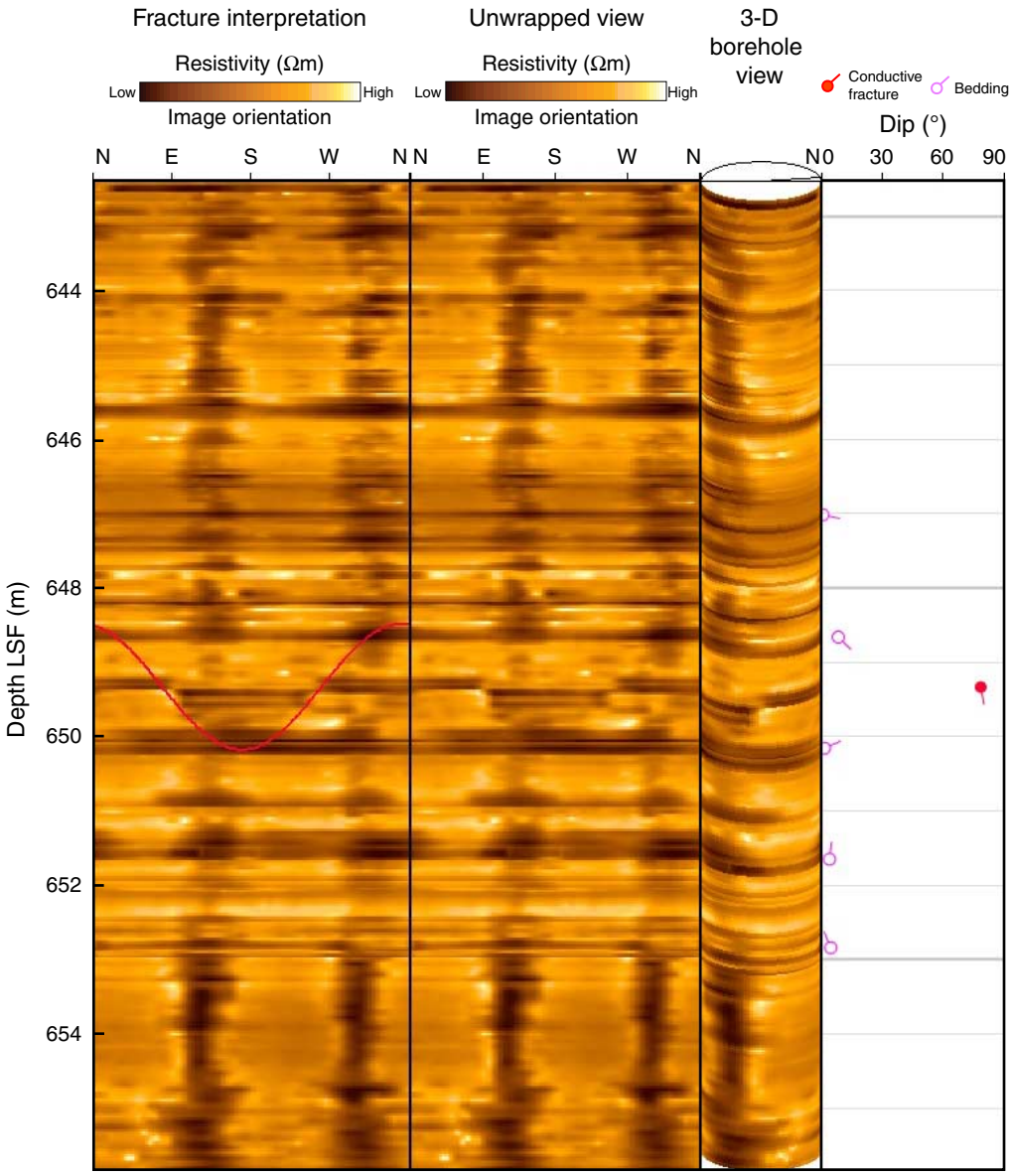

Figure F34. Steeply dipping conductive conjugate fractures in the prism (1207–1210 m LWD depth below seafloor [LSF]). Static normalized shallow resistivity image. 3-D = three-dimensional, tadpole lines = dip direction of the plane.

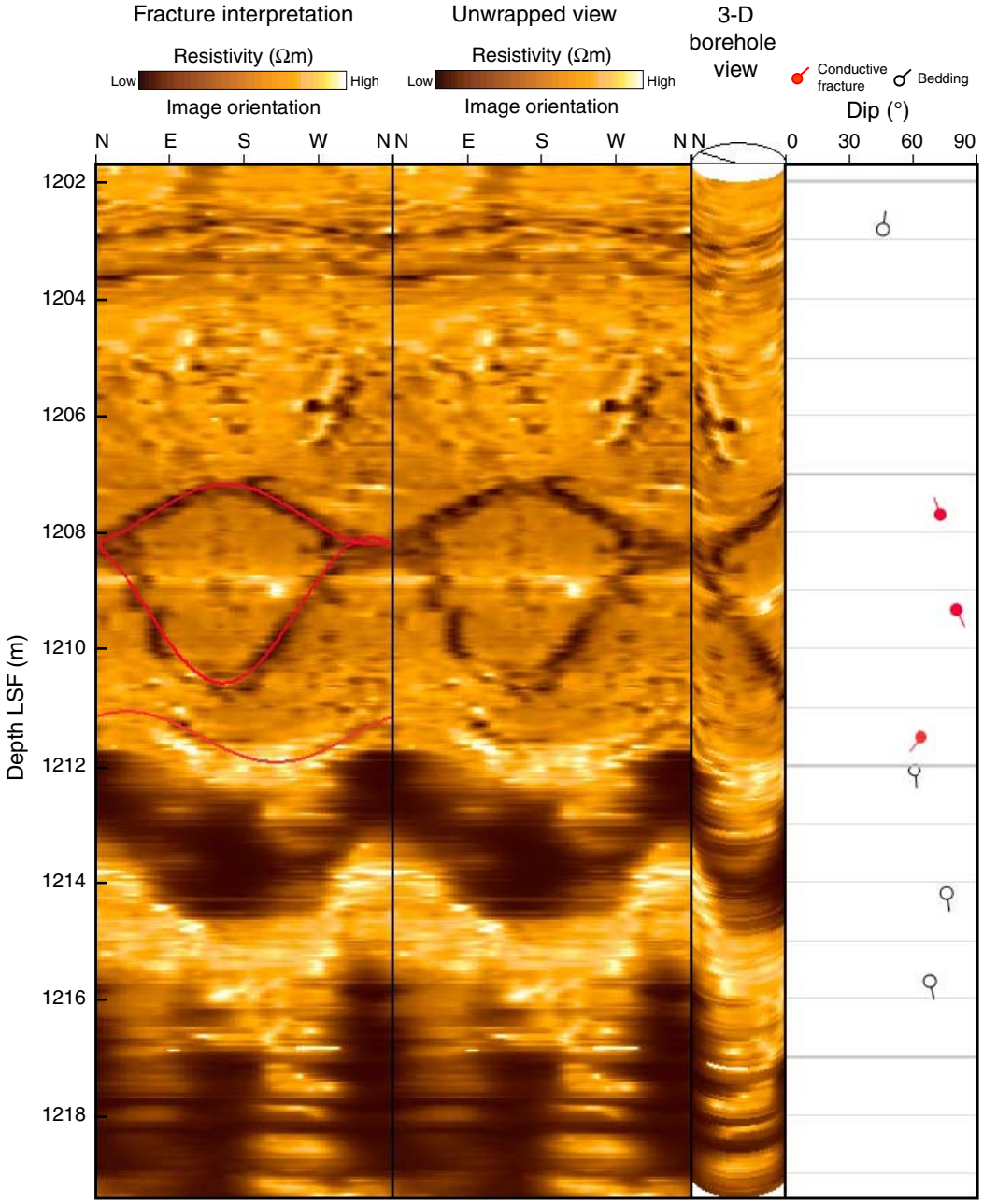

Figure F35. Histograms of borehole breakouts. **A.** Azimuth of breakouts. Azimuths are symmetrically distributed around mean value of 134°. **B.** Breakout width. Note tail extending toward larger breakout widths, which are concentrated in logging Unit VI (see Fig. F36).

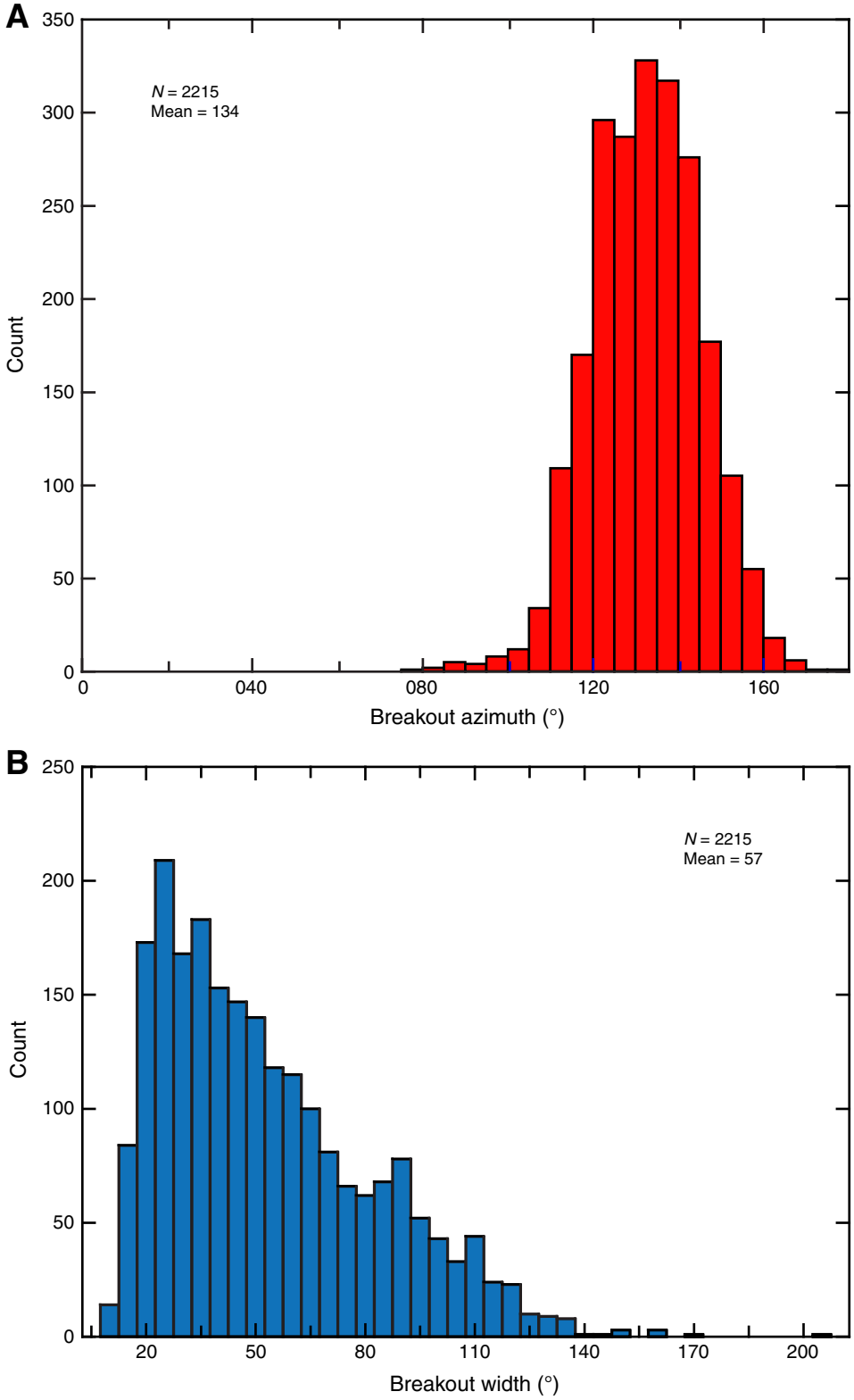

Figure F36. Variation of borehole breakouts with depth. **A.** Azimuth. Black line = 100-point moving average illustrating general trend from mean azimuth of 120° at 200 m LWD depth below seafloor (LSF) to 145° at 1400 m LSF. **B.** Breakout width. Note sharp increase in breakout width at top of logging Unit IV.

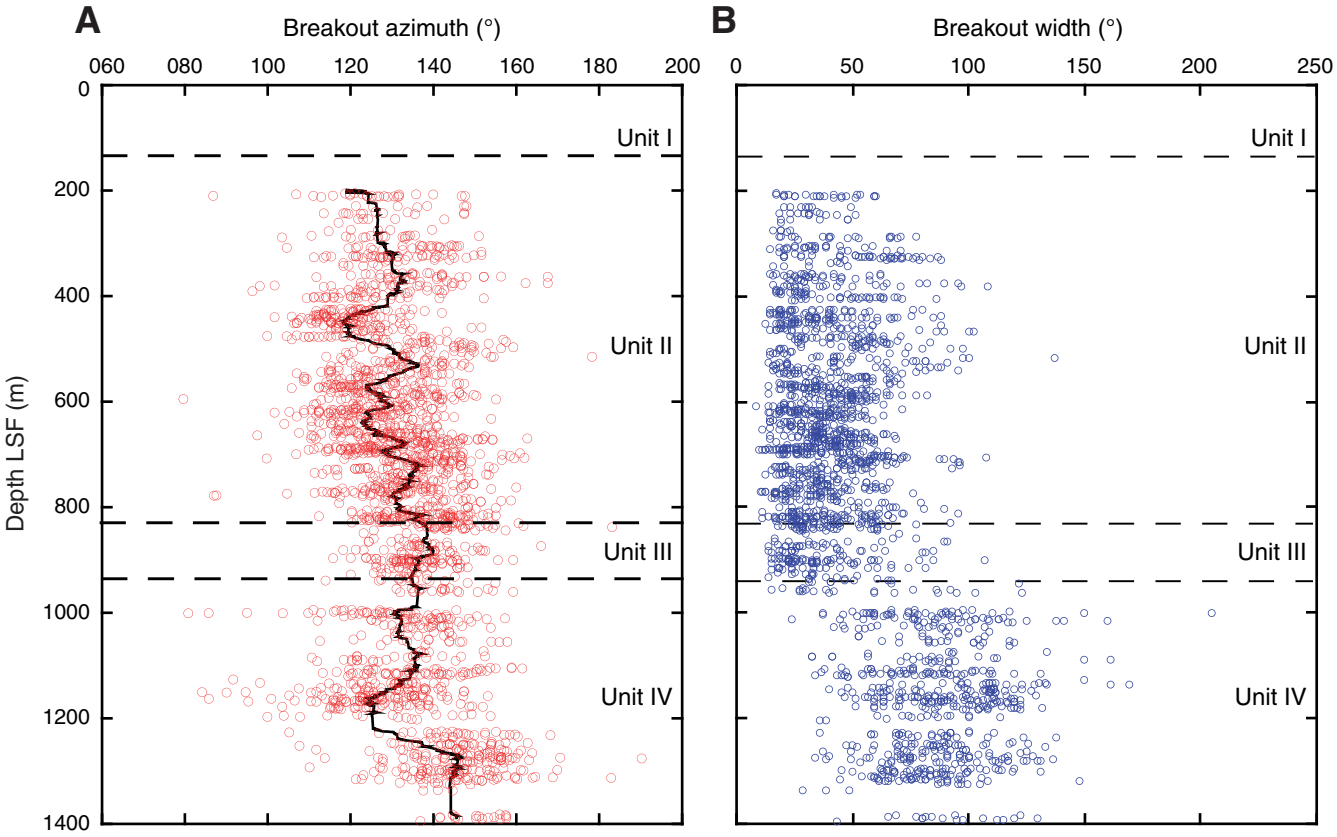

Figure F37. Stress polygons and likely stress regimes based on breakout widths and estimated uniaxial compressive strength (UCS) values at two depths in Hole C0002A. **A.** Forearc basin. **B.** Prism. S_{Hmax} and S_{hmin} lie within the stress polygon, to the right (or below) the red line and along a trajectory of rock strength, parallel to the blue lines. LSF = LWD depth below seafloor. TF = thrust faulting, SS = strike-slip faulting, NF = normal faulting.

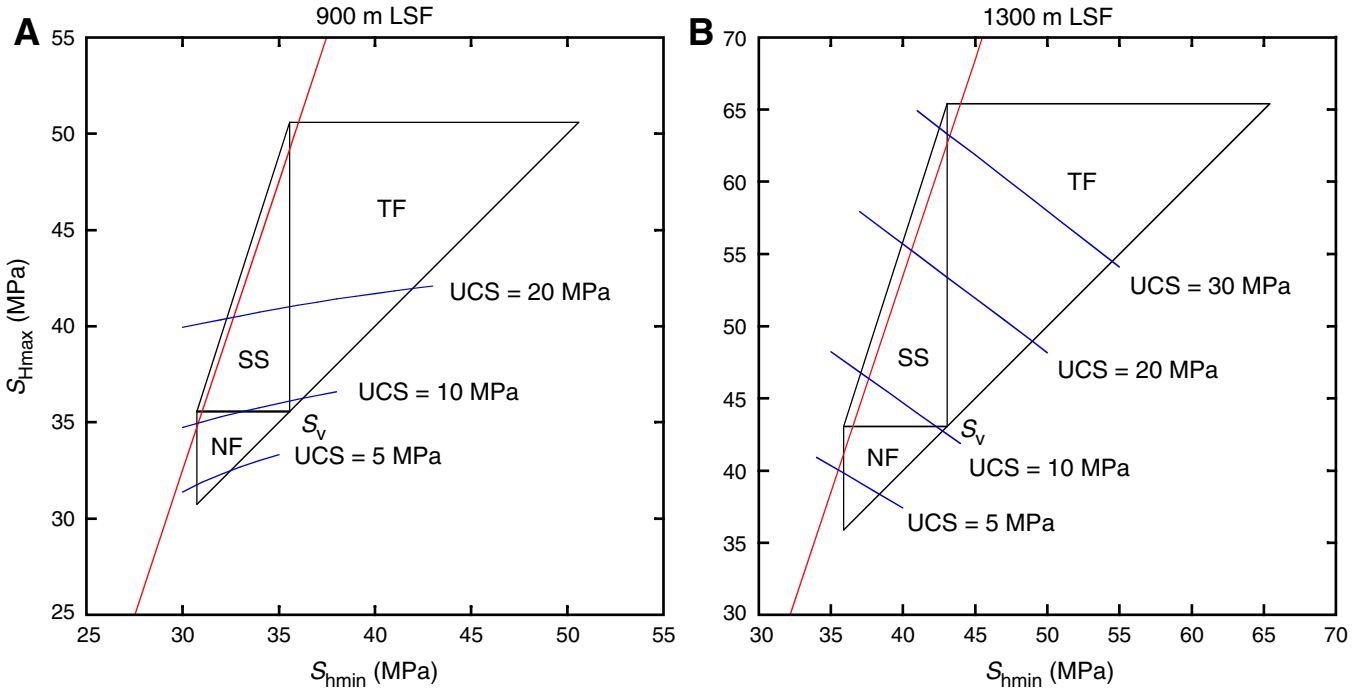

Figure F38. A. Time slice of prestack time-migrated seismic volume at 2888 ms two-way traveltime. Note contorted shape of basin and presence of faults of several different orientations. **B.** Scaled-up view of the area of the time slice near the borehole. Faults that exist close to the site are displayed with overlapping squares and follow consistent trends. Blue star = location of Hole C0002A, red shades = positive amplitude, gray shades = negative amplitude, white area = seafloor depression between forearc basin and thrust sheets of active accretionary prism (Martin et al., 2007).

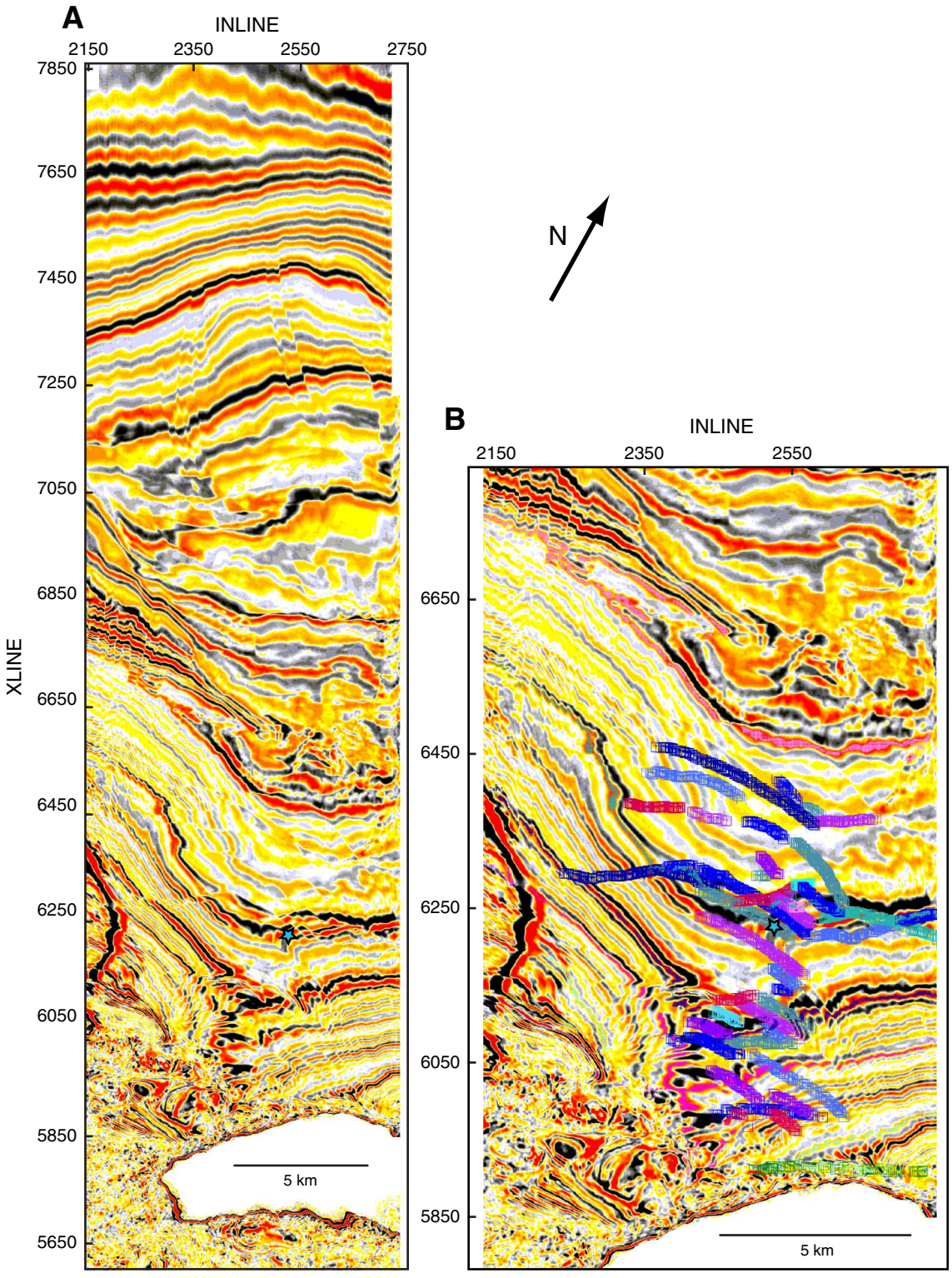

Figure F39. *P*-wave interval velocity from check shots (left of hole location) and sonic log (right of hole location) superimposed on check shot–corrected prestack depth-migrated seismic profile through Hole C0002A. LSF = LWD depth below seafloor, VE = vertical exaggeration.

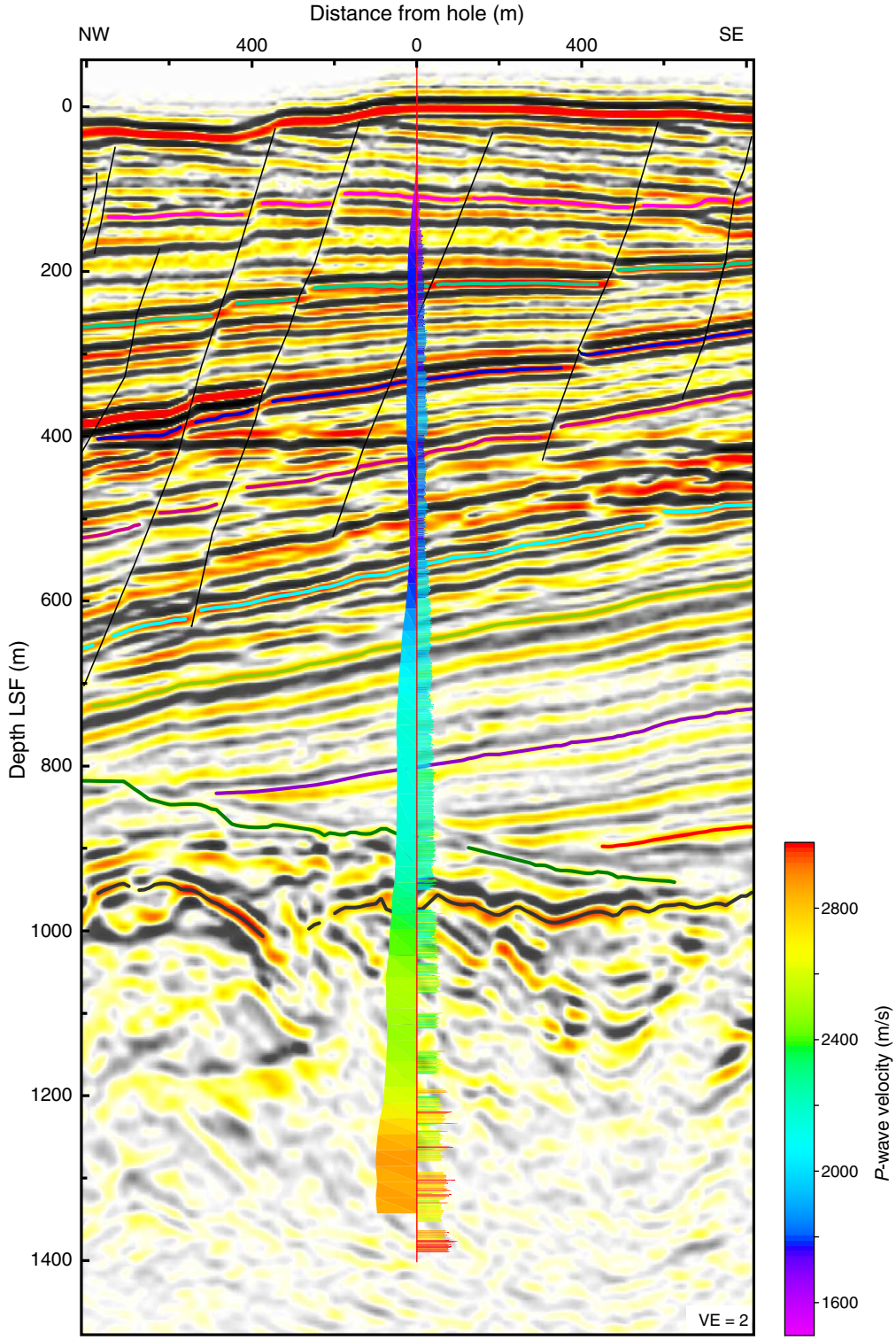

Figure F40. Density log superimposed on check shot–corrected prestack depth-migrated seismic profile through Hole C0002A. LSF = LWD depth below seafloor, VE = vertical exaggeration.

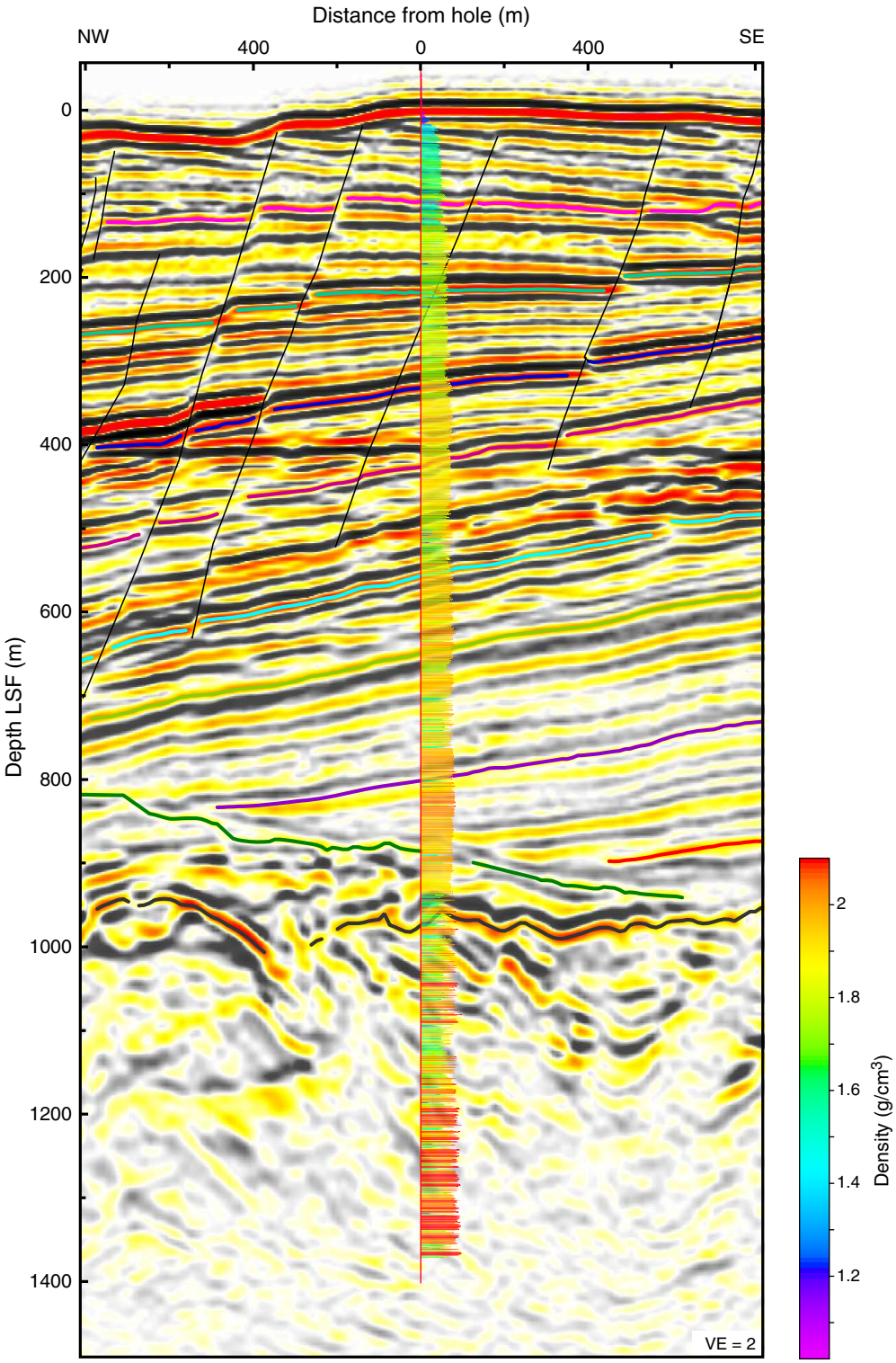

Figure F41. Ring resistivity log superimposed on check shot–corrected prestack depth-migrated seismic profile through Hole C0002A. LSF = LWD depth below seafloor, VE = vertical exaggeration.

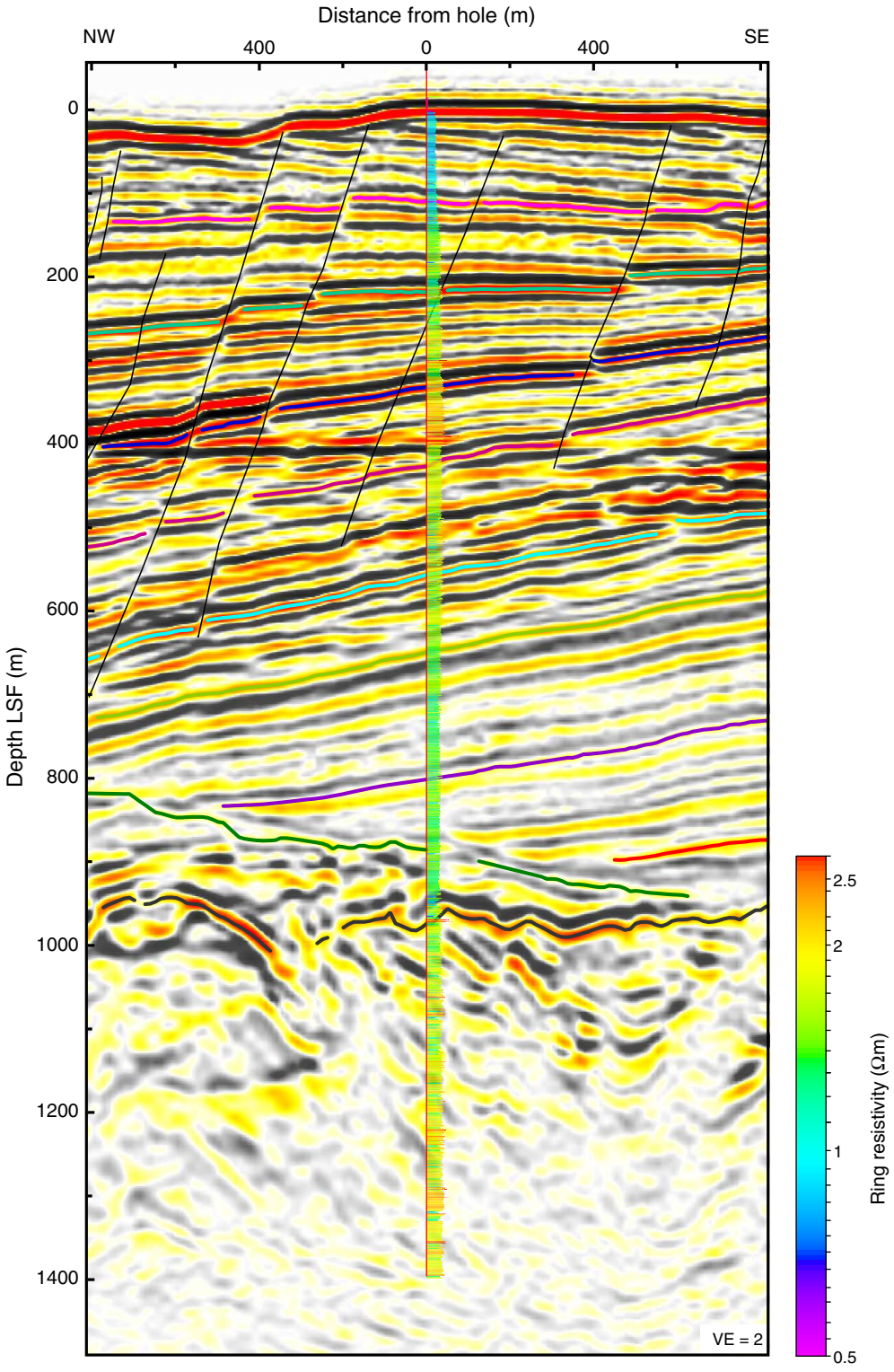

Figure F42. Gamma ray log superimposed on check shot–corrected prestack depth-migrated seismic profile through Hole C0002A. LSF = LWD depth below seafloor, VE = vertical exaggeration.

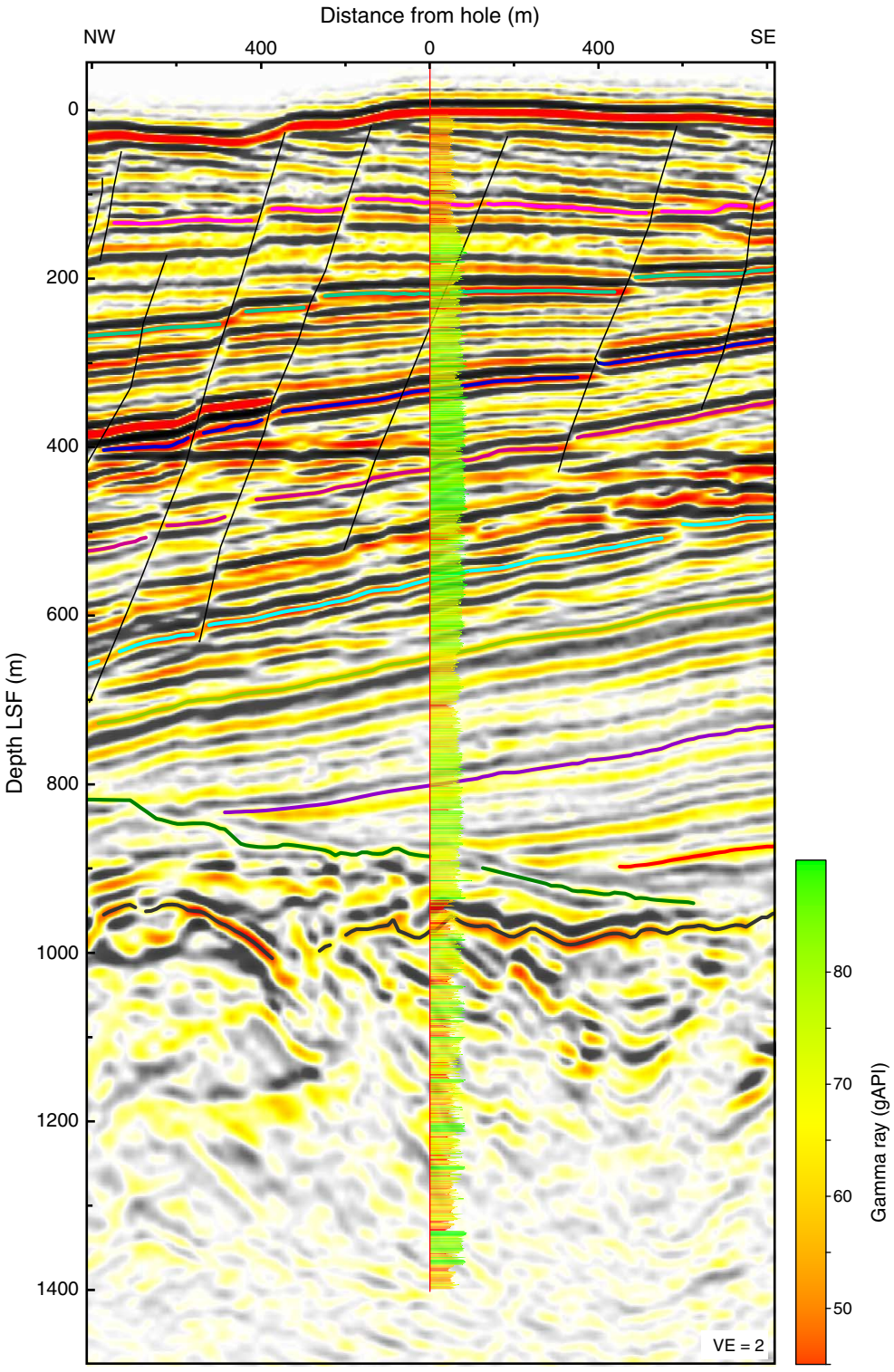

Figure F43. Caliper (hole diameter) log superimposed on check shot–corrected prestack depth-migrated seismic profile through Hole C0002A. LSF = LWD depth below seafloor, VE = vertical exaggeration.

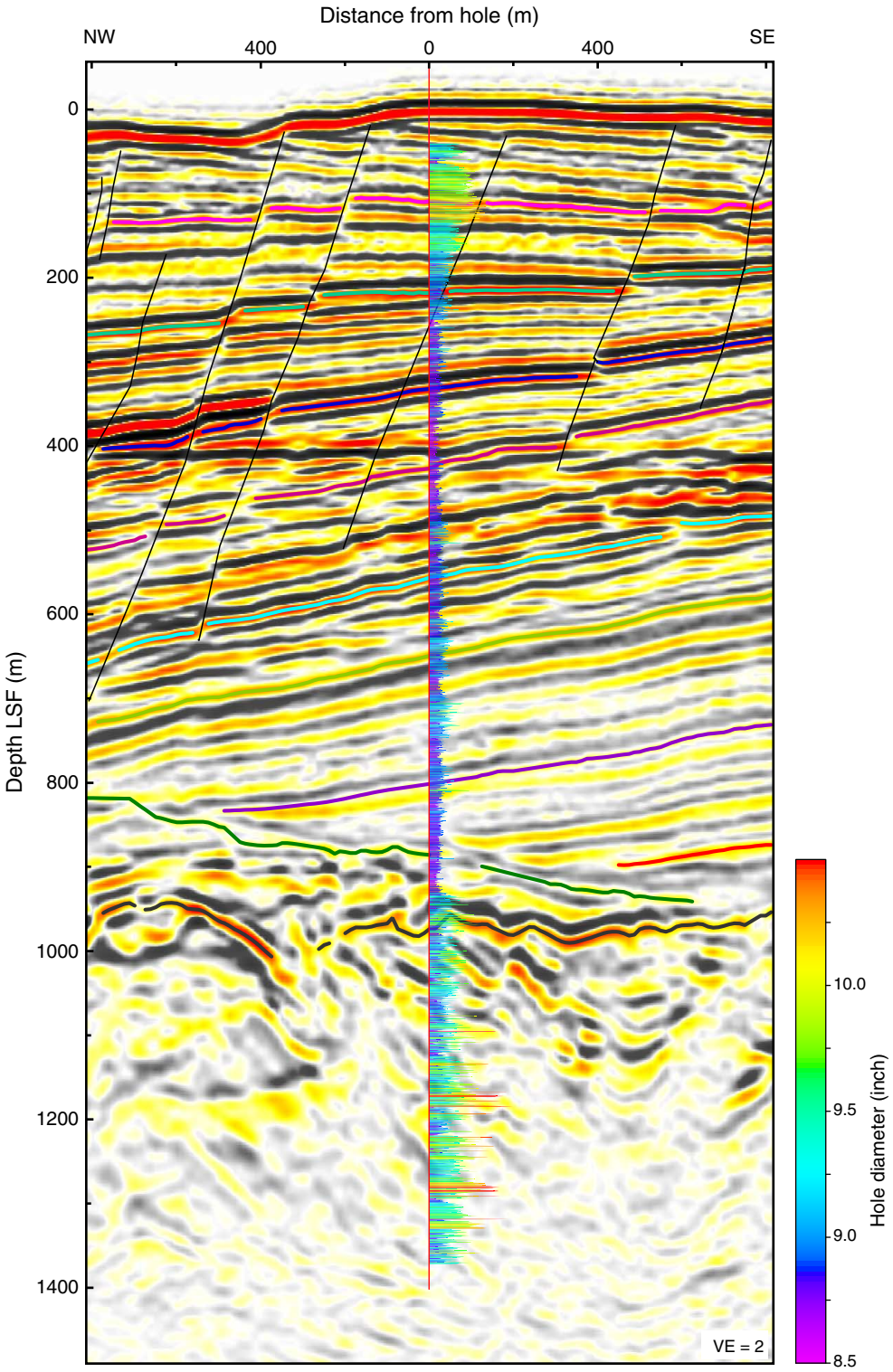

Figure F44. Neutron porosity log superimposed on check shot–corrected prestack depth-migrated seismic profile through Hole C0002A. LSF = LWD depth below seafloor, VE = vertical exaggeration.

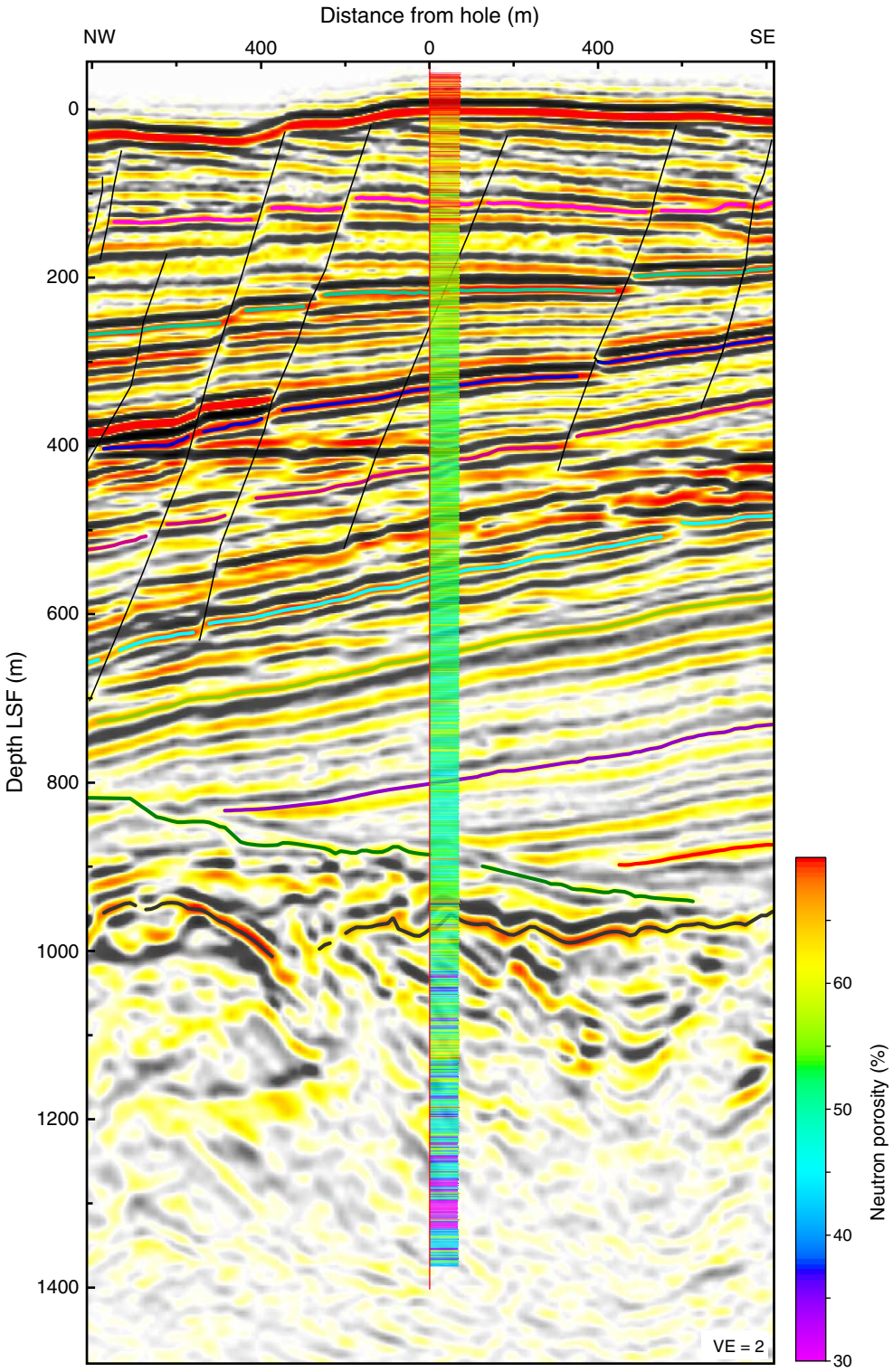

Figure F45. Photoelectric factor log superimposed on check shot–corrected prestack depth-migrated seismic profile through Hole C0002. LSF = LWD depth below seafloor, VE = vertical exaggeration.

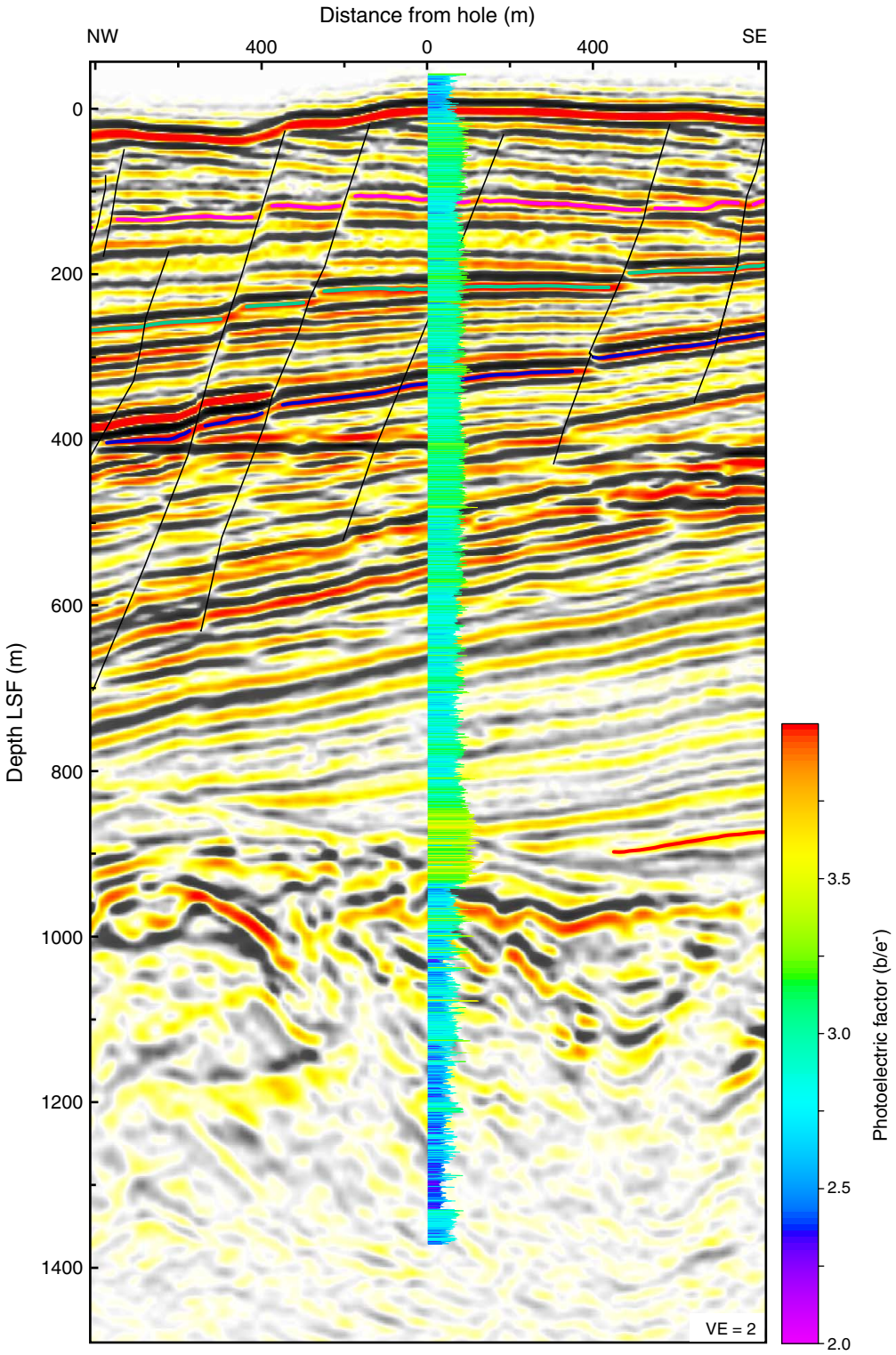

Figure F46. Log curves and local seismic section (variable density display method; red = positive, black = negative) at logging Unit I/II boundary. Data superimposed over Inline 2529 from the check shot–corrected prestack depth-migrated seismic volume near Hole C0002A. **A.** Logging units. SU = seismic unit. **B.** *P*-wave velocity. **C.** Gamma ray values. LSF = LWD depth below seafloor.

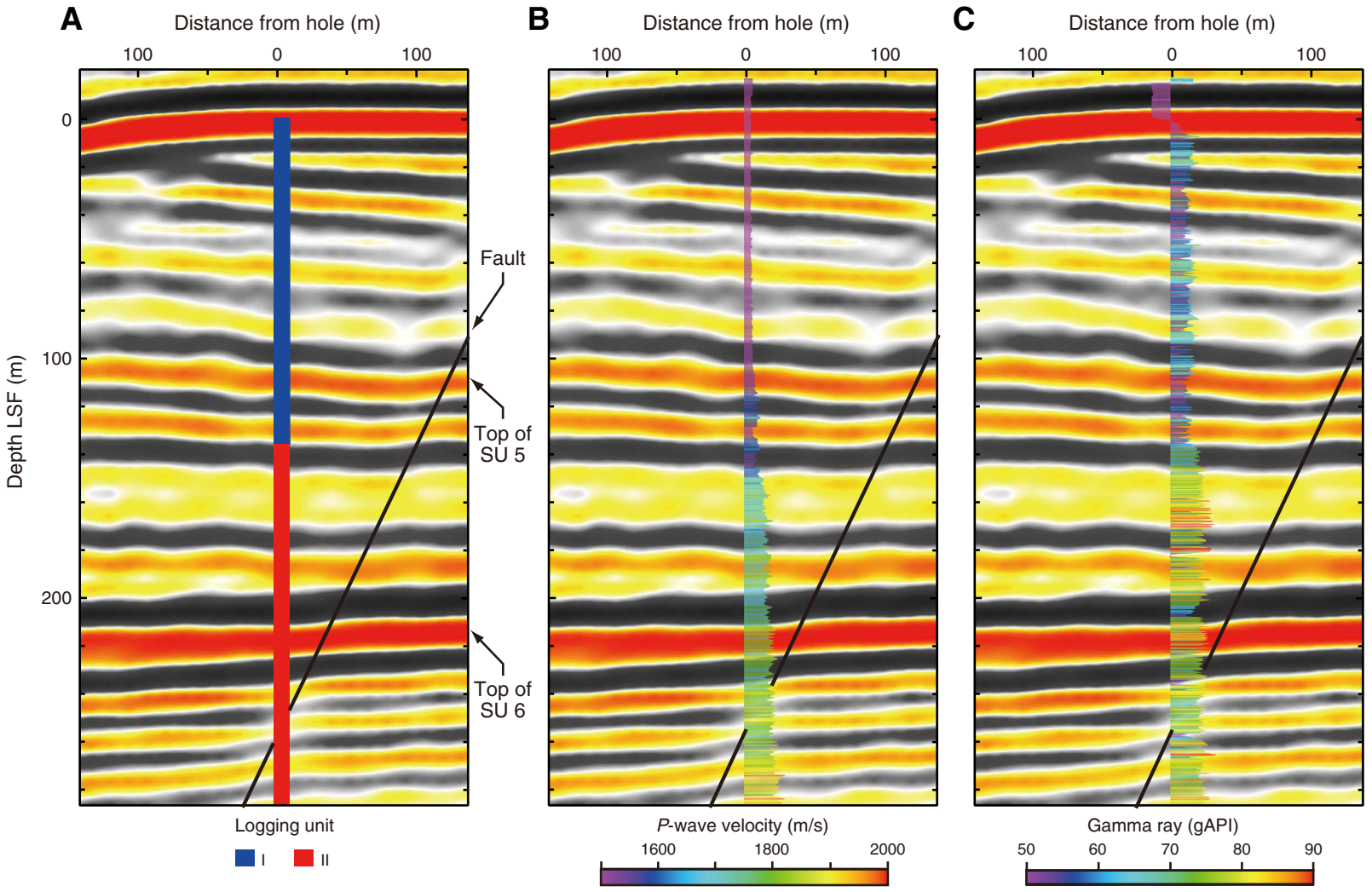

Figure F47. Log curves and local seismic section (variable density display method; red = positive, black = negative) at depths of Zones A and B. Data superimposed over Inline 2529 from the check shot–corrected prestack depth-migrated seismic volume near Hole C0002A. **A.** Zones. BSR = bottom-simulating reflector, SU = seismic unit. **B.** Ring resistivity data. **C.** *P*-wave velocity. LSF = LWD depth below seafloor.

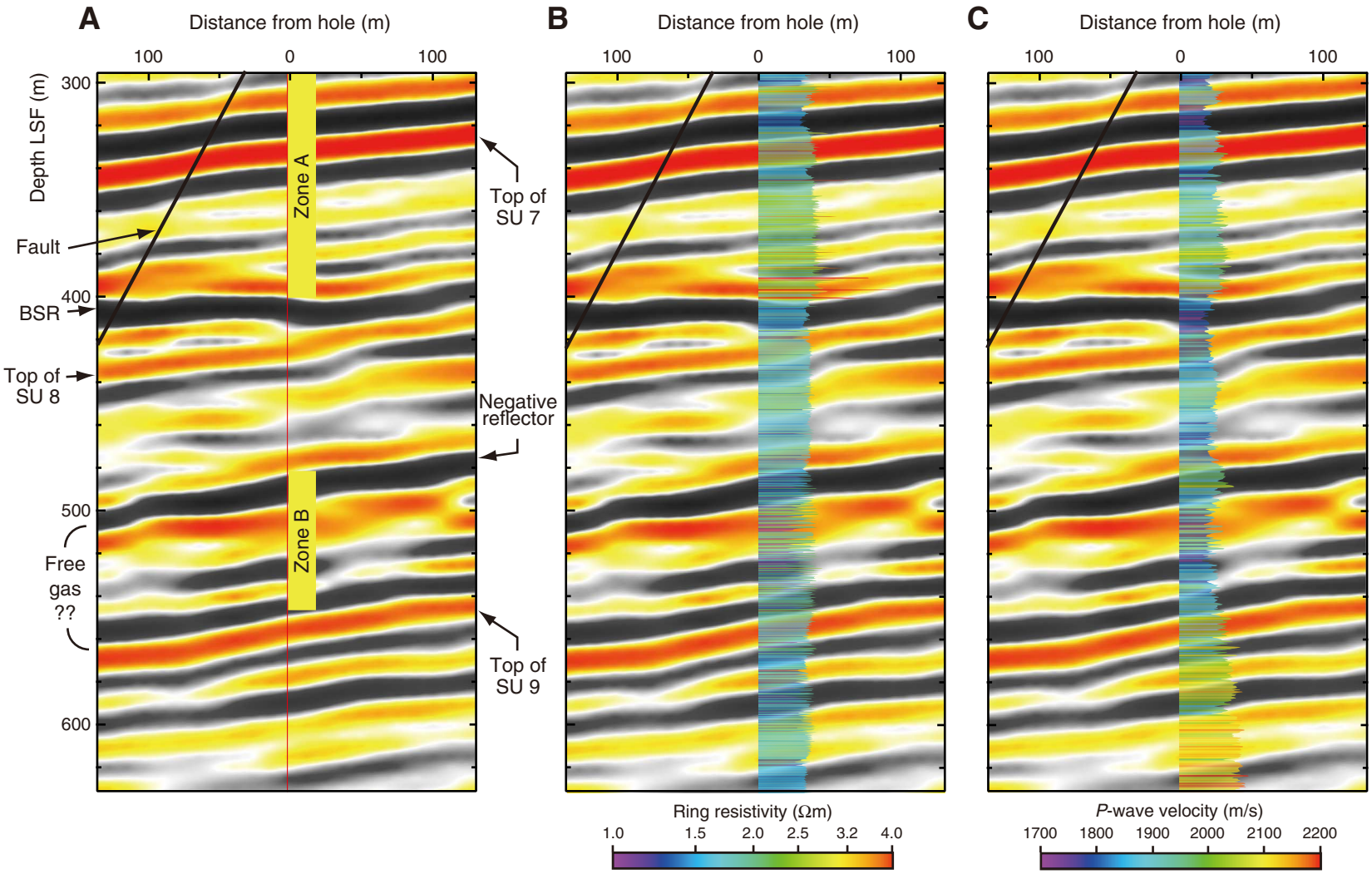

Figure F48. Log curves and local seismic section (variable density display method; red = positive, black = negative) at logging Unit III/IV boundary. Data superimposed over Inline 2529 from the check shot–corrected prestack depth-migrated seismic volume near Hole C0002A. **A.** Logging units. SU = seismic unit, Seds = Sediments, Acc. = Accretionary. **B.** Photoelectric factor (PEF) data. **C.** Gamma ray values. LSF = LWD depth below seafloor.

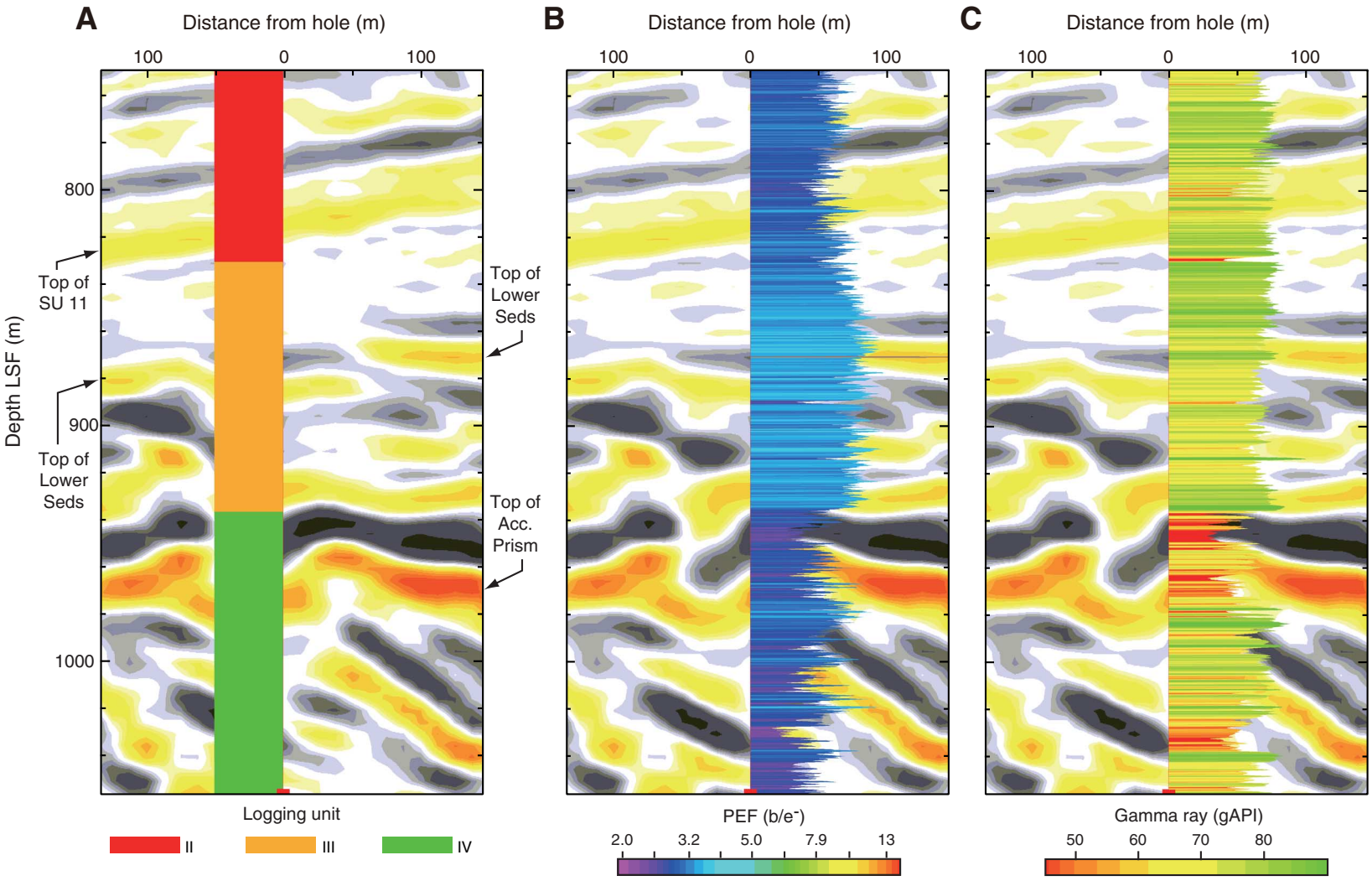

Figure F49. Check shot seismogram at Site C0002. First arrivals increase in time as sensor is deployed at increasing depth in the borehole. Slope of nearby first arrivals is an indicator of interval velocity.

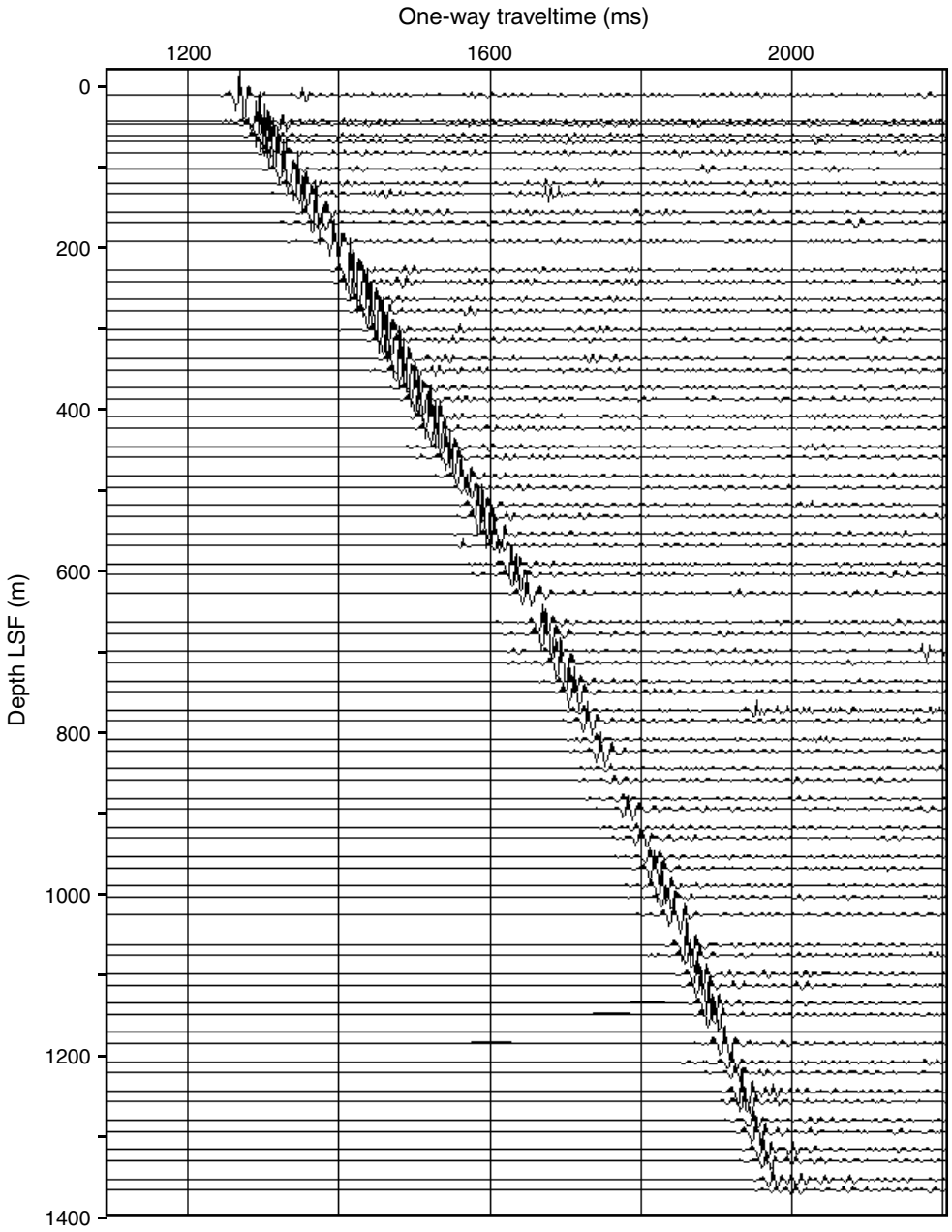

Figure F50. Comparison of check shot interval velocity and sonic log interval velocity as a function of depth at Site C0002. LSF = LWD depth below seafloor.

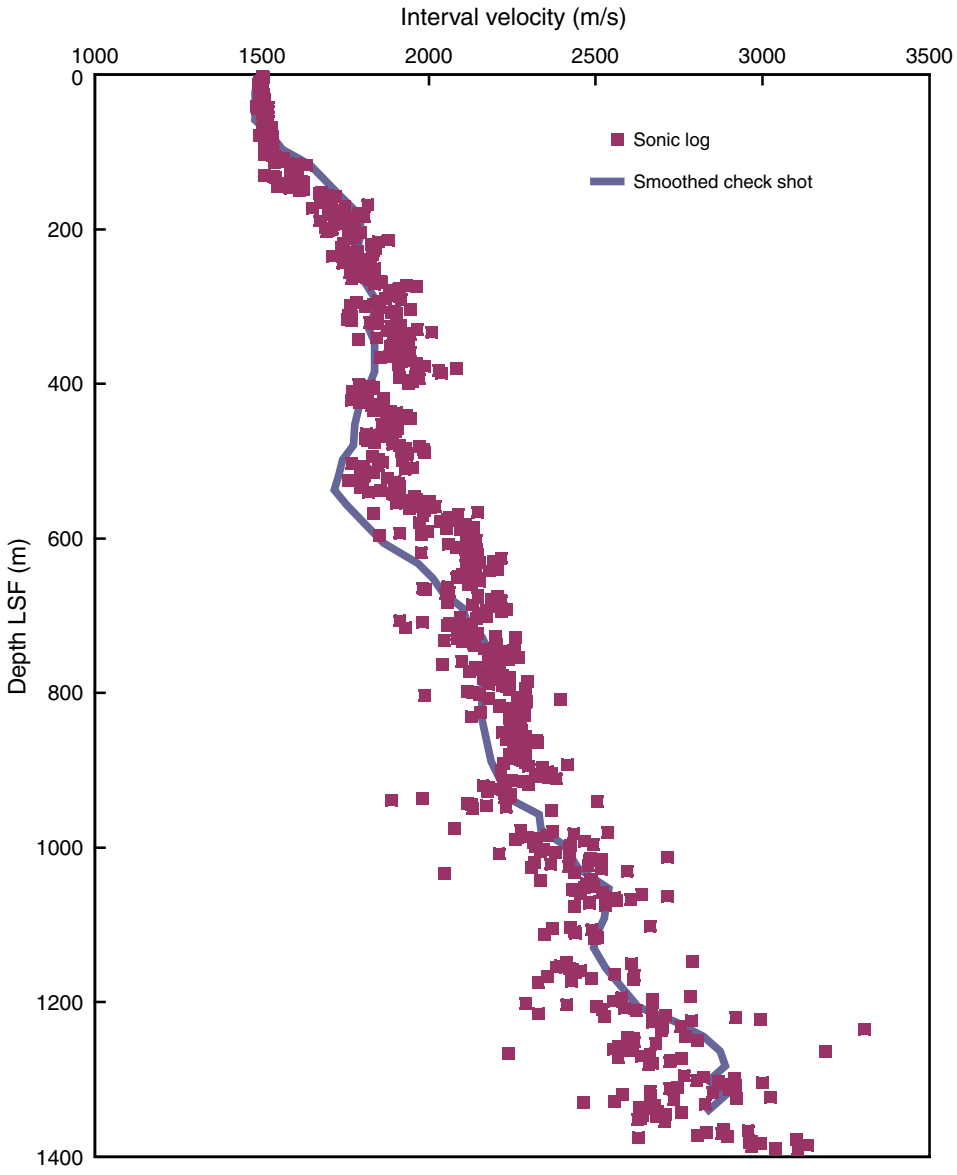

Figure F51. Relationship between vertical seismic profile (VSP) and a prestack time-migrated seismic profile from the site and to the northwest of Site C0002. Sections are aligned at the seafloor and are at the same time scale. Red lines in the VSP do not show particular reflections but illustrate expected slope of upgoing reflection arrivals and indicate their general relationship with the reflection profile. LSF = LWD depth below seafloor.

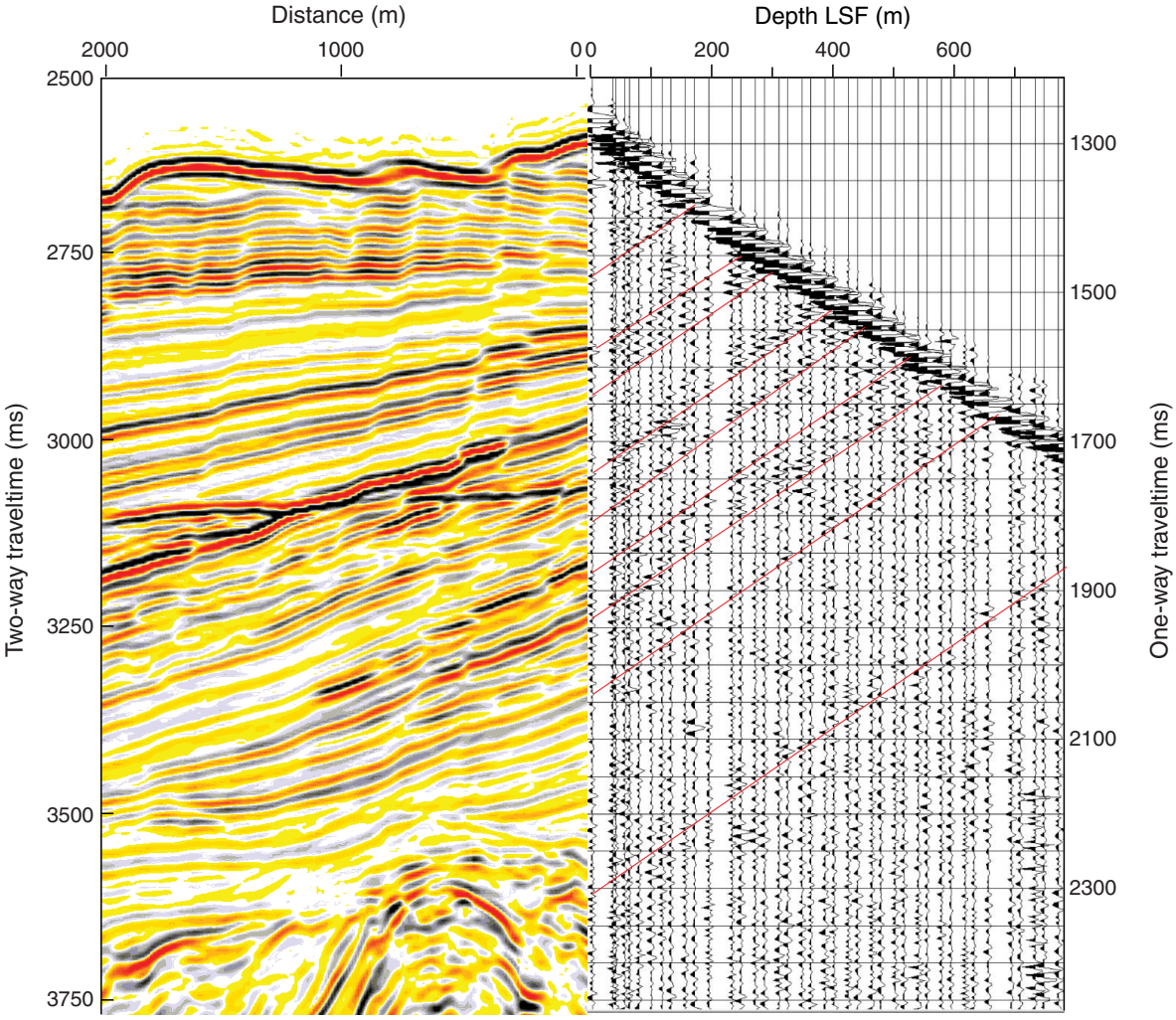

Figure F52. Synthetic seismogram test for Site C0002. Note correspondence of high caliper values, low gamma ray values suggestive of sand layers, and erroneous reflectors in the synthetic. **A.** Time vs. depth curve based on check shot. TWT = two-way traveltime. **B.** Sonic log (see text for description of interpolation). **C.** Image-derived density (IDRO) log (see text for description of filtering and interpolation). **D.** Computed synthetic (Synth.) seismogram shown as five identical traces side by side. **E.** Reflection coefficients (Refl. coeff.) determined from the input sonic and density logs. **F.** 256 ms deterministic wavelet (Wvlt.) used for the source wavelet. **G.** Fifteen traces of cross-line 6221 closest to borehole. **H.** Synthetic seismogram repeated with positive amplitude filled in red and negative amplitude filled in blue. **I.** Fifteen traces of Inline 2529 closest to borehole. **J.** Ultrasonic caliper (DCAV). **K.** Gamma ray (GR) log. LSF = LWD depth below seafloor.

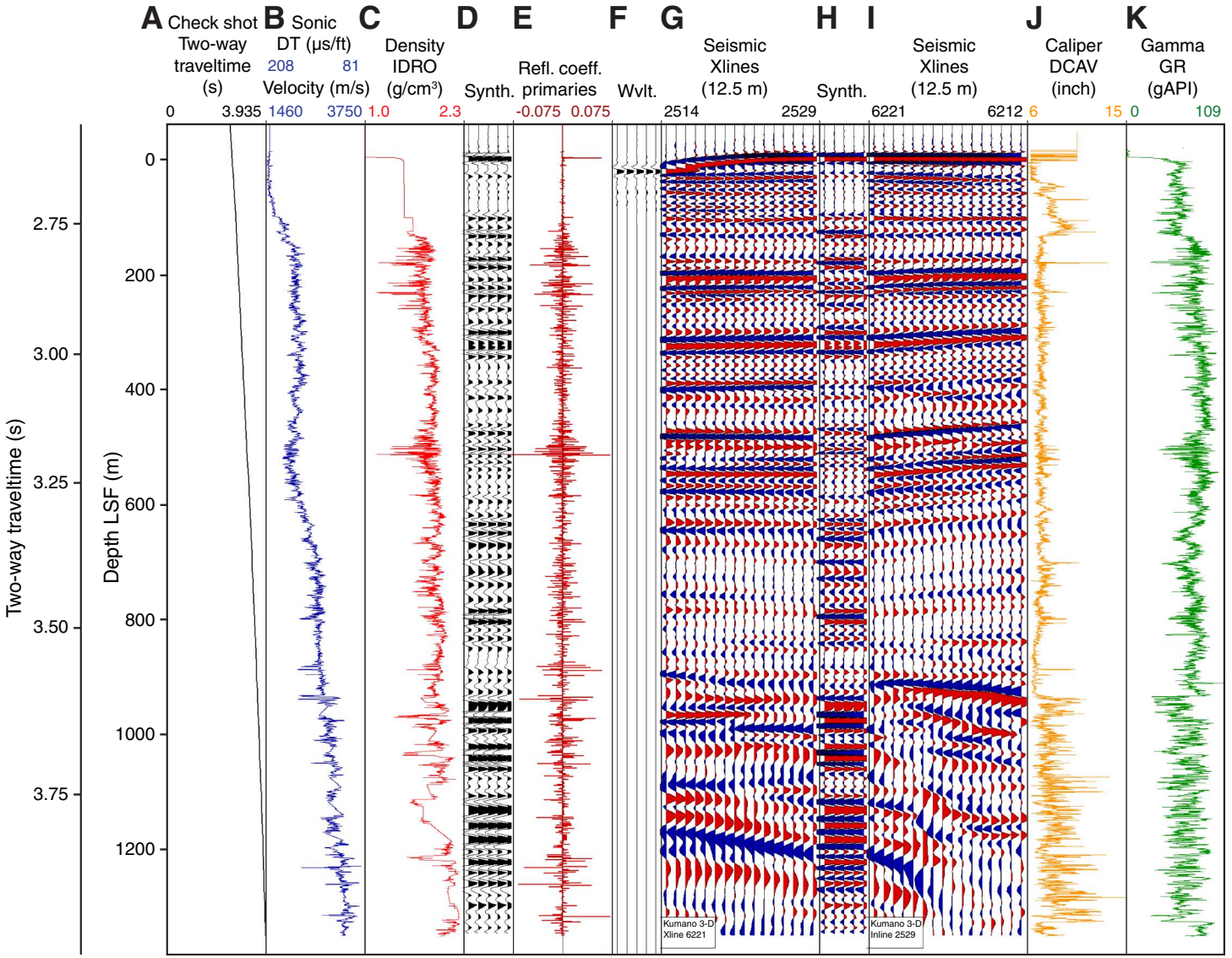

Table T1. Operations summary, Site C0002. (See table notes.)

Hole C0002A
Latitude: 33°18.0192′N
Longitude: 136°38.1810′E
Seafloor (drill pipe measurement from rig floor, m): 1964.5
Distance between rig floor and sea level (m): 28.5
Water depth (drill pipe measurement from sea level, m): 1936

Operation	Start Date (Oct 2007)	Start Local time (h)	Depth (m LSF) Top	Depth (m LSF) Bottom	Drilled (m LSF)	Comments
Hole C0002A LWD hole			0	1401.5	1401.5	8-1/2 inch LWD (GVR-sonic-SVWD-MWD-APWD-ADN)
ROV survey	13	2200				
Tag seafloor	13	2200				
Spud-in	14	0045				
Rig floor maintenance	15	0445				Mechanical failure on power swivel
Ream and sweep	15	1500				Wiper trip for 8 stands
Reach total depth	17	1110				
Pull tools out of hole	17	1400				
Recover tools on the rig floor	18	0415				
Recover data	18	0600				Download all data with delay on seismicVISION because battery ran out before reaching rig floor

Notes: LSF = LWD depth below seafloor. LWD = logging while drilling. GVR = geoVISION resistivity tool, sonic = sonic while drilling (sonicVISION), SVWD = seismicVISION while drilling, MWD = measurement while drilling, APWD = annular pressure while drilling, ADN = Azimuthal Density Neutron tool (adnVISION). ROV = remotely operated vehicle.

Table T2. Bottom-hole assembly, Hole C0002A. (See table notes.)

BHA component	Length (m)	Cumulative length from bit (m)
PDC bit	0.320	0.320
Stabilizer/float sub	1.500	1.820
Crossover sub	0.612	2.432
geoVISION	3.080	5.512
sonicVISION	7.620	13.132
Power Pulse	8.550	21.682
seismicVISION	4.630	26.312
adnVISION	6.230	32.542
Crossover sub	0.610	33.152
6-3/4 inch drilling collar	9.315	42.467
6-3/4 inch drilling collar	9.319	51.786
6-3/4 inch drilling collar	9.313	61.099
6-3/4 inch drilling collar	9.315	70.414
6-3/4 inch drilling collar	9.316	79.730
6-3/4 inch drilling collar	9.313	89.043
6-3/4 inch drilling collar	9.315	98.358
6-3/4 inch drilling collar	9.314	107.672
6-3/4 inch drilling collar	9.314	116.986
6-3/4 inch drilling collar	9.318	126.304
6-3/4 inch drilling collar	9.315	135.619
6-3/4 inch drilling collar	9.314	144.933
Jar	10.095	155.028
6-3/4 inch drilling collar	9.314	164.342
6-3/4 inch drilling collar	9.314	173.656
6-3/4 inch drilling collar	9.310	182.966
6-3/4 inch drilling collar	9.310	192.276
6-3/4 inch drilling collar	9.315	201.591
6-3/4 inch drilling collar	9.310	210.901
6-3/4 inch drilling collar	9.310	220.211
6-3/4 inch drilling collar	9.315	229.526
Crossover sub	0.610	230.136
Crossover sub	0.800	230.936
Crossover sub	0.610	231.546

Notes: BHA = bottom-hole assembly. PDC = polycrystalline diamond compact.

Table T3. Quality control characteristics and sonic log data, Hole C0002A. (See table notes.)

Depth interval (m LSF)				
Top	Bottom	Zone	Quality	Comments
–6	107	2	0	Difficult to distinguish from mud arrival.
107	634	2	2	Fairly intermittent arrivals with zones of clear arrivals and zones hard to pick on MP wide. While in general worse, there are patches where MP widefast (pulling out) returns improved signal over MP wide (e.g., 327–347 m LSF). Leaky-P gives a more continuous, but less trustworthy coherence. Separation from mud arrival improves with depth. Note: processing parameter change at 546 m LSF but no obvious change in coherence.
634	760	1	1	Fairly strong arrivals on MP wide clearly distinguished from mud velocity.
760	813	1	2	Intermittent arrivals with some gaps in MP wide. 2 m scale oscillation in values that may be noise related.
813	934	1	1	Excellent arrivals; significant jumps appear to be trustworthy.
934	978	1	3	Very few reliable looking coherency patches. Base is location of parameter change from “very slow” to “slow” parameters.
978	1075	1	2	Reliable patches with small gaps that are unpickable in between.
1075	1099	1	3	Large unpickable gap.
1099	1118	1	2	Pickable section.
1118	1150	1	3	Unpickable.
1150	1165	1	2	Pickable but not as clear as some of the patches.
1165	1191	1	3	Unpickable.
1191	1282	1	2	Pickable with some clear patches and some mediocre patches.
1282	1293	1	3	Unpickable.
1293	1391	1	2	Mix of pickable coherent packages and small unpickable gaps.

Notes: LSF = LWD depth below seafloor, MP = mixed processing. See “Data and log quality.”

Table T4. Quality control characteristics and resistivity image data, Hole C0002A. (See table notes.)

Depth interval (m LSF)		Comments
Top	Bottom	
—	129	Start GVR rotation, beginning of image log
129	197	Very good
197	201	Excellent
201	202	Poor
202	218	Excellent
218	219	Poor
219	323	Excellent
323	324	Poor
324	1353	Excellent
1353	1355	Good (data drop-outs)
1355	1398	Excellent
—	1398	End of GVR image log

Notes: LSF = LWD depth below seafloor. GVR = geoVISION resistivity tool.

Table T5. Logging units and zones, Site C0002. (See table notes.)

Depth (m LSF)	Logging unit	Zone	Interpreted lithology	Description
0–135.5	I		Unconsolidated sandy/silty mud	Basin sediments
135.5–218.1	II			
218.1–400.4		A	Hydrate-bearing zone; Hemipelagic mud and silty/sand turbidites	
400.4–481.6				
481.6–547.1		B	Potential gas zone; Hemipelagic mud and silty/sand turbidites	
547.1–830.4				
830.4–935.6	III		Mudstone	
935.6–TD	IV		Deformed sandy/silty turbidites	Accretionary prism

Notes: LSF = LWD depth below seafloor. TD = total depth.

Table T6. Check shot–corrected depths, dips, and dip directions for prominent stratigraphic and structural features, Site C0002. (See table notes.)

Depth (m)		Feature	Dip (°)	
SSL	SSF		Direction	Angle
1937	0	Seafloor		
2065	128	Top of Kumano 5	165	2
2154	217	Top of Kumano 6	294	2
2190	253	Fault, Kumano 11	—	—
2268	331	Top of Kumano 7	323	4
2341	404	BSR	—	—
2362	425	Top of Kumano 8	330	6
2426	489	Dipping negative reflector	—	—
2492	555	Top of Kumano 9	334	7
2584	647	Top of Kumano 10	346	6
2739	802	Top of Kumano 11	354	5
2807	870	Top of Lower Sediments 1	111	2
2884	947	Top of Accretionary Prism	0	2
2970	1033	Prism Reflector 1	119	10
3076	1139	Prism Reflector 2	107	15
3186	1249	Prism Reflector 3	127	23

Notes: SSL = seismic depth below sea level, SSF = seismic depth below seafloor, BSR = bottom-simulating reflector. — = no data.

Table T7. Strikes and dips of four faults closest to Site C0002 within the Kumano Basin. (See table notes.)

Fault	Location*	Strike (°)	Dip (°)
Kumano 10	475 m SSE	082	57.5
Kumano 11	At borehole	080	55.5
Kumano 12	250 m NNW	083	59.5
Kumano 13	500 m NNW	058	55.0

Notes: * = relative to borehole. SSE = south-southeast, NNW = north-northwest.

Table T8. Check shot raw and smoothed traveltimes and calculated interval velocities, Site C0002. (See table notes.)

		Raw		Smoothed	
Depth* (m LSF)	Midpoint depth† (m LSF)	First arrival time* (ms)	Interval velocity† (m/s)	First arrival time* (ms)	Interval velocity† (m/s)
1.65	9.20	1292.0	1257	1291.6	1494
16.74	27.08	1304.0	2584	1301.7	1487
37.41	46.27	1312.0	0984	1315.6	1489
55.13	62.35	1330.0	2405	1327.5	1488
69.56	81.38	1336.0	1313	1337.2	1534
93.19	100.57	1354.0	2460	1352.6	1570
107.95	119.76	1360.0	1312	1362.0	1652
131.57	150.77	1378.0	1745	1376.3	1722
169.96	177.18	1400.0	2888	1398.6	1783
184.40	196.21	1405.0	1575	1406.7	1803
208.02	215.41	1420.0	2462	1419.8	1801
222.79	234.60	1426.0	1389	1428.0	1789
246.41	253.63	1443.0	2407	1441.2	1783
260.85	272.66	1449.0	1575	1449.3	1817
284.47	291.85	1464.0	3690	1462.3	1845
299.23	311.05	1468.0	1477	1470.3	1846
322.86	330.08	1484.0	2405	1483.1	1827
337.29	349.11	1490.0	1575	1491.0	1846
360.92	368.30	1505.0	2109	1503.8	1845
375.68	387.49	1512.0	1968	1511.8	1845
399.30	406.52	1524.0	1805	1524.6	1828
413.74	425.55	1532.0	1687	1532.5	1803
437.36	456.56	1546.0	1745	1545.6	1786
475.75	482.97	1568.0	2407	1567.1	1783
490.19	502.00	1574.0	1476	1575.2	1750
513.81	521.20	1590.0	2462	1588.7	1738
528.58	540.39	1596.0	1575	1597.2	1724
552.20	559.42	1611.0	2063	1610.9	1761
566.64	578.45	1618.0	1476	1619.1	1803
590.26	609.46	1634.0	1919	1632.2	1873
628.65	635.87	1654.0	3607	1652.7	1977
643.08	654.90	1658.0	1688	1660.0	2020
666.71	674.09	1672.0	2460	1671.7	2050
681.47	693.28	1678.0	1687	1678.9	2109
705.09	712.31	1692.0	3610	1690.1	2124
719.53	731.34	1696.0	1968	1696.9	2167
743.15	750.37	1708.0	2407	1707.8	2188
757.59	776.79	1714.0	2133	1714.4	2169
795.98	834.20	1732.0	2123	1732.1	2165
872.42	891.62	1768.0	2399	1767.4	2194
910.81	922.63	1784.0	1969	1784.9	2229
934.44	941.66	1796.0	2405	1795.5	2255
948.87	960.68	1802.0	2362	1801.9	2339
972.49	979.88	1812.0	2462	1812.0	2344
987.26	999.07	1818.0	2362	1818.3	2410
1010.88	1029.91	1828.0	2379	1828.1	2455
1048.94	1056.33	1844.0	2462	1843.6	2547
1063.71	1075.52	1850.0	2952	1849.4	2540
1087.33	1094.55	1858.0	2407	1858.7	2533
1101.77	1113.58	1864.0	2362	1864.4	2513
1125.39	1132.77	1874.0	2460	1873.8	2502
1140.15	1159.18	1880.0	2719	1879.7	2537
1178.21	1190.03	1894.0	2363	1894.7	2597
1201.84	1209.22	1904.0	2460	1903.8	2636
1216.60	1228.41	1910.0	2952	1909.4	2747
1240.22	1247.44	1918.0	2888	1918.0	2831
1254.66	1266.47	1923.0	2953	1923.1	2880
1278.28	1285.67	1931.0	2954	1931.3	2896
1293.05	1304.86	1936.0	2624	1936.4	2846
1316.67	1324.06	1945.0	2954	1944.7	2896
1331.44	1343.25	1950.0	2952	1949.8	2846
1355.06	—	1958.0	—	1958.1	—

Notes: Smoothed values were used in the generation of synthetic seismograms and time-depth conversion of seismic reflection profiles near the site. * = first arrival time picks associated with depths of observations, † = interval velocities associated with midpoints between depths of observations. LSF = LWD depth below seafloor. — = no data.